ENHANCED DAMAGE TOLERANCE OF COMPOSITE MATERIALS BY MULTIPLE DELAMINATIONS

PhD thesis

Daan Jonas Hottentot Cederløf

January, 2022
DTU Wind Energy
Technical University of Denmark

Prepared by:
Daan Jonas Hottentot Cederløf

Main supervisor:
Bent F. Sørensen, Professor
Technical University of Denmark
DTU Wind Energy, Section of Composites Analysis and Mechanics
Mail: bsqr@dtu.dk

Co-supervisors:
Yukihiro Kusano, Dr.
Danish Technological Institute
Mail: yuk@teknologisk.dk

Malcolm McGugan, Chief Engineer
Technical University of Denmark
DTU Wind Energy, Section of Composites Analysis and Mechanics
Mail: mamc@dtu.dk

Stergios Goutianos, Professor
Norwegian University of Science and Technology
Department of Manufacturing and Civil Engineering
Mail: stergios.goutianos@ntnu.no

Publication reference data
Daan J. Hottentot Cederløf
Enhanced damage tolerance of composite materials by multiple delaminations
PhD thesis
Technical University of Denmark
DTU Wind Energy, Section of Composites Analysis and Mechanics
January 2022
https://doi.org/10.11581/dtu.00000222

Preface

This thesis is submitted to the Technical University of Denmark in candidacy for a degree of Doctor of Philosophy, PhD. The study was done in accordance with the regulations regarding the PhD programme in Denmark.

The topic treated is control of initiation of multiple delaminations in unidirectional glass fibre reinforced composite materials, to enhance fracture resistance of the laminate. The materials in this thesis are primarily used in wind turbine blades and civil structures such as bridges. The work was performed at the Composite Analysis and Mechanics section at DTU Wind Energy from September 2018 to January 2022, with a brief 3 month hiatus from July 2021 to end September 2021.

The research was performed as part of the EU Horizon 2020 project DACOMAT with funding from the EU Horizon 2020 research and innovation programme 5 under GA No. 761072. The project was supervised by Bent F. Sørensen (DTU Wind Energy), Yukihiro Kusano (Danish Technological Institute), Malcolm McGugan (DTU Wind Energy) and Stergios Goutianos (Norwegian University of Science and Technology).

Daan Jonas Hottentot Cederløf

Risø, Denmark
January 2022

Acknowledgements

"If I have seen further it is by standing on the sholders [sic] of Giants." - Isaac Newton

This PhD would not have been possible without the support of Giants. That includes the scientists whose work I have used as a foundation and a long list of colleagues, friends and family who have supported me along the way.

Bent, for all the discussions and digressions, on topics ranging from tulips to fracture process zones, thank you for guiding me. Your attention to detail, careful logic and endless curiosity are qualities I admire and will carry with me. Yuki, thank you for taking me in when I first started and encouraging me to learn from experiments from day one. Special thanks to both Bent and Yuki for supporting me in writing this thesis. I want to thank both Malcolm and Stergios for the support in steering my PhD. I want to thank the members of the DACOMAT project. It has been a great benefit to gain an insight into the whole value chain of the composites industry.

Special thanks to the fiberlab and testlab technicians, who have all contributed significantly to this experimental PhD: Christian, Jonas, Adnan, Anette, Hans, Vagn, Kenneth, Jan, Erik and Gitte. Most of all, thanks for fruitful discussions, helping me understand my many experiments and friendly chats over coffee.

To all the students, postdocs, engineers and researchers at DTU Wind who have supported me along the way. Thank you for keeping my spirits high. Special thanks to Nicolai, Ulrich, Ashish and Kristine who took the time to help me fine tune numerous graphs and figures. Thank you to my fellow members of the PhD committee and PhD association: Rebecca and Max.

Life isn't all about studying and work. My friends and family have kindly been there to remind me of that. I have been fortunate to occasionally take my mind off both the global pandemic and my studies by giving a helping hand to the space architects at SAGA studio. Thanks for taking me in and keeping me busy.

A warm thank you to the Danish winter climate for keeping me indoors whilst writing this thesis.

To Benedicte, without whom this PhD would never have started, I cannot express enough my gratitude for your support, care and love throughout this voyage. I look forward to our next adventure.

Abstract

Delamination is a common damage mechanism in composite structures such as wind turbine blades and bridges. Growth of delamination cracks can lead to failure of the composite component and possibly the structure it is a part of. Naturally, delamination damage is unwanted and avoided where possible. However, it is inevitable in large composite structures that delaminations occur and propagate. Instead of trying to avoid delaminations altogether, they should rather be accepted and controlled such that delamination growth is stable or arrested. Enhancing the fracture resistance of a composite system is a method for reducing delamination growth, and could possibly even stop the delamination altogether. In this work, a method for enhancing fracture resistance by means of introducing multiple parallel delaminations is presented. By the use of plasma fluorination to introduce a controlled weak layer close to where a primary delamination is expected, a secondary delamination crack is induced. Both crack interfaces demonstrate large amounts of fibre bridging, a toughening mechanism that increases the resistance to delamination. It is demonstrated experimentally that in cases where a secondary delamination crack forms, the apparent fracture resistance of the whole laminate increases approximately by a factor of two.

Resumé

Delaminering er en almindelig skadesmekanisme i kompositstrukturer såsom vindmøllevinger og broer. Vækst af delamineringsrevner kan føre til svigt af delkomponenter og hele den struktur den er en del af. Naturligvis er delaminationskader uønsket og bør undgås, hvor muligt. Det er dog uundgåeligt, at der opstår delamineringer i store kompositstrukturer. I stedet for at prøve for at undgå delamineringer helt, bør de snarere accepteres og kontrolleres sådan at delamineringsvæksten er stabil eller standses. Øgelse af revnevækstmodstanden for et kompositsystem er en metode til at reducere delamineringsvæksten, og kan bruges til at stoppe delamineringer helt. I den foreliggende afhandlingen præsenteres en metode til at forøge revnevækstmodstand ved at indføre flere parallelle delamineringer. Ved brugen af plasmafluorering indføres et kontrolleret svagt lag tæt på hvor en primær delaminering forventes, med det formål at udvikle en sekundær delamineringsrevne. Begge revne indeholder store mængder fiber, der danner 'bro' mellem revnefladerne. Dette er en sejhedsforøgende mekanisme, der øger modstanden mod delaminering. Det demonstreres eksperimentelt at i tilfælde hvor der dannes en sekundær delamineringsrevne, vil den makroskopiske revnevækstmodstand, karakteriseret ved J integralet, af hele laminatet fordoples.

Publications

Publications appended to this thesis

[P1] **Hottentot Cederløf, D. J.**, Kusano, Y., and Fæster, S. (2019). Fluorination of sized glass fibres for decreased wetting by atmospheric pressure plasma treatment in He/CF_4. *Journal of Adhesion*, 96(1-4), pp. 2–12.

[P2] Fang, C., **Hottentot Cederløf, D. J.**, Bardenshtein, A., and Kusano, Y. (2020). Air-to-air atmospheric pressure plasma treatment – perspective for composite manufacturing *IOP Conf. Series: Materials Science and Engineering*, 942, 012030.

[P3] **Hottentot Cederløf, D. J.**, Kusano, Y., and Sørensen, B. F. (2021). Control of interfacial peak stress by atmospheric pressure plasma treatment. Submitted to *Composite Interfaces*.

Other publications and contributions

- Kusano, Y., **Hottentot Cederløf, D. J.**, Fæster, S. (2020). Plasma surface modification of glass fibre sizing for manufacturing polymer composites. *Key Engineering Materials*, 843, pp. 159-164.
- **Hottentot Cederløf, D. J.**, and Sørensen, B. F. (2020). Characterisation of fibre/matrix interfacial fracture energy using the single fibre peel experiment. *IOP Conf. Series: Materials Science and Engineering*, 942, 012029.
- **Hottentot Cederløf, D. J.** and Kusano, Y. (2020). Tech. Report. D2.5: Methods for lamina interface modification *DACOMAT GA No. 761072*
- McGugan, M. and **Hottentot Cederløf, D. J.** (2020). Tech. Report. D5.4: Tools for MAPOD for the SHM technique based on Acoustic Emission *DACOMAT GA No. 761072*

Contents

Chapter 1

Introduction

The global electricity generation in 2020 was 26 762 TWh [1]. Of this, wind energy production totalled just 1596 TWh or around 6% of the global total. With the ongoing electrification of our society e.g. transitioning to fully electric transport, the demand for electricity will inevitably increase. This is in addition to the global population increase and the hundreds of millions of people who are transitioning out of poverty into a life associated with increased energy usage [2].

Simultaneously, there is an urgent need to reduce the effects of anthropogenic climate change. Global climate risk factors will increase by the end of the 21st century, even with moderate greenhouse gas emission trajectories [3, 4]. The transition away from traditional fossil fuel energy sources is therefore required to maintain our planet's habitability, for current and future generations. The electricity production from wind turbines is expected to triple from 2020 levels within just 10 years [1].

Wind turbines are today a viable method of energy production, able to compete on price with fossil fuel energy sources [5]. The levelised cost of energy (LCoE) of wind energy has decreased steadily as the technology has evolved and the size of wind turbines has increased, both in height and rotor diameter. Today, there are off-shore wind turbines in use with capacities of up to 12 MW and rotor diameters up to 220 m; a 15 MW 236 m diameter turbine was recently announced by Vestas [6].

1.1 Composite materials

The historical increase in rotor diameter is made possible through the utilisation of high performance, low cost composite materials such as glass fibre reinforced polymers. The rotor blades of all commercial wind turbines are made of composite materials, due to the excellent weight specific performance of fibre composites (illustrated in the Ashby plot in fig. 1.1). Weight specific means the performance with respect to weight, for example the ratio of stiffness to weight, or strength to weight. Glass fibres have typically been used to keep production costs low, however larger blades are seeing an increasing use of carbon fibres together with glass fibres [7, 8].

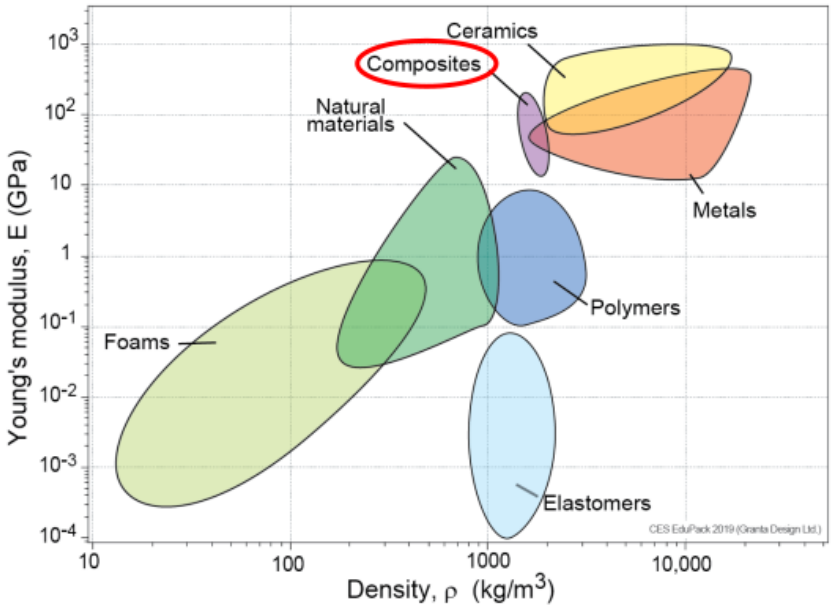

Figure 1.1: Young's Modulus vs Density Chart. Material Family Chart. Chart created using CES EduPack 2019, ANSYS Granta © 2020 Granta Design.

The material system in this research is a glass fibre reinforced vinyl ester composite which is typically used in marine, civil or wind energy structures [9]. The two components that make up the composite are: glass fibres (in fabric form) and a vinyl ester resin system. These are commonly referred to as the fibre and matrix, respectively. In short, the fibre provides high stiffness and strength (in the lengthwise direction of the fibre), whilst the matrix binds everything together and protects the fibres (e.g. from environmental exposure).

A fabric consists of three sub-elements: fibre bundles, stitching thread and backing material. Bundles of several thousand fibres are stitched together with backing material. The backing material, in this case sparse glass fibre bundles, allows the handling of the fabrics before they are infused with the resin [10]. Without the backing fibres, the fabrics would unravel and fall apart when placed in a mould.

In order to manufacture a composite part by vacuum infusion, layers of fabrics are first placed in a mould. Next, the mould is sealed and a vacuum is applied by a vacuum pump to one side of the mould (outlet side). Elsewhere on the mould, a reservoir of resin is connected to the mould (inlet side). As the inlet is slowly opened, resin is displaced out of the reservoir due to the pressure differential applied by the vacuum pump at the outlet. As the resin is pulled through the fabrics in the mould, it fills the gaps within the fabrics and wets the fibres. When the infusion is complete the part may be cured. The cure cycle dependent on the resin system, production time limits,

residual stress requirements, etc. [11]. Finally, the part may be de-moulded and inspected for defects such as voids [12].

A note on length scales: Wind turbine blades can span over 100 m but the glass fibres they are made of have a diameter in the micrometer scale (0.000 001 m). In this thesis, investigations are made down to the molecular scale (nanometer) when dealing with surface treatments and up to the element scale when testing fibre composite specimens. In table 1.1, the different scales are defined along with a characteristic example at each scale.

Table 1.1: Length scales used in the present work

Scale	Unit	Order of magnitude [m]	Example
Nano	nm	10^{-9}	Diameter of fluorine atom $\approx$ 0.3 nm
Micro	μm	10^{-6}	Thickness of 'sizing' coating on a glass fibre
Macro	mm	10^{-3}	Cohesive law end opening opening
Element	m	1	DCB specimen 0.6 m

1.2 Glass fibres

In the glass fibre manufacturing process, after the fibres have been formed, they are treated with a thin coating layer called *'size'*. The process of applying the surface coating is called *'sizing'*. These two terms are often used interchangeably in the literature [13], in this thesis the two words will also be used interchangeably. Sizing plays several important roles in the production of composite materials, such as: physical protection of the fibre, preventing moisture absorption, increasing wetting with resins and acting as a coupling agent between the fibre and resin [13–15]. The majority of size formulations contain a silane coupling agent that will covalently bond to the glass fibre surface and react with the polymer resin, creating a strong fibre-polymer connection [13]. Around 80-90% of sizing (by weight) is made up of a film former, which is typically chosen to be compatible to the intended resin matrix [13]. Film former materials include polyurethanes, polyesters and epoxies [13]. The thickness of the size is typically in the order of 10 nm - 1 µm, though large variation in sizing layer thickness has been reported [16, 17].

Since both uninfused 'dry' fibres and cured fibre composites are investigated, it is important to distinguish the type of surface or volume that is characterised. During composite manufacturing, the sizing layer and the polymer matrix diffuse into each other, forming a transition region between the glass fibre and polymer matrix [18].

This transition region between fibre and polymer is called the interphase region [19], not to be confused with an interface. The interphase is a 3D volume whereas an interface is a 2D plane of zero thickness transition between two materials (see fig. 1.2). This distinction is important in the context of surface treatment of glass fibres because any treatment applied to the sizing surface will be diffused into a volume around the fibre (the interphase) when the fabric is infused with a polymer resin. In this thesis, the word interphase is used for the fibre/matrix transition region. The word interface is used when describing transitions between two laminae in a fibre composite layup.

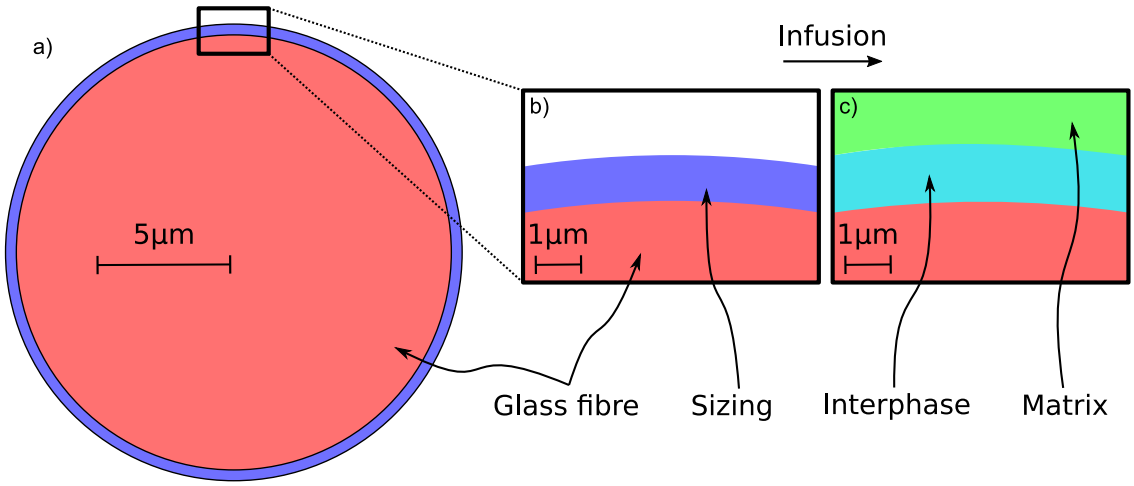

Figure 1.2: Illustration of the cross section of glass fibre interphase formation as a result of resin infusion. **a)** Sized fibre prior to contact with resin, **b)** Close up view of sizing layer prior to infusion, **c)** Interphase region after sizing has diffused into resin.

1.3 Damage in composite structures

Manufacturing of large composite structures such as wind turbine blades inevitably leads to defects. It is prohibitively expensive to develop a manufacturing method that would result in a 'defect free' material (for example due to high rejection rates or a lot of repairs). Instead, it is more cost-effective to accept the fact that damages occur (from manufacturing defects or other sources) and to try to limit or stop damage growth. The damage tolerance philosophy is well established within the aerospace engineering industry, where weight is the primary design driver [20–22]. Damage tolerant designs rely on frequent inspections to catch damage growth before it becomes critical, this allows for lower design safety factors and therefore less material to be used in the airframe [21].

The primary focus of this study is on the delamination of unidirectional composite laminates, a common failure mode for large composite structures [23, 24]. Delamination is a phenomena where two plies within a cured composite laminate separate from each other. A delamination may form as a result of impact, overloading or manufacturing defects. Delamination is often associated with a decrease in stiffness of a structure, which can lead to structural failure. In stiffness driven designs such as wind turbine rotor blades, this is a critical damage type. For example, a loss in bending stiffness of a rotor blade can result in the blade tip bending far enough to strike the turbine tower, leading to a total loss of the turbine.

Delamination may occur in three so called *fracture modes*, which are illustrated in fig. 1.3. Typically, materials are more resistant to shearing type fracture (mode II and mode III) than normal opening mode I type fracture. Pure mode I is rarely encountered in real life situations, instead a combination of mode I and mode II (known as mixed mode) is more common.

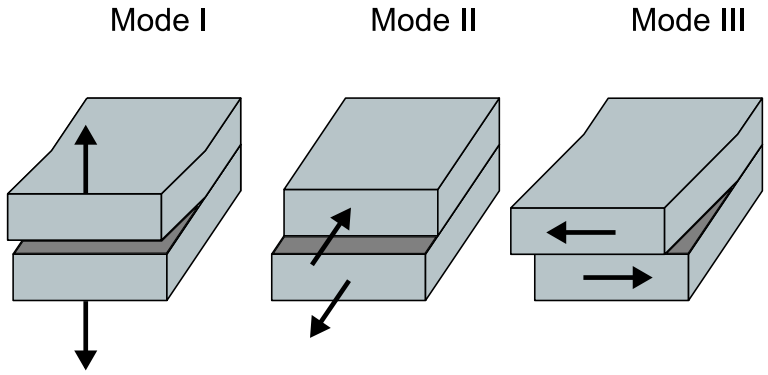

Figure 1.3: Illustration of the three different fracture modes.

1.4 Fracture resistance

The ability of a fibre composite material to withstand the growth of a delamination may be characterised by its fracture resistance. Fracture resistance is the value of the J-integral when the crack grows. The resistance curve (known as R-curve) is a graph showing the J-integral as a function of crack extension, a.

A phenomenon known as the R-curve effect (shown in fig. 1.4) is sometimes observed in delaminating composites. It is the apparent toughening of a composite as the delamination crack propagates [25]. The R-curve behaviour is normally seen in laminates where *fibre bridging* occurs (illustrated in fig. 1.5) such as reinforced ceramics [26], fibre reinforced polymers [25], wood [27] or natural composites [28]. Other

phenomena in fibre composites that contribute to the R-curve behaviour include z-direction reinforcements (such as stitching, z-pinning or interlocking) [29–31] and interleaving [32].

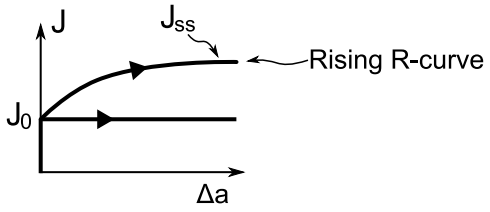

Figure 1.4: Illustration of two R-curves. The top curve shows a rising 'R-curve effect' often observed in fibre composite materials exhibiting fibre bridging. The lower curve indicates a constant fracture energy.

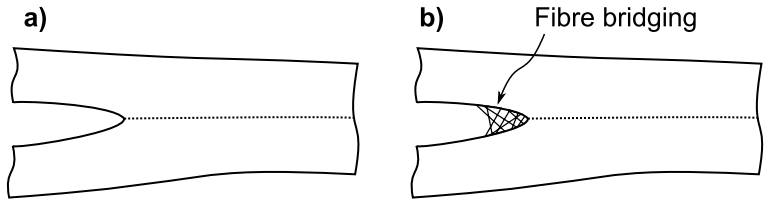

Figure 1.5: Multiple delaminations in a composite material: **a)** without fibre bridging and **b)** with large scale fibre bridging.

In this thesis, the words crack and delamination are used interchangeably, both words include the fibre bridging zone and the crack tip. Where necessary, specific reference is made to for example a crack tip or fibre bridging zone.

1.5 Cohesive Laws

For the problem of delamination of laminates, small scale yielding at the crack tip (i.e. no plasticity) is assumed since the problem is related to brittle thermoset polymer matrix composites. In specimens exhibiting large scale fibre bridging (LSB), the use of linear elastic fracture mechanics (LEFM) is no longer valid [33]. The delamination process may be described in terms of a cohesive law defined by a traction-separation relation, where the normal ($\sigma_n = \sigma_{22}$) and shear tractions ($\sigma_t = \sigma_{11}$) are dependent on the the normal ($\delta_n = \delta_{22}$) and tangential ($\delta_t = \delta_{11}$) opening displacements of the crack face. A simplified illustration of a crack with fibre bridging showing normal opening displacement only is shown in fig. 1.6. Both mode I opening (normal or x_2 direction) and mode II sliding (tangential or x_1 direction) are possible, illustrations of mode I and mode II traction-separation laws are shown in fig. 1.7, where δ^0 is the end-opening at

full separation (i.e. traction is zero) and $\hat{\sigma}$ is the peak traction.

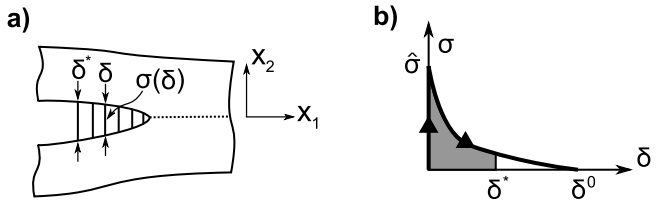

Figure 1.6: a) Illustration of a bridged crack undergoing opening. **b)** A graphical representation of a cohesive law that describes the traction σ as a function of separation δ. δ^0 is the end-opening at full separation and $\hat{\sigma}$ is the peak traction. The contribution to the J-integral is the area under the traction-separation curve from zero to the end-opening, δ^*.

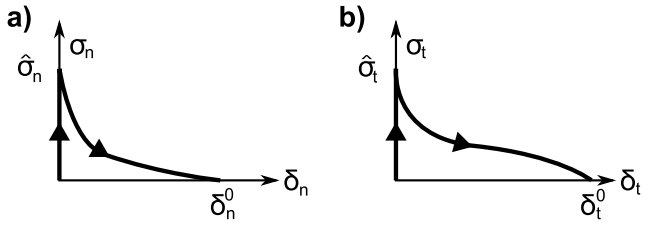

Figure 1.7: Illustration of traction separation laws for normal opening (a) and tangential opening (b). $\hat{\sigma}_n$ is the peak normal traction and $\hat{\sigma}_t$ is the peak tangential traction. δ_n^0 and δ_t^0 are the normal end-opening and tangential end-opening at full separation.

The path independent J-integral approach may be adopted to determine cohesive laws [34]

$$J = \int_\Gamma \left(W dx_2 - T_i \frac{\partial u_i}{\partial x_1} dS \right), \tag{1.1}$$

where Γ is the contour going counter clockwise around the fracture process zone, the surface traction defined by $T_i = \sigma_{ij} n_j$, where σ_{ij} is the stress tensor and n_j the outward normal to the path Γ; u_i is the displacement vector and dS is a segment around path Γ. The strain energy density, W, is defined by

$$W = \int_0^{\epsilon_{ij}} \sigma_{ij} d\epsilon_{ij}, \tag{1.2}$$

where ϵ_{ij} is the infinitesimal strain tensor.

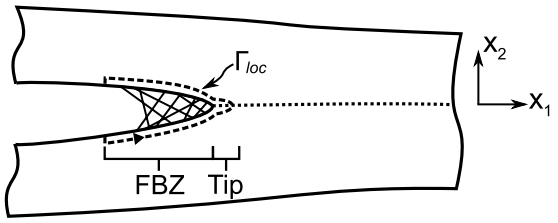

Figure 1.8: Illustration of the counterclockwise integration path,Γ_{loc}, for the J-integral, indicating both crack tip and fibre bridging zone (FBZ).

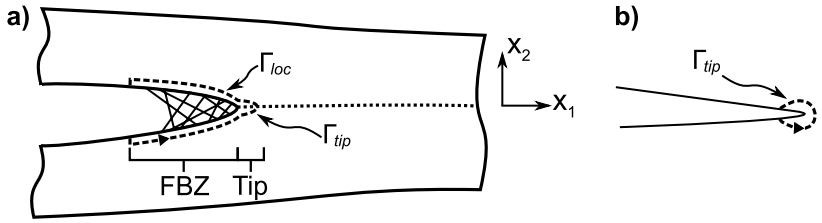

Figure 1.9: a) Illustration of the counterclockwise integration path,Γ_{loc}, for the J-integral, indicating both crack tip and fibre bridging zone (FBZ). **b)** close up view of the J-integral path around the crack tip.

Applying the J-integral along a path locally around the cohesive zone gives [25]

$$J_{loc} = J_{tip} + \int_0^{\delta_n^*} \sigma_n d\delta_n + \int_0^{\delta_t^*} \sigma_t d\delta_t, \tag{1.3}$$

where J_{tip} is the J-integral value of the crack tip (Γ_{tip}), δ_n^* is the normal end-opening displacement and δ_t^* the tangential end-opening displacement (see fig. 1.6).

Cracking (advancement of the crack tip) will occur when J_{tip} equals the fracture energy of the crack tip, J_0. Then, under crack growth, the J-integral results can be given the physical interpretation as the sum of the energy dissipation of the crack tip (J_0) and the work of the cohesive tractions at the end of the cohesive zone, where $\delta_n = \delta_n^*$ and $\delta_t = \delta_t^*$. As the crack opens, the work of the cohesive tractions increase (the integrals in eq. (1.3)). Steady-state is attained when $\delta_n^* = \delta_n^0$ and $\delta_t^* = \delta_t^0$.

The steady state crack propagation is defined when the crack is propagating and the bridging zone is fully developed. At this point J=J_{ss}. The contribution to the steady state J-integral (J_{ss}) can be split into the two segments (shown in fig. 1.9),

$$J_{ss} = J_0 + \Delta J_{ss}, \tag{1.4}$$

where, J_0, is the crack tip contribution and J_{FBZ} is the fibre bridging zone contribution. The unit of J is J/m^2 (Joule per meter square) and its physical meaning can be interpreted as the work per unit fracture area.

For the pure modes, differentiating the J-integral with respect to end opening δ^* gives the combined tip and bridging law [25]. For pure mode I the second integral in eq. (1.3) vanishes and for pure mode II the first integral in eq. (1.3) vanishes,

$$\sigma_n(\delta_n^*) = \frac{dJ}{d\delta_n^*} \quad \text{(Mode I)}, \qquad \sigma_t(\delta_t^*) = \frac{dJ}{d\delta_t^*} \quad \text{(Mode II)}. \tag{1.5}$$

1.6 Multiple delaminations

Previous experimental works [35–37] have shown that the formation and propagation of multiple parallel delamination cracks in bonded joints, with large scale fibre bridging, can increase fracture resistance of the overall specimen. The steady state fracture resistance increased near proportionally to the number of new cracks formed [36]. One extra crack doubled the steady state fracture resistance whilst 2 new cracks resulted in a tripling of the steady state fracture resistance. However, the formation of these multiple cracks was not consistent and their formation was not understood. In the work by Kusano et al. [35], all the mode II specimens and two out of six mode I specimens showed multiple cracks. Similarly, in the study by Rask and Sørensen [36], mixed mode specimens showed either two or three delamination cracks, whereas mode I specimens did not develop multiple cracks.

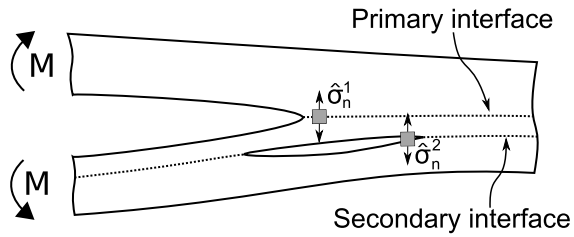

Figure 1.10: Illustration of multiple crack formation. Initially a crack occurs on the primary crack plane, later a secondary crack forms and both cracks continue to propagate. The superscript indicates primary (1) and secondary (2) delamination plane. The subscript, n, refers to normal direction ($\sigma_{22} = \sigma_n$). After: [38]

Further numerical and analytical modelling by Goutianos and Sørensen [39] explained the possible increase in fracture resistance by multiple cracks. They showed by nu-

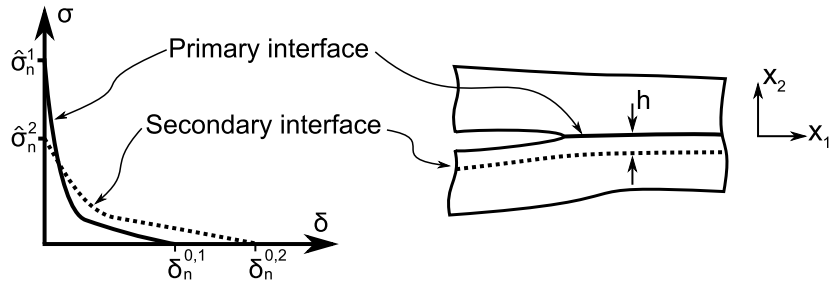

Figure 1.11: Illustration of cohesive law requirement for formation of multiple parallel cracks. The superscript indicates primary (1) and secondary (2) delamination plane. The subscript, n, refers to the opening mode. Layer thickness = h.

merical modelling that there are two key criteria for initiating multiple cracks in a laminate:

1. The strength of the interface of the secondary crack must be lower than the strength of the primary crack interface. In terms of cohesive laws this means that the peak traction ($\hat{\sigma}_n = \sigma_{22}$) of the secondary crack must be lower than the peak traction of the primary crack (see fig. 1.11). This criterion was also suggested by Kusano et al. [35].

2. The distance, h, from the primary crack to the secondary crack must be small enough such that the stress field around the primary crack tip directly influences the secondary crack plane (see fig. 1.11). In fibre composites this would be primarily driven by the thickness of a single ply in the layup.

This insight now opens the possibility to tailor interfaces to control the formation of multiple cracks and increase the fracture resistance of fibre composites.

An increase in fracture resistance by multiple cracks can have significant benefits for the cost of composite components, which in the case of wind turbines could lower the LCoE. Less conservative design choices may be made, reducing the material usage during manufacturing. Service costs may be lowered by increased inspection intervals. A laminate exhibiting slower damage growth will need fewer repairs, further reducing costs. Finally, service life of a tougher blade may be increased with decreased damage growth, allowing a turbine to remain in operation longer. This allows not only a quicker transition to renewable energy sources but reduces the environmental impact of composite turbine blades as they are currently impossible to fully recycle to their initial material components [40].

1.7 Decreased peak traction by plasma fluorination

In the literature, there are examples of how fracture properties of composite interfaces may be controlled. Kuhtz et al. [41, 42] showed that perforated polytetrafluoroethylene (PTFE) films could be used to modify the interlaminar contact area (and as a result mean peak traction) in fibre composites. The perforated PTFE films were used to induce multiple delaminations which was shown to increase the energy absorption capacity and impact resistance [42]. However, the inclusion of PTFE films (with or without perforations) will likely act as an interlaminar barrier, preventing the formation of fibre bridging.

Plasma treatment is an attractive modification method because it affects the surface of a material without changing physical or chemical properties of the bulk material [43]. Plasma treatments are used for surface modification because it has high treatment efficiency, low environmental impact and allows for selective functionalization (nitration, oxidation, fluorination) [44].

The wettability of a fibre is generally accepted to be important to ensuring a strong fibre/matrix bond [15], however it is a difficult parameter to measure on rough, porous surfaces such as fabrics [45]. Mäder et al. [46] performed wetting measurements on glass and carbon fibres with different sizings using the micro-Whilhelmy technique. Mechanical characterisation was performed by single-fibre pull-out (interfacial shear strength, IFSS), short beam shear (interlaminar shear strength, ILSS) and compression shear (shear strength, SS) tests [46]. Generally, for the glass fibre systems, a higher advancing contact angle (i.e. lower wetting) correlated with a lower IFSS and ILSS. The authors concluded that whilst wetting measurements are a useful tool for characterising fibre surfaces, they cannot alone be used to draw conclusions about the fibre/matrix interphase properties (i.e. fibre/matrix bond strength) [46]. In another study on carbon fibre/epoxy systems, Mäder et al. [47] found a weak inverse correlation between IFSS and contact angle (i.e. decreasing IFSS with increasing contact angle). Shin et al. also showed an inverse relation between contact angle and IFSS with different glass fibre epoxy combinations [48]. Park et al. [49] found a strong inverse correlation between water contact angle and ILSS for 4 different silane treated glass fibres and polyester resin.

In the present work, the proposed method to reduce the interlaminar peak traction of the cohesive law is by plasma fluorination of the dry glass fibre fabrics prior to resin infusion. Since the majority of the sizing applied to glass fibres is made up of film former (80-90% by weight), the treatment is primarily of the film former surface. Fluorinated surfaces exhibit hydrophobic wetting properties and weak adhesion to resins such as epoxy or vinylester [44, 50]. The idea is that by introducing fluorine or fluorine containing molecules onto the fibre sizing surface, wetting is delayed and the interaction

between fibre sizing and the resin is delayed. As the resin cures, the molecular mobility of the radicals in the resin is reduced [51]. Due to the delayed interaction with the fibre sizing, the fibre/matrix bond strength is reduced, reducing interlaminar strength properties.

At the macro length scale (millimeters) there are various interlaminar tensile [52, 53] and shear tests ([54]) which may be used to characterise properties such as the interlaminar tensile and shear strengths (peak normal and shear stress, respectively). At this length scale however, it is not purely the fibre/matrix interphase that is characterised, as deformation and failure also occurs in surrounding resin and fibres. In the present work, the curved beam test is used to determine peak normal stress and the short beam shear test is used to determine the peak tangential stress for treated and untreated interfaces. Details are presented in chapter 3.

1.8 Problem statement and objectives

The present work aims to develop a treatment method to control the formation of multiple delaminations in a unidirectional laminate by reduction of the peak cohesive law traction of laminate interfaces. Furthermore, the aim is to demonstrate that the formation of multiple delaminations leads to a significant increase in overall laminate fracture resistance. The guiding principle is to accept that damage occurs and grows in composite laminates. Instead of preventing delamination cracks from initiating, the aim is to slow it down, and perhaps even stop growth altogether by the formation of a fracture process zone that dissipates energy via multiple bridged cracks.

The overall objectives are to:

1. Introduce a fluorine containing layer on the fibre sizing surface by atmospheric pressure plasma.

2. Reduce peak stress of the interlaminar cohesive law.

3. Control the formation of multiple delaminations by reduction of peak cohesive law stress.

4. Show that the formation of multiple delaminations increases fracture resistance by experimental testing.

1.9 Thesis outline

The thesis is structured to follow the three steps taken to achieve a controlled formation of multiple delamination cracks. In chapter 2 the treatment methods are presented. Chapter 3 describes the chemical and mechanical characterisation methods for the treated fibres and composite interfaces, along with a summary of key results. In chapter 4, the J-integral is revisited in for double cantilever beam (DCB) specimens. Furthermore, in chapter 4 the enhancement of fracture resistance by multiple delamination cracks in double cantilever beam specimens is demonstrated. The results are discussed in chapter 5 and final conclusions drawn in chapter 6.

Chapter 2

Plasma fluorination of sized glass fibres

The following chapter focuses on the treatment of sized glass fibre fabrics with atmospheric pressure plasma in a fluorine containing gas. Following an introduction to the plasma and treatment of fibres, two different plasma devices that have been used to treat fabrics are presented. The results of the treatment are presented in chapter 3.

2.1 Introduction to plasma

Plasma is one of the four states of matter [55]. It consists of an electrically conductive ionized (or partially ionized) gas. Non-equilibrium plasma (or non-thermal plasma) is a type of plasma where the electron temperature is far greater than the gas temperature. Electron temperatures may be 10 000 K or higher, whilst the gas temperature can be at room temperature; such 'cold' plasmas can be used for the treatment of polymers [43]. Non-equilibrium plasmas can be generated at both low pressures and at atmospheric pressure [56].

A dielectric barrier discharge (DBD) (also known as a silent discharge) is a common type of atmospheric pressure plasma source [56–60], where a plasma discharge is generated by an alternating current (AC) supplied to electrodes separated by at least one dielectric barrier. The electrodes therefore do not need to be in direct contact with the plasma. This type of plasma device was first used by Siemens in 1857 [61].

During plasma treatment, both etching and surface chemistry modification may occur. One of these two mechanisms may be more dominant than the other, depending on the treated material and plasma treatment conditions [43]. Surface chemistry modification can mean deposition or substitution on the treated surface. During deposition, or plasma polymerization, a layer is built up (polymerized) on the treated surface. If a non-polymerizing gas is used, a substitution reaction may occur on the treated surface, where for example a hydrogen atom on the treated surface is replaced by a radical in the plasma.

The glass fibres treated in this study have a mean thickness of 17 µm and a sizing thickness of $< 1\,\mu m$. For plasma treatment, the treatment depth is normally around

10 nm [43]. Therefore, the treatment will only affect the surface of the sizing layer around the fibre without affecting the glass fibre itself. A schematic of the proposed treatment on the fibre sizing is presented in fig. 2.1.

An interesting development is the use of ultrasonic irradiation of the plasma process to achieve higher treatment efficacy [62]. Introduction of ultrasonic waves may increase molecular mobility near the substrate surface, increasing the treatment effect. Fang et al. [63] showed a reduction by a factor 30 in treatment time required to achieve the same wettability improvement when treating PET films with a DBD plasma in helium (He). Similar effects may be possible with other treatment types such as plasma fluorination.

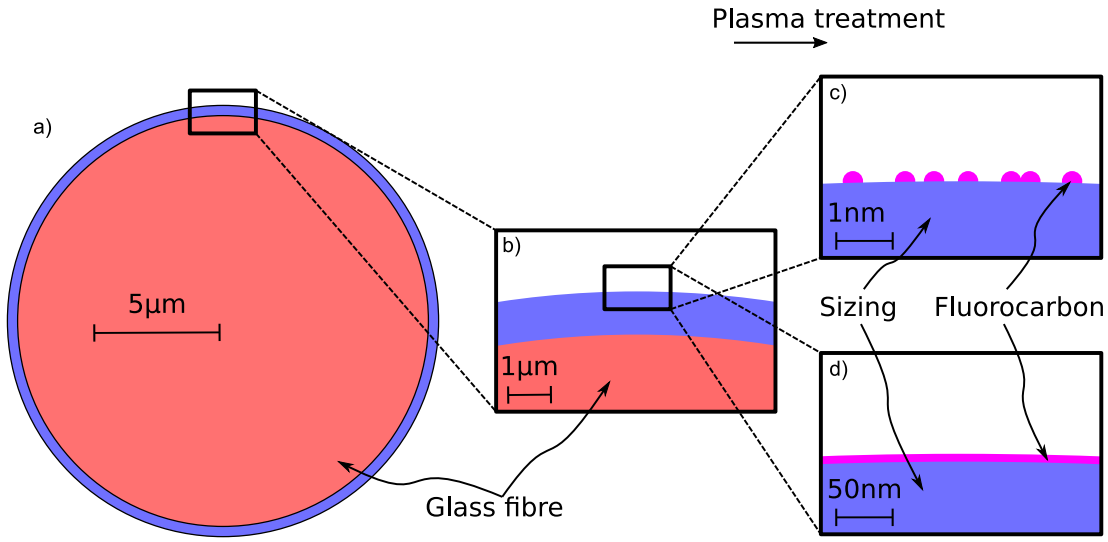

Figure 2.1: Illustration of a glass fibre cross section. **a)** Sized glass fibre prior to treatment, **b)** Close up view of glass fibre sizing layer, **c)** View of sizing surface after plasma treatment and fluorocarbons.

2.2 Materials and treatment overview

A single material system was used for all treatments and characterisation techniques in the present work. A commercially available, sized uni-directional (UD) non-crimp E-glass fibre fabric (W3030 2400tex, Hexcel, Duxford, UK) was used. The fabric has an areal weight of 800 g/m^2 and the fibres have a diamater of 17 µm. Two different plasma sources with different precursor gas mixtures were used to treat the fabrics. For the 'small DBD' a mixture of helium (He) and tetrafluoromethane (CF_4) was used. The 'large DBD' used a mixture of He and octo-fluorobutane (OFB). An overview of the treatments is presented in table 2.1. Details of the DBD devices and gas mixtures

used are presented in sections 2.3 and 2.4.

Table 2.1: Summary of treatments and characterisation techniques used.

Treatment device	Condition name	Condition parameter	Gas mixture
Untreated	A	-	-
Small DBD	B1	50 W	He/CF_4
	B2	100 W	He/CF_4
Large DBD	C1	10 mm/s	He/OFB
	C2	1 mm/s	He/OFB

2.3 Small DBD device

Paper 1 **[P1]** describes the small DBD device and treatment method in detail. A brief summary will be given here.

Preliminary treatment experiments were performed using a plasma device capable of treating specimens up to 50 mm $\times$ 50 mm in size. Short bundles of fabric were placed in the plasma chamber on top of the dielectric barrier (see fig. 2.2). A gas mixture of helium (He) and tetrafluoromethane (CF_4) was introduced into the plasma chamber with a flow rate of 3 SLM (standard liter per minute) of He and 0.23 SLM (CF_4). An alternating-current was supplied by a generator at approx. 40 kHz (Generator 6030. SOFTAL Electronic GmbH, Hamburg, Germany). The treatment time was 60 s for all specimens, with power being used as a variable. Power was controlled to be either 50 W or 100 W. Contamination with ambient air was minimized by enclosing the plasma chamber in a poly(methyl methacrylate) (PMMA) chamber and purging the chamber for approx. 10 s prior to initiating the plasma.

In the plasma treatment process, it is expected that the C-F bonds in the CF_4 are broken and that F radicals are substituted onto the sizing surface [64–66].

2.4 Large DBD device

The DBD device and the tuning of treatment parameters are described in detail in Paper 2 **[P2]**. The applicable fibre treatment and characterisation methods are described in Paper 3 **[P3]**.

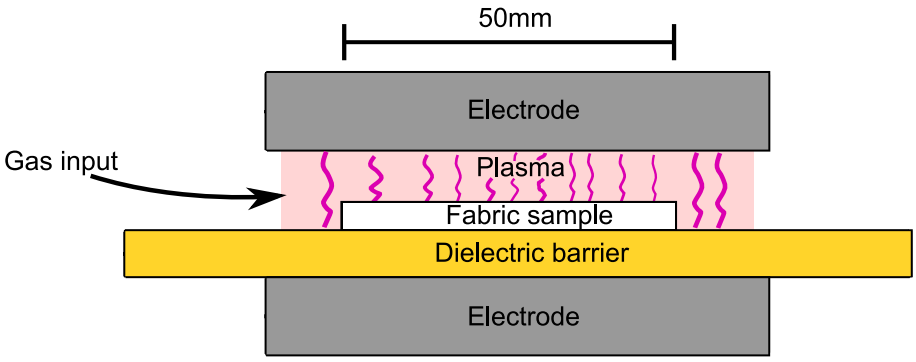

Figure 2.2: Simplified illustration of the 'small' DBD device.

The small DBD device only enabled the treatment of specimens up to 50 mm $\times$ 50 mm. A new DBD device was built in order to enable the treatment of larger sized fabrics, which could be used to prepare larger specimens for mechanical testing, such as the double cantilever beam (DCB) specimens. Rather than making a scaled up version of the 'small DBD' device, which would consume too much power, a system with a movable ground electrode was used (see fig. 2.3a). Such a system allows for treatment of fabrics of any length, the dimension being limited only by the size and travel of the movable electrode. The area that can be treated using the movable electrode in this 'large DBD' device is 280mm x 400mm. The powered static electrode is water cooled and insulated in an alumina dielectric barrier (see fig. 2.3b). A poly(methyl methacrylate) (PMMA) tube surrounds the static electrode and acts as a chamber in which the gas mixture can be contained. The PMMA tube has an opening towards the movable ground electrode, through which the plasma discharge is generated. In fig. 2.4 a side view of the plasma device is shown with and without ambient light present. A clear purple discharge is seen around the electrode.

A different gas mixture was used with the large DBD device: He and octo-fluorobutane (OFB). OFB has been reported to have superior hydrophobic effects compared to CF_4 [64]. OFB has a cyclic structure and it is therefore expected that a C-C bond is broken, opening the cyclic carbon chain, and polymerizing the molecule onto the sizing surface [67, 68]. Plasma polymerization with OFB has been widely used to create hydrophobic or superhydrophobic surfaces on polymeric and metallic substrates [68–70].

Treatment was performed by placing the fabric sample on the movable ground electrode, starting the flow of the gas mixture, initiating the plasma and passing the fabric through the plasma a single time. The treatment condition was controlled by changing the velocity of the movable grounded electrode. In chapter 3 and chapter 4, laminates were made using two different treatment conditions: 1 mm/s (also referred to as high treatment condition) and 10 mm/s (referred to as low treatment condition). The slower treatment condition (1 mm/s) exposes the fibres for a longer time to the plasma and

therefore is more likely to have a larger treatment effect (e.g. more fluorine polymerized).

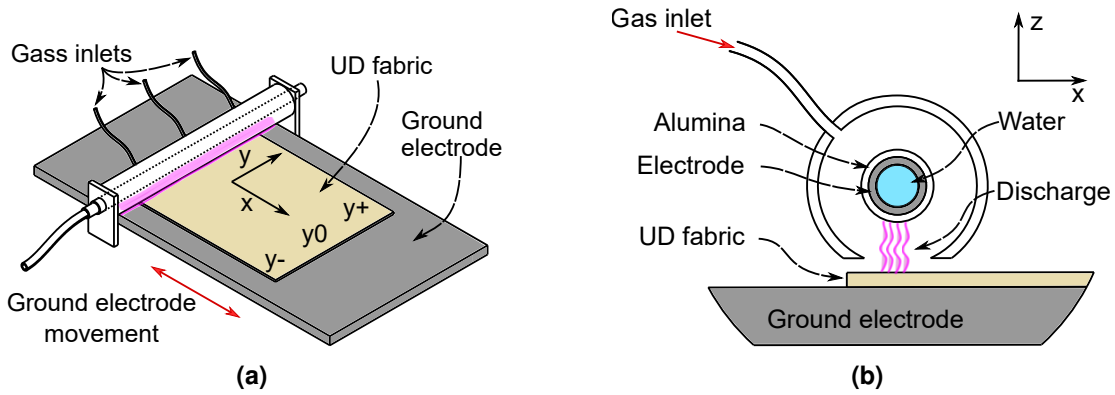

Figure 2.3: Illustration of DBD device with fabric sample. **(a)** 3D visualization of DBD device, indicating the direction of motion of the ground electrode and coordinate system used for treatment measurements. **(b)** Cross sectional view of the DBD device, showing both electrodes and fabric sample. [Source: [38]]

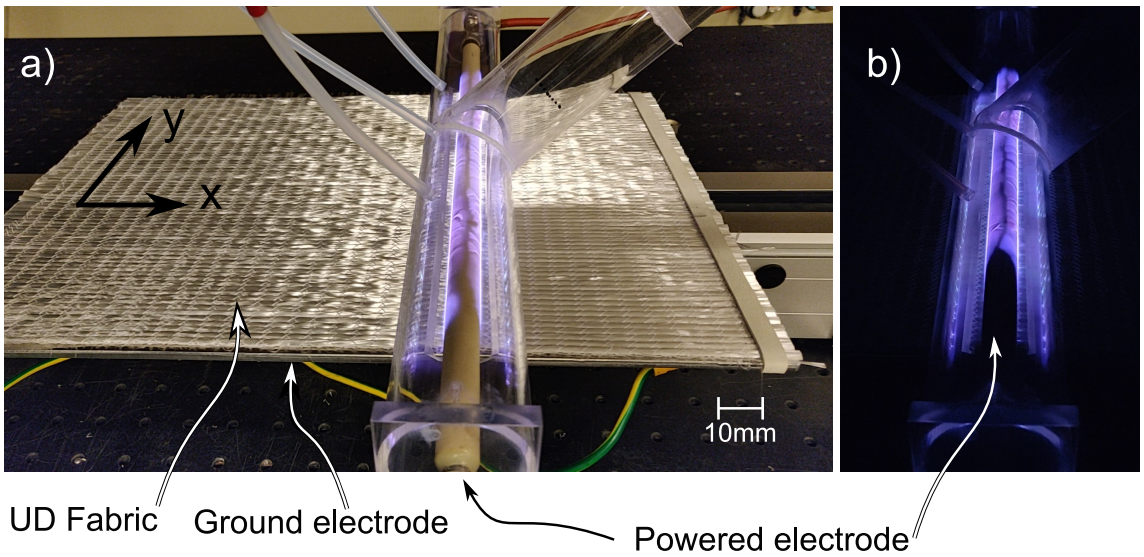

Figure 2.4: Sideview of 'large' DBD device. **a)** Treatment of UD fabric sample (coordinate axes corresponds to fig. 2.3a). **b)** View of plasma discharge around powered electrode without ambient light. Scale bar is accurate for foreground objects only.

Chapter 3

Characterisation of treated glass fibres

In the following chapter the methods to characterize the effect of the plasma treatments on the fibre surfaces are presented. Firstly, a brief overview of commonly employed characterisation techniques is given. Next, the characterisation techniques are introduced for the sizing interface after treatment (section 3.2). The mechanical test methods to characterise the treatment affect on the properties of the fibre composite after infusion and curing are presented in section 3.3. Finally, a summary of the test results for the treatments with the 'small DBD' and 'large DBD' devices are presented in section 3.4. This chapter primarily includes published work from papers **[P1]** and **[P3]**. In addition, some unpublished results are presented, such as the microbond tests, which were not conducted by the author but have a significant effect on the present work.

3.1 Introduction

The treatments presented in chapter 2 can have changed both the physical and chemical structure of the fibre sizing surface. Several methods may be employed to characterise the physico-chemical properties of the surface of (sized) glass fibres. Common chemical analysis techniques include X-ray photoelectron spectroscopy (XPS) [16], time-of-flight secondary ion mass spectrometry (TOF-SIMS) [71] and Fourier transform infrared spectroscopy (FTIR)[72]. These tests may be used to determine the class of sizing and the chemical composition near the fibre surface. For example, XPS can be used to detect elements within the outer 10 nm of a surface whereas TOF-SIMS only samples the outermost molecules (in the order of 10-20 Å). While technically a volume is analysed, the depth is several orders of magnitude smaller than the fibre and sizing (micrometer scale), therefore we will still consider these techniques 'surface' characterisations. By comparing XPS and TOF-SIMS spectra to known sizing, Feih et al. [71] were able to estimate the type of sizing used on their fibres. However, the secretive nature of sizing development means that accurate descriptions of sizing formulae are not openly available or straightforward to determine [73].

Analysing the fibre surface chemically before and after treatment can give an indica-

tion into how the composite will behave after infusing the fibres with resin and curing. However, as noted by Mäder et al. [46], characterising just the fibre surface (nano scale) cannot give the full perspective of how a fibre composite will behave (at micro or macro scale). Therefore it is required to perform mechanical tests on the interphase region that is formed after infusion and curing of the resin. To investigate the influence of sizing on the mechanical properties of the fibre/matrix interphase (micro scale), the sizing may be extracted from the fibre surface using acetone, the extracted size may then be mixed with resin to perform differential scanning calorimetry (DSC), dynamic mechanical analysis (DMA) and nuclear magnetic resonance (NMR) spectroscopy [72, 74]. At the single fibre scale, mechanical tests include the single fibre fragmentation test [75–77], microbond [78, 79], single fibre peel test [80–82], and pull-out [46, 83] and push-out tests [84]. Most of these tests are typically focused on the shear properties (mode II) of the fibre/matrix interphase, with the exception of the single fibre peel test which is a mixed mode problem.

In table 3.1 an overview is presented of a selected number of characterisation techniques that were used to analyse the sized glass fibres before and after plasma treatment. These methods are described in the next section.

Table 3.1: Summary of treatments and characterisation techniques used. Abbreviations: X-ray photoelectron spectroscopy (XPS), Dynamic micro-wetting (DMW), Interfacial shear strength (IFSS), Interlaminar shear strength (ILSS), Interlaminar tensile strength (ILTS), Scanning electron microscopy (SEM).

Treatment device	Condition name	Condition parameter	Gas mixture	Characterisation method					
				XPS	DMW	IFSS	ILSS	ILTS	SEM
Untreated	A	-	-	✓	✓	✓	✓	✓	✓
Small DBD	B1	50 W	He/CF_4	✓	✓	✓			✓
	B2	100 W	He/CF_4	✓	✓	✓			✓
Large DBD	C1	10 mm/s	He/OFB	✓	✓		✓	✓	
	C2	1 mm/s	He/OFB	✓	✓		✓	✓	

3.2 Characterisation of the fibre surface (interface)

In this section, the primary focus is on the dynamic micro-wetting technique developed as part of the thesis work (section 3.2.1). X-ray photoelectron spectroscopy (XPS) and field emission scanning electron microscopy (FE-SEM) are briefly introduced in section 3.2.2 and section 3.2.3, respectively.

3.2.1 Dynamic micro-wetting (DMW)

In the present study, due to lacking equipment to measure the dynamic contact angle by the Whilhelmy plate technique, a novel technique for characterisation of fabric bundles was developed in order to quickly analyse the effect of plasma fluorination of sized glass fibre fabrics. The introduction of fluorine onto the fabric should behave similarly to a polytetrafluoro-ethelyne (PTFE) like layer, with low surface energy resulting in a hydrophobic, or de-wetting, effect. A quick test therefore, is to observe the behaviour of a droplet of resin like liquid when it is placed onto a fabric bundle. A droplet placed on an untreated fabric should wet the fibres quickly whereas a fluorinated fabric is expected to have a slower wetting rate. Similar techniques have been used elsewhere to measure the wetting behaviour of fabrics [48, 85].

The proposed measurement setup involves placing a droplet of test liquid (approx. 1 µL) on the fabric (see fig. 3.1). A video camera with macro lens (CAM100. Crelab Instruments AB, Billdal, Sweden) is used to observe the contact angle, θ, of the droplet on the fabric bundle. The novelty of the dynamic micro-wetting technique lies in the analysis of such a droplet as a function of time. The measured contact angle θ was fitted with an exponential function,

$$cos(\theta) = 1 - A \cdot e^{-\alpha \cdot t}, \tag{3.1}$$

where A and α are fitting parameters and t is time from the droplet is placed on the fabric. The fitting parameter A indicates the state of the droplet at $t = 0$. Since the application of the droplet onto the fabric is difficult to do in a highly reproducable manner, the value of A is not a good parameter to compare different wetting behaviours. Instead, the wetting rate, α, is found to be a more repeatable and robust measure [86].

Wetting tests were performed within one day of plasma treatment. In order to study the long term stability of the treatment, some wetting tests were also performed approximately 6 months after plasma treatment. Between the plasma treatment and contact angle testing, the samples were stored at $21\,^{\circ}\mathrm{C}$ in aluminium foil and sealed in a plastic bag.

3.2.2 X-ray photoelectron spectroscopy (XPS)

XPS was used to characterise the elemental composition of the treated glass fibre surfaces at molecular scale. Measurements were performed using a micro focused monochromatic Al Kα X-ray source (K-alpha, ThermoFischer Scientific, Paisley, UK) with an X-ray energy of 1486.6 eV, resulting in a lateral resolution (minimum spacing

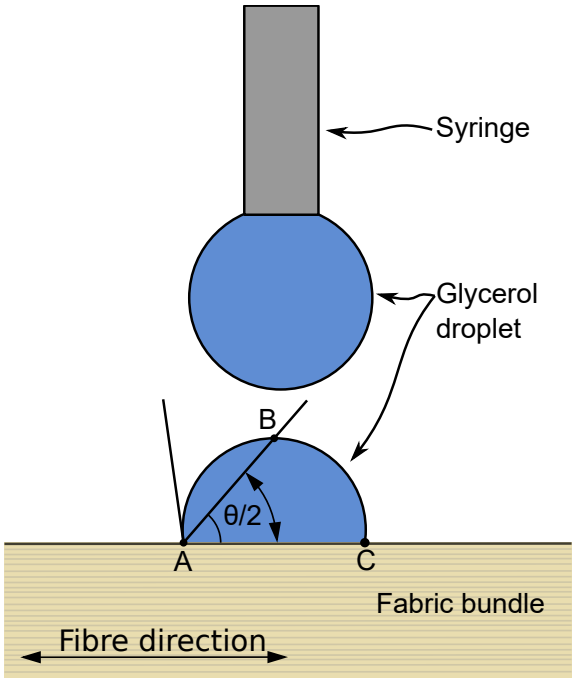

Figure 3.1: Illustration of the dynamic micro wetting test setup. **[[38]]**

at which two features can be recognised as distinct and separate) of 30 μm. Survey analysis was performed using two scans and high resolution C1s spectra were obtained using 30 scans. For analysis of samples treated with the 'small' DBD device, fibres were taken from the bundle interior and exterior (see fig. 3.2).

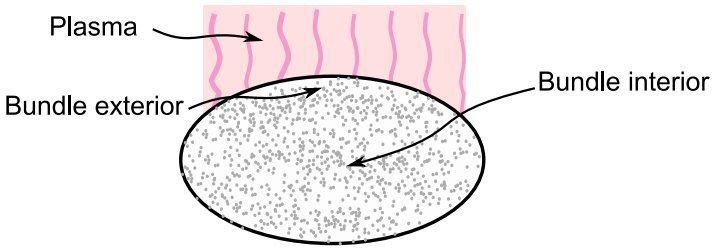

Figure 3.2: Illustration of a fabric bundle cross section with interior and exterior locations for XPS analyses indicated.

3.2.3 Field emission scanning electron microscopy (FE-SEM)

FE-SEM (Zeiss Ultra 55, Oberkochen, Germany) was performed on individual fibres before and after plasma treatment to investigate morphological changes to the sizing surface. Fibres were sputter coated with gold (layer thickness approx. 7 nm) prior to

microscopy.

3.3 Mechanical characterisation of the fibre/matrix interphase and cohesive law

The following section contains an overview of the mechanical test methods performed to characterise the fibre/matrix interphase (section 3.3.1) and peak stress (sections 3.3.4 and 3.3.5). A brief description of the manufacturing of the samples used to determine the peak stress is also included in section 3.3.2.

3.3.1 Microbond

Microbond tests were performed by Dr. Peter Jenkins at the University of Strathclyde in Scotland using shipped samples of plasma fluorinated fibres. The results thereof are not published elsewhere but are of significance to the present thesis. These tests were the earliest mechanical tests performed on fluorinated samples and were central to the choice of continuing with plasma fluorination.

The microbond test is a micromechanical test used to measure the apparent interfacial shear strength (IFSS) of a fibre/matrix interphase. Using a pair of knife edges to hold back the fibre, a fibre is pulled out of a droplet of cured resin as illustrated in fig. 3.3. The method was introduced by Miller et al. in 1987 [78] and further developed by Yang et al. [79]. The apparent IFSS, τ_{app}, is calculated by [78],

$$\tau_{app} = \frac{F_{max}}{\pi D_f L_e}, \tag{3.2}$$

where F_{max}, D_f and L_e are the maximum observed tensile force on the fibre, the fibre diameter and embedded length, respectively. Both the embedded length and droplet diameter are measured using an optical microscope.

3.3.2 Manufacturing of curved beam and short beam shear specimens

In order to determine interlaminar strength properties at the macro scale (peak normal and tangential stress in cohesive laws), the curved beam test and short beam shear

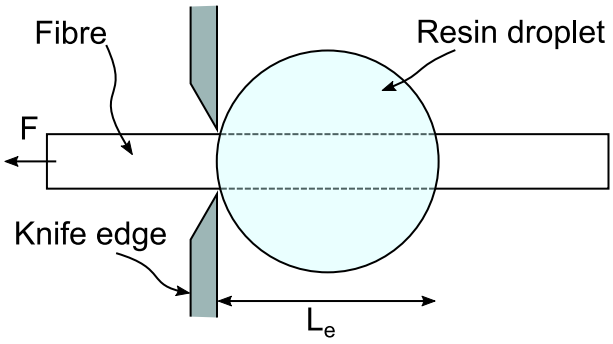

Figure 3.3: Illustration of the micrbond test setup.

test were performed on composite specimens made by treated fabrics and a vinyl ester resin system. The resin system used in this study is a commercial vinyl ester (DION VE1260, Polynt A/S, Sandefjord, Norway). According to the fibre manufacturer technical data sheet, the sizing on the glass fibres is compatible with this resin system [87].

Laminates were prepared using an L shaped steel mould (conform to the ASTM D6415 standard [53]) with a 6.4 mm inner radius (r_i) in the curved section. Four plies of UD fabric were placed on the mould and individually curved around the mould edge to avoid excessive warping of the fabric. The fibres were oriented so as to follow the curvature of the steel mould (x_1 direction in figs. 3.4 and 3.5). The laminates were infused and cured according to resin supplier recommended methods (see paper **[P3]** for details).

A linear elastic FE model of the curved beam test was made in Abaqus/Standard [88] to visualize the stress distribution in the test section of the curved beam. Plane strain elements were used with the following elastic parameters: $E_1 = 51\,\text{GPa}$, $E_2 = 7\,\text{GPa}$, G$= 2.7\,\text{GPa}$ and $\nu_{12} = 0.26$.

Specimens that were made with plasma treated fabrics followed the layup shown in fig. 3.5. Only ply number 3 was treated with plasma, the other plies were kept untreated. The curved beams were vacuum infused on the same day as plasma treatment, typically within 4 hours.

Curved beam specimens were cut to 25 mm width with legs of approx 100 mm length according to ASTM standard D6415 [53]. Short beam shear specimens were cut from the straight portion of the curved beam laminate and followed the dimensional requirements stipulated by ASTM D2344 [54]. This procedure eliminates possible difference in process conditions.

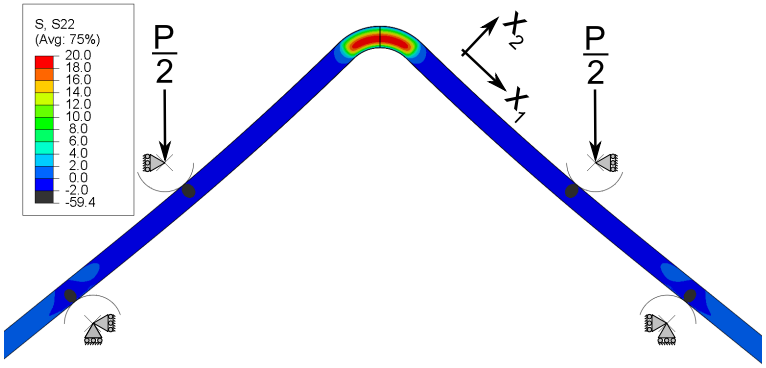

Figure 3.4: Out of plane stress (σ_{22}) distribution of curved beam specimen loaded with pure moments (4 point bending). The coordinate system follows the fibre direction in the curved section, with x_1 in the fibre direction.

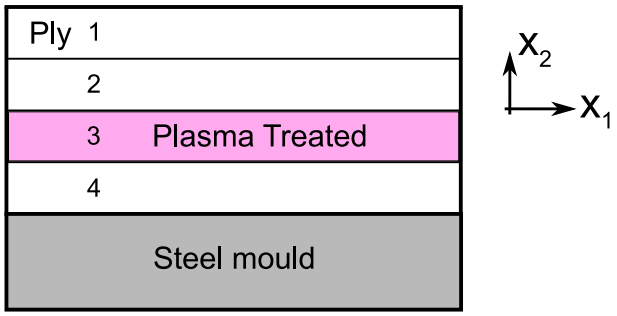

Figure 3.5: Layup used to create curved beam and short beam shear samples. x_1 indicates the fibre direction and x_2 the thickness direction.

3.3.3 Fibre volume fraction (FvF) and microscopy

Samples were cut from the cured laminates using a diamond tipped saw blade. Fibre content and void content was determined by the ignition loss method as per ASTM standards D2584 [89] and D3171 [90]. Environmental scanning electron microscopy (ESEM) was performed using an EVO 60 (Zeiss, Oberkochen, Germany). Microscopy samples were first cut using a diamond tipped blade and subsequently polished (and rinsed ultrasonically) in stages to a final grit of 1 µm, before sputter coating with carbon (layer thickness approx. 15 nm).

3.3.4 Macroscale mechanical characterization: Curved beam testing

The curved beam test is a four point loading test that applied a pure moment to a curved composite beam (illustrated in fig. 3.6). A concentrated stress in the x_2 is created which initiates a mode I delamination crack close to the neutral axis of the beam. However, as shown by Lu et al. [91], the mode mixity (defined as the phase angle of mode I and mode II stress concentration factors), ψ, increases changes linearly with the angle, Φ (see fig. 3.6), which means that only the crack initiation is a valid measure of the mode I interlaminar properties.

A closed form solution by Lekhnitskii for curved beams with cylindrical anisotropy may be used to determine the out of plane stress σ_{22} [53, 92],

$$\sigma_{22} = \frac{-M}{w r_o^2 g}\left[1 - \frac{1-\rho^{\kappa+1}}{1-\rho^{2\kappa}}\left(\frac{r_m}{r_o}\right)^{\kappa-1} - \frac{1-\rho^{\kappa+1}}{1-\rho^{2\kappa}}\rho^{\kappa+1}\left(\frac{r_m}{r_o}\right)^{\kappa+1}\right], \tag{3.3}$$

where M is the applied moment, w is the specimen width and the parameters are

$$g = \frac{1-\rho^2}{2} - \frac{\kappa}{\kappa+1}\frac{(1-\rho^{\kappa+1})^2}{1-\rho^{2\kappa}} + \frac{\kappa\rho^2}{\kappa-1}\frac{(1-\rho^{\kappa-1})^2}{1-\rho^{2\kappa}} \tag{3.4}$$

$$\kappa = \sqrt{\frac{E_{11}}{E_{22}}} \tag{3.5}$$

$$\rho = \frac{r_i}{r_o} \tag{3.6}$$

and

$$r_m = \left[\frac{(1-\rho^{\kappa-1})(\kappa+1)(\rho r_o)^{\kappa+1}}{(1-\rho^{\kappa-1})(\kappa-1)(\rho r_o)^{-(\kappa-1)}}\right]^{\frac{1}{2\kappa}}, \tag{3.7}$$

where E_{11} and E_{22} are the moduli in the fibre (x_1) and interlaminar (x_2) direction; and r_i and r_o are the inner and outer radius of the curved section, respectively.

Because pure bending is applied, the stress σ_{22} in eq. (3.3) is independent of angular position. An approximate method for calculating the peak stress σ_{22} is used in the

ASTM standard [53]

$$\sigma_{22} = \frac{3M}{2wt_C\sqrt{r_i r_o}}, \tag{3.8}$$

where M is the applied moment; t_C and w are the thickness and width; and r_i and r_o are the inner and outer radius of the curved section, respectively. During the experiment, M is gradually increased. At the onset of crack formation (typically associated with a sharp load drop [53]), σ_{22} is taken to be equal to the peak cohesive traction $\hat{\sigma}_n$.

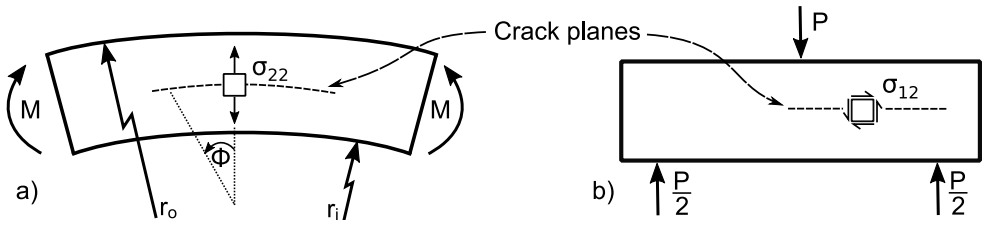

Figure 3.6: Stress state of **a)** curved beam and **b)** short beam shear sample. The dashed line in both illustrations indicate the plane where maximum stress occurs. This plane coincides with the interface between plies 2 and 3 shown in fig. 3.5. Adapted from: [38]

The valid failure mode is a mode I type delamination occurring in the curved region. Typically, the delamination process is sudden and causes one or more delamination form. The out-of-plane stresses σ_{22} in the curved section are greatest slightly below the neutral axis of the beam (between ply 2 and 3 in fig. 3.5). The thicker the layup is, the further the peak stress location moves towards the inner radius i.e. towards ply 3 [53, 92]. In order to keep the peak stress as close to the interface between ply 2 and 3 as possible, a thin 4 ply laminate was used. To prevent excessive rotations in the laminate, a stainless steel dog bone shaped stiffener sleeve was used to support the legs of the curved beam specimens [93].

3.3.5 Short beam shear

The short beam shear test is a common three-point bending experiment, illustrated in fig. 3.6. A distributed shear stress is created between a centre roller and the two lower roller supports. Shear cracks typically form near the mid-plane, where the highest shear stress is located [53]. The mid-plane shear stress may be calculated by [54],

$$\sigma_{12} = \frac{3}{4}\frac{P}{bh}, \tag{3.9}$$

where (P), (b) and (h) are the applied load, specimen width and specimen thickness, respectively. At the load level where shear cracks form, σ_{12} is taken to be equal to the peak value of the cohesive shear traction, $\hat{\sigma}_t$.

3.4 Summary of results

The summary of results is divided into two groups based on the DBD device used for the treatment. The preliminary study was performed using the 'small' DBD device whilst the large DBD device was still under development. The findings from the work using the small DBD device are part of **[P1]**. Fibre treatment using the large DBD device and subsequent mechanical characterisation are the basis for **[P3]**. An overview of the treatments and characterization techniques used can be found in table 3.1

3.4.1 Small DBD device

Hottentot Cederløf, D. J., Kusano, Y., and Fæster, S. (2019). Fluorination of sized glass fibres for decreased wetting by atmospheric pressure plasma treatment in He/CF_4. *Journal of Adhesion*, 96(1-4), pp. 2–12.

- **XPS:** Measurements were taken from fibres located within a fibre bundle and from the fibre bundle exterior. The 50 W treated specimens showed a fluorine introduction of (1.4–1.5 atomic percent (at.%)), for the bundle interior and exterior, respectively (see table 3.2). A larger amount of fluorine was detected for 100 W treatment; 3.6–5.3 at.% for the interior and exterior, respectively. For both the treatment conditions, the oxygen content was found to be slightly increased, whereas the silicone content (most likely a contaminant) was absent.

Table 3.2: Elemental composition of glass fibre surface before and after treatment.

Power [W]	Bundle location	Elemental composition [at.%]						O:C	F:C
		C	O	F	N	Si	Ca		
-	Interior	76.0	22.9	0.0	0.0	1.1	0.0	0.29	0
	Exterior	76.8	21.9	0.0	0.0	1.3	0.0	0.29	0
50	Interior	74.7	23.3	1.4	0.0	0.6	0.0	0.31	0.040
	Exterior	75.1	23.4	1.5	0.0	0.0	0.0	0.36	0.043
100	Interior	72.9	23.5	3.6	0.0	0.0	0.0	0.33	0.055
	Exterior	71.1	23.1	5.3	0.4	0.0	0.1	0.32	0.056

- **Microbond test**: Microbond of the samples treated in the small DBD device showed a clear reduction in interfacial shear strength (IFSS) with increasing treatment power (see fig. 3.7). The decreasing trend is approximately linear with treatment power. This indicates that more fluorine introduced onto the fibre surface decreases the mechanical interaction between resin and fibre.

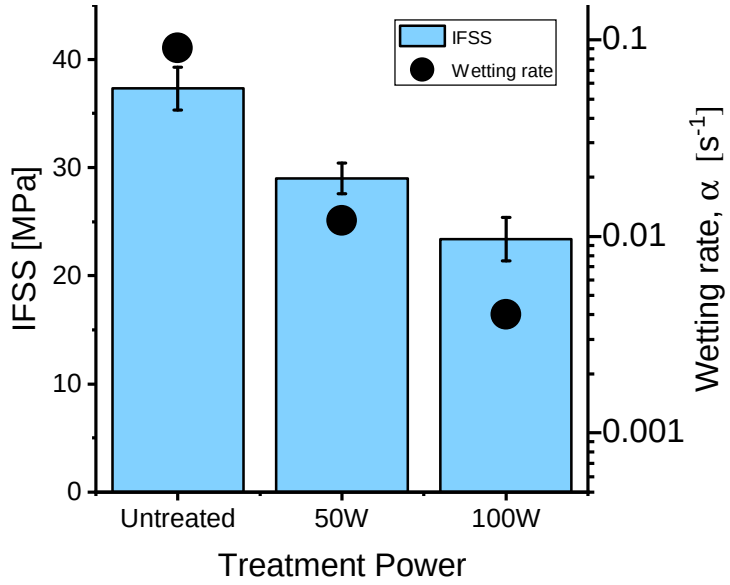

Figure 3.7: Microbond and dynamic micro wetting results. Microbond data from P. Jenkins (personal communication).

- **DMW:** The dynamic micro-wetting rate, α, is plotted together with the microbond results in fig. 3.7. Note the logarithmic axis for the wetting rate. A decreasing α is observed with increasing treatment power. The samples with a smaller α, i.e. a slower wetting behaviour, were also observed to have higher initial contact angles, θ (similar to the 1 s column in fig. 3.8).

- **FE-SEM:** No clear morphological change was observed for for fibres subjected to either treatment. Both treated and untreated specimens showed fine surface cracks in the order of 100 nm-200 nm (see paper **[P1]** for micrographs).

3.4.2 Large DBD device

Hottentot Cederløf, D. J., Kusano, Y., and Sørensen, B.F. (2021). Control of interfacial peak stress by atmospheric pressure plasma treatment. *In manuscript/Submitted to Journal of Composite Interfaces*.

All treatments consisted of exposing the fabric to the plasma one time. The treatment condition of 10 mm/s corresponds to a faster treatment and therefore shorter exposure to plasma than the 1 mm/s treatment. The 1 mm/s condition is therefore more significant because of the longer exposure to the plasma. To ease readability the treatment condition of 10 mm/s is referred to as the 'low treatment' and the 1 mm/s treatment condition as the 'high treatment', to reflect the severity of the treatment, rather than the treatment speed.

- **XPS:** Fluorine was successfully polymerized onto the fibre sizing surface as shown in table 3.3. Mean fluorine content was increased from 0.0at.% to 1.7at.% for the low treatment. For the high treatment condition, a mean fluorine content of 10.3at.% was measured. With a slower treatment speed and thus longer exposure time to the plasma, more fluorine is polymerized to the fibre surface. A large variation however, was observed across the electrode width (y-direction in fig. 2.3a). For the 1 mm/s treatment at the most extreme edges of the electrode, fluorine content was 4.4at.% in the (Y-) location and 17.3at.% in the (Y+) location. For both the treatment conditions, the oxygen content was decreased compared with the untreated fibres.
- **DMW:** It was observed that for the high treatment condition often the droplet of test liquid remained on the fibre bundle surface for more than 10-15 minutes. Droplets placed on untreated fabric bundles would be absorbed by the bundle in less than 60 s. A side-by-side comparison is presented in fig. 3.8 showing a typical dynamic micro-wetting experiment. The top images show an untreated fabric sample and the lower images are from a fabric with high treatment. Images are frames taken at 1 s, 30 s, and 60 s after placement of droplet. Wetting tests performed on fabrics with high treatment condition, approximately 6 months after treatment, showed similar low wetting rates. In comparison with the untreated fibres, the mean dynamic micro-wetting rate showed a reduction by a factor 7 for the fibres with low treatment and a factor 157 for the high treatment (see table 2 in paper **[P3]**).

Table 3.3: Elemental composition of glass fibre surface before and after treatment with large DBD device. Source: paper **[P3]**.

Treatment	Position	Elemental composition [at.%]					
		C1s	O1s	F1s	Si2p	F:C ratio	O:C ratio
Untreated		74.5	25.5	0.0	0.0	0.00	0.34
10 mm/s (low treatment)	Y+	72.6	20.8	4.4	2.2	0.06	0.29
	Y0	77.7	20.6	0.5	1.1	0.01	0.27
	Y-	75.9	22.0	0.0	1.6	0.00	0.29
	mean	75.4	21.1	1.7	1.7	0.02	0.28
1 mm/s (high treatment)	Y+	63.4	18.0	17.3	1.2	0.27	0.28
	Y0	68.6	21.4	9.3	0.7	0.14	0.31
	Y-	72.6	23.0	4.4	0.0	0.06	0.32
	mean	68.2	20.8	10.3	0.6	0.15	0.31

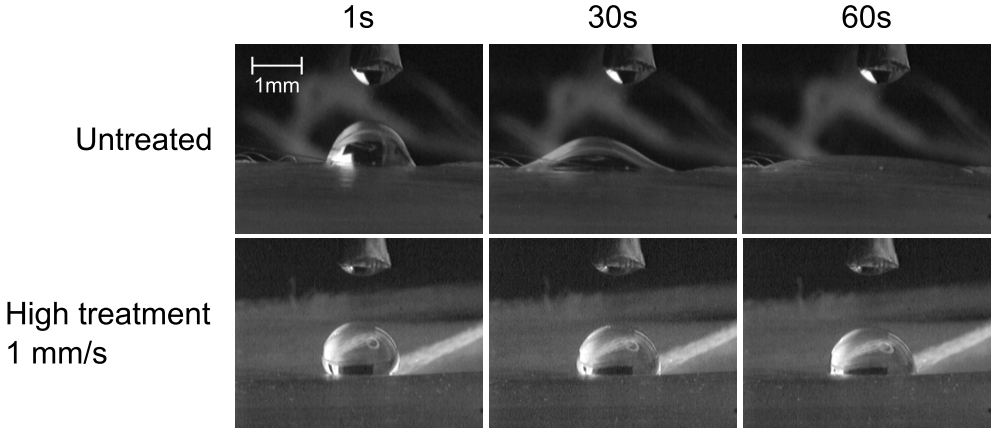

Figure 3.8: Images from the dynamic micro-wetting experiment showing evolution of droplet over time (frames taken at 1 s, 30 s, and 60 s after droplet placement). A comparison of untreated fabrics and a fabric with high treatment is presented.

- **Curved beam:** For the high treated specimens, failure always occurred on the plasma treated interface, i.e. between ply 2/3 or between ply 3/4 (examples of failed specimens are shown in fig. 3.9). With untreated specimens, failure occurred randomly through the sample thickness. In all cases, both treated and untreated, failure was sudden and often multiple delaminations were observed. The peak normal stress, $\hat{\sigma}_{22}$, for the low treatment condition did not show a statistically significant reduction with respect to the untreated fibres (see table 4 in paper **[P3]**). However, for the high treatment condition a statistically significant reduction in $\hat{\sigma}_{22}$ was found. The mean value of $\hat{\sigma}_{22}$ for all the specimens with the

high treatment condition was 12.8% lower than for the untreated specimens.

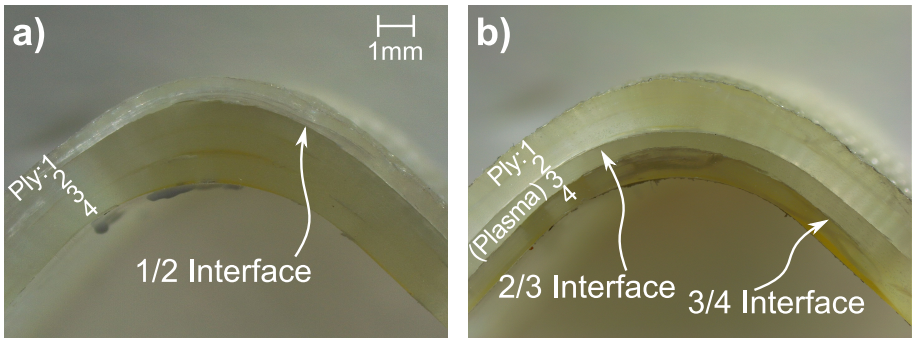

Figure 3.9: Images taken of curved beam samples after failure. **a):** Untreated specimen with failure at the interface between ply 1 and 2. **b):** Specimen where ply 3 has been subject to high treatment prior to infusion, delamination visible at interfaces between plies 2 and 3, and between plies 3 and 4.

- **Short beam shear:** Similar to the curved beam specimens, failure occurred at multiple lamina interfaces and occasionally within laminae (shown in fig. 3.10). In comparison with the untreated specimens, the mean peak shear stress, $\hat{\sigma}_{12}$, has decreased with 2.6% for the low treatment case and 4.2% for the high treatment case. The decrease in $\hat{\sigma}_{12}$ was only statistically significant for the specimens with high treatment.

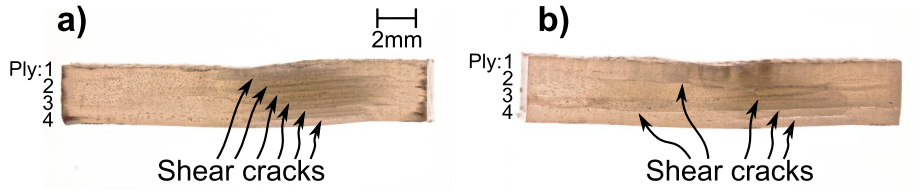

Figure 3.10: Images taken of short beam shear samples after testing. Multiple parallel shear cracks are visible. Images have been edited by increasing micro contrast and sharpening. **a):** Untreated specimen. **b):** Specimen with high treatment condition.

- **SEM:** Microstructural observations of curved beam cross sections did not show an increase in void content for either of the composites made with treated fabrics. This finding is further supported by fibre volume fraction analysis. For all specimens, untreated and treated, the void content was between 0.7-0.8% with a standard deviation of 0.1%. See figure 6 in **[P3]** for micrographs.

Chapter 4

Enhanced fracture resistance by controlled multiple delaminations

In this chapter the methodology and results are presented for testing the fracture resistance of laminates which contain a plasma fluorinated ply. A brief introduction to the double cantilever beam (DCB) test is first given. The layup and manufacturing of the specimens is shown together with the DCB test procedure in section 4.2. Finally, the results are presented in section 4.3. The contents of this chapter are not published elsewhere.

4.1 Background

The double cantilever beam loaded with uneven bending moments (DCB-UBM) is a versatile test specimen used to determine fracture properties of bondlines and composites [37]. Pure moments are applied to the specimen, as shown in fig. 4.1, resulting in crack growth initiated at the tip of the pre-crack. The application of pure bending moments allows for stable cracks growth, independent of crack length.

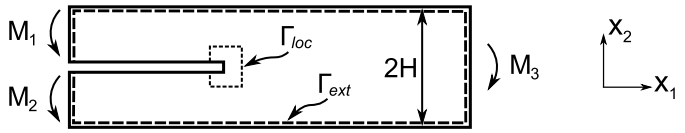

Figure 4.1: DCB-UBM specimen loaded with uneven pure bending moments. Two integration paths for the J integral are shown.

The path independence of the J integral [34], means that the J integral evaluated around the external boundaries of the DCB specimen (path Γ_{ext}) is equal to the J calculated along a path just outside the fracture process zone (FPZ), Γ_{loc} (shown in fig. 4.1). In the presence of large scale fibre bridging there are two contributions to J: crack tip cracking and crack surface tractions from the bridging fibres. If we set the path Γ to cover the full fibre bridging zone and the crack tip (as illustrated in fig. 1.9), then it will combine the contributions to J from the crack tip and the bridging zone [94],

$$J_{ext} = J_{loc} = J_{tip} + J_{bridge}. \tag{4.1}$$

For a DCB specimen loaded purely with moments, the J integral evaluated around the path, Γ_{ext}, under plane stress conditions is [37]

$$J_{ext} = \frac{21(M_1^2 + M_2^2) - 6M_1M_2}{4B^2H^3E} \quad \text{for} \quad |M_1| < M_2, \tag{4.2}$$

where, $M_3 = -(M_1 + M_2)$, and M_1 and M_2 are the applied moments shown in fig. 4.1; B, H and E are the beam width, thickness and Young's modulus in x_1 direction for orthotropic materials, respectively. This is the solution for the J integral for mixed mode conditions. For mode I loading conditions the moments M_1 and M_2 are equal in magnitude but opposite in direction ($M_1 = -M_2$) (shown in fig. 4.2). As a result, $M_3 = 0$ and eq. (4.2) reduces to [25]

$$J_{ext} = \frac{12M^2}{B^2EH^3}. \tag{4.3}$$

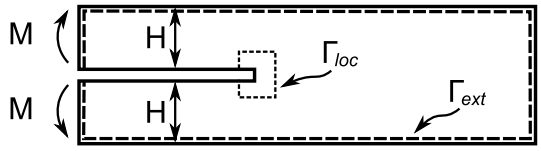

Figure 4.2: DCB loaded with moments under pure mode I conditions.

4.2 Methodology

4.2.1 Manufacturing

DCB specimens were prepared using 20 plies of uni-directional (UD) (fibres in x_1 direction) fabrics and a PTFE slipfoil (WL4900B, AIRTECH Europe Saarl, Differdange, Luxembourg) (13 µm thick) inserted at the mid-plane (between ply 10 and 11, see fig. 4.3). The slipfoil length, a_f, was 100 mm. The following layup was used [(UD-A)$_5$/(UD-B)$_5$]$_S$. UD-A is a unidirectional fabric with areal weight 1397 g/m^2 (SE3030 2400tex, Owens Corning, Zele, Belgium) and UD-B is a unidirectional fabric with an

areal weight of 819 g/m^2 (SE3030 2400tex, Hexcel, Duxford, UK). Both fabrics have the same fibre and sizing formulation, and are compatible with the vinyl ester resin system used for infusion. Fabric UD-B is the same fabric described in section 2.2 which was used for the treatment characterisations in chapter 3.

The layup for specimens with a plasma treated ply is shown in fig. 4.3. The plasma fluorinated ply was placed one ply below the DCB midplane, i.e. ply 9. This was done to preserve an untreated interface for the primary crack. Ply 10 is thus expected to act as a bridging ply. A bridging ply is defined as a ply, spanning the full width of the specimen, which connects two opening faces of a delamination. It is similar in concept to a bridging fibre or ligament.

Due to size restrictions of the large DBD plasma device it was not possible to treat the full length of the fabrics. The length of the treated area (a_p in fig. 4.3) was approximately 290 mm. Two plates were made using plies treated with plasma. The plasma treatment conditions are described in section 2.4 and are the same as the conditions used in the characterisation chapter (chapter 3). For reference: the 'low' treatment condition corresponds to a treatment velocity of 10 mm/s and the 'high' treatment condition corresponds to a 1 mm/s treatment velocity (see table 3.1).

Laminates were laid up by hand on a glass plate prepared with release agent (ZYVAX-slipcoat WATER SHIELD, Granudan ApS, Stenløse, Denmark). A perforated peel ply (AeroFilm PP230, Easy Composites EU B.V., Rijen, The Netherlands) was placed on top of the fabric stack and partially covered with an infusion mesh (FM100, Easy Composites EU B.V., Rijen, The Netherlands) before sealing with a vacuum bag.

A commercial vinylester (DION VE1260, Polynt A/S, Sandefjord, Norway) was used for infusion. The resin was mixed with an accelerator (Norox PBC21, United Initiators GmbH, Pullach, Germany) (2.5% by weight) before degassing for approximately 5 min. The resin infusion was performed with an outlet vacuum pressure of 850 mbar until the fabrics were fully wetted. Then the vacuum pressure was reduced to 600 mbar before sealing the inlet and outlet. Laminates were cured at room temperature for 24hrs followed by a 16hr postcure at 60 °C.

Final plate dimensions were 280 mm $\times$ 600 mm (x_3 and x_1 directions in fig. 4.3). 7 DCB specimens (30 mm width x 560 mm length) were cut from each plate. Steel grip mounts (for the loading arms) were attached to the DCB specimens using 4 screws and an adhesive layer (Scotch Weld DP360, 3M, Copenhagen, Denmark). Extensometer pins were mounted at the end of the slipfoil (see fig. 4.4).

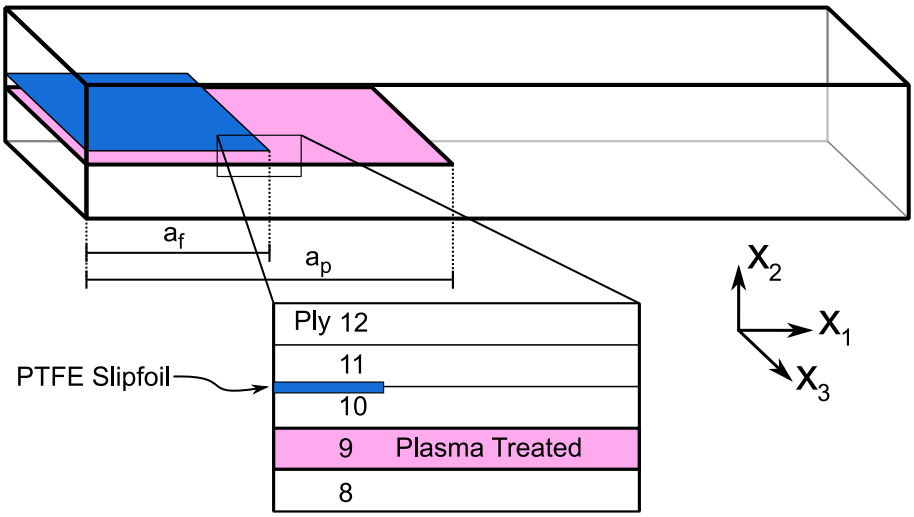

Figure 4.3: Drawing of layup, illustrating PTFE slipfoil insert and plasma treated ply. a_f is the initial slip foil length. a_p is the portion of ply 9 that has been plasma treated (ply 9 is 560 mm in length like the other plies, but only around 280 mm has been plasma treated.)

4.2.2 Microscopy and fibre volume fraction analysis

Laminate quality was investigated using the same ESEM procedure as described in section 3.3.3. Fibre weight fraction (FwF) was determined according to the ASTM method D3171 [90]. 4 FwF samples were taken from the test region in each panel.

4.2.3 Test procedure

Specimen width, B, and height, H, were measured using knife edge calipers at 5 locations along the beam length. An extensometer with max opening of 10 mm ($\pm 1\%$) (2620-601 series, Instron GmbH, Darmstad, Germany) mounted on steel pins near the edge of the slip foil recorded end-opening. Two acoustic emission (AE) sensors ((1283 USB AE Node with R15-α sensors, Physical Acoustics Ltd., Cambridgeshire, UK) were mounted at 20 mm and 260 mm from the slip foil edge. A laptop running AEwin^{TM} software (Mistras Group, Princeton Jct., USA) was used for data acquisition with the following timing parameters: 50 µs Peak Definition Time, 100 µs Hit Detection Time, and 300 µs Hit Lockout Time. In the results, the number of AE 'counts' is used; this is the number of times the detected AE signal crosses a threshold value of 45 dB.

Two Nikon D7500 digital single lens reflex (DSLR) cameras with 20.9 Mega pixel sensors were used to video record the experiments at 30 frames per second (fps). One camera recorded the whole specimen, whilst one was used to record a zoomed in

portion around the slip foil edge (approx. 80 mm $\times$ 140 mm).

A custom loading frame was used to perform the DCB tests under pure mode I loading. The specimen was loaded by translating the movable lower beam (see fig. 4.4) at a constant rate of 5 mm/min. A series of pulleys and a single wire applies a force couple to the loading arms (see fig. 4.4). The test configuration is described in greater detail elsewhere [37]. The load, F, was measured using two load cells (each 5 kN) with a data acquisition frequency of 20 Hz. Since a single steel wire is used in the test rig, there should be a constant force in the wire and the two load cells should measure the same load, F. Any load difference may be attributed to friction in the steel rollers used to guide the wire.

The described DCB test method is susceptible to error when the grips translate in the x_2 direction (see fig. 4.4). The error is partially due to a lateral force in the x_2 direction, similar to an archer's bow when it is drawn back. As the force in the x_2 direction increases, it applies a negative moment to the crack tip. The moment arm of the lateral force increases with increasing crack length. In addition, a shear stress component (σ_{12}) is introduced to the DCB arms due to the lateral force. As a result the moment in the DCB arms is overestimated and dependent on crack length, thereby overestimating the J value. This error is mitigated by maintaining small x_2 displacements of the loading grips.

Data reduction was performed using eq. (4.2). The mean B and H of each specimen was used to calculate the J value. A Young's modulus of 43 GPa was used. To avoid errors due to large deflection (in x_2 direction) of the grips [37], the data series for the extensometer opening were truncated at 5 mm opening.

After the initial round of DCB tests, the grip mounts were repositioned 150 mm in the positive x_1 direction (see fig. 4.4). Furthermore, the pins for mounting the extensometer were repositioned to the new crack tip. This was to test the steady state J value as the delamination(s) transitioned from the treated plasma interface to the untreated section of the DCB specimen (a_p in fig. 4.3). The reason for moving the grips is that the error in determining the applied moment becomes significantly large with large deflection of the grips in the x_2 direction [37]. Moving the grips further down on the specimen reduces this translation in the x_2 direction under testing.

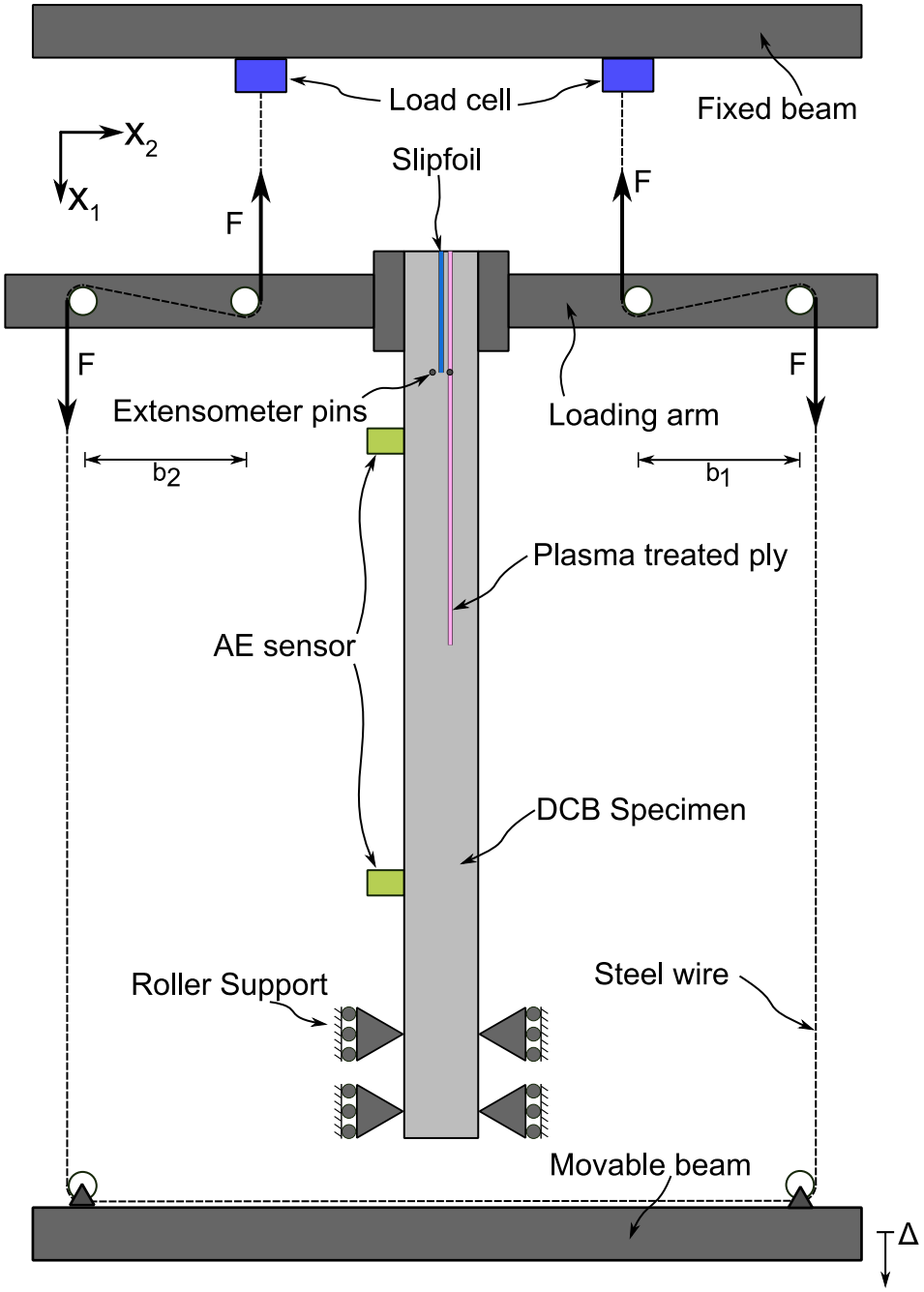

Figure 4.4: DCB test setup. Not to scale.

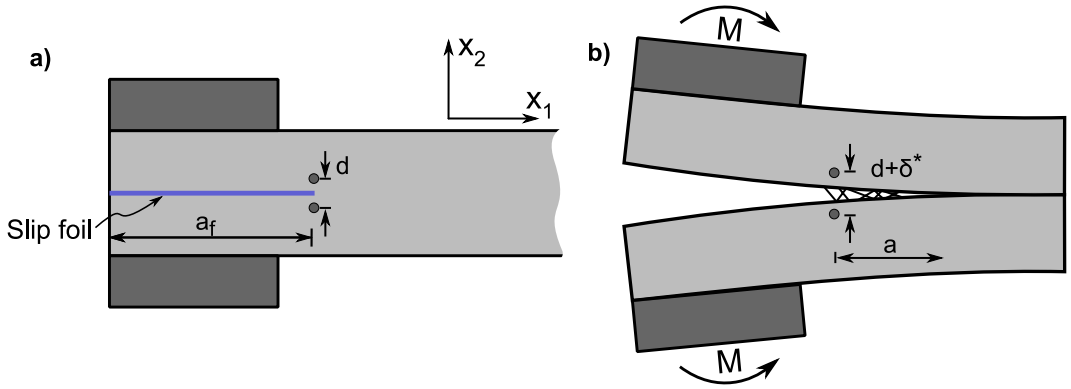

Figure 4.5: Mode I DCB specimen in unloaded and loaded (with moment M) configuration. **a)** Unloaded DCB with slipfoil before crack growth. Initial pin distance, d ad slipfoil length, a_f. **b)** Loaded DCB with bridged crack, illustrating end-opening δ* and crack length a.

4.3 Results: DCB with multiple cracks

The colors used in this section are kept constant for the three conditions: **Green = Untreated**, **Blue/dashed blue = low treatment** and **Red/dashed red = high treatment**.

After infusion, a dry area was observed near the outlet region of the panel (this was consistent for each of the 3 panels). The dry region was in the ply closest to the steel mould (ply 1, see fig. 4.3). Repairs were made by filling the dry spots with cyanoacrylate adhesive and curing the adhesive before mounting the loading grips. Since the dry region was near the surface, away from the test region and expected crack planes, the panels were still deemed fit for testing after the necessary repairs. Fibre weight fraction results (measured away from the dry areas) are presented in table 4.1 These show a consistent fibre weight content of $75.8 \pm 1.1\%$.

Table 4.1: Fibre weight fraction result for DCB series.

Treatment	Fibre weight		Matrix weight	
	Mean [%]	SD	Mean [%]	SD
Untreated	74.7	0.1	25.3	0.1
Low treatment	76.9	0.1	23.1	0.1
High treatment	75.9	0.1	24.1	0.1

4.3.1 First test series: pristine DCB specimens

All specimens (treated and untreated), initiated a single delamination at the slipfoil edge. In fig. 4.6, the J vs end-opening curves are presented for the untreated specimens. Two of the specimens (indicated in the plot with dashed lines) showed a combination of multiple cracks and large scale fibre bridging. These two specimens are deemed outliers and not included in the calculation of the mean J for the untreated series.

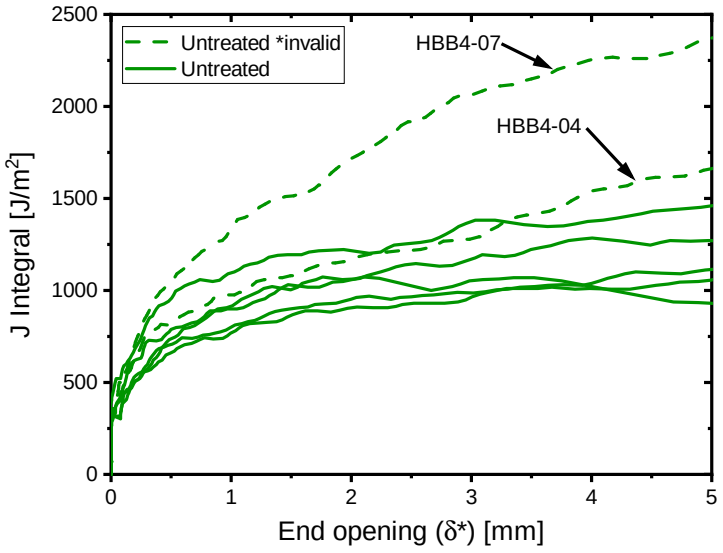

Figure 4.6: Fracture resistance of untreated laminates as a function of end-opening. The dashed lines labelled with HBB4-04 and HBB4-07 are untreated DCB specimens that developed two cracks with large scale fibre bridging.

Specimens with the high treatment condition all showed formation of a secondary delamination on the plasma treated interface, with large scale fibre bridging. In treated specimens secondary delaminations would typically initiate after a primary crack growth of approx. 30 mm. When the secondary delamination was forming, the primary delamination would arrest completely. As loading continued, J increased and the secondary crack grew and developed a bridging zone, eventually the primary crack would resume growth (in the wake of the secondary crack).

Right after initiation, secondary cracks were observed to grow in both the positive and negative x_1 direction. Growth in negative x_1 direction was typically arrested after growing around 5 mm in negative x_1 direction, whilst crack growth in the positive x_1 direction continued with increasing applied moment.

A series of images taken from the video recording of specimen HBB1-01 is presented in fig. 4.7. Close up images of the secondary crack formation and ply bridging are presented in fig. 4.8. A large amount of fibre bridging is observed for both the primary and secondary delaminations. This observation was consistent for the other high treatment specimens. For the low treatment specimens and untreated specimens, less fibre bridging was observed. Occasionally for the untreated and low treatment specimens, bridging bundles were observed i.e. large bridging ligaments. This was especially pronounced in specimen HBB4-07 (see fig. 4.9a).

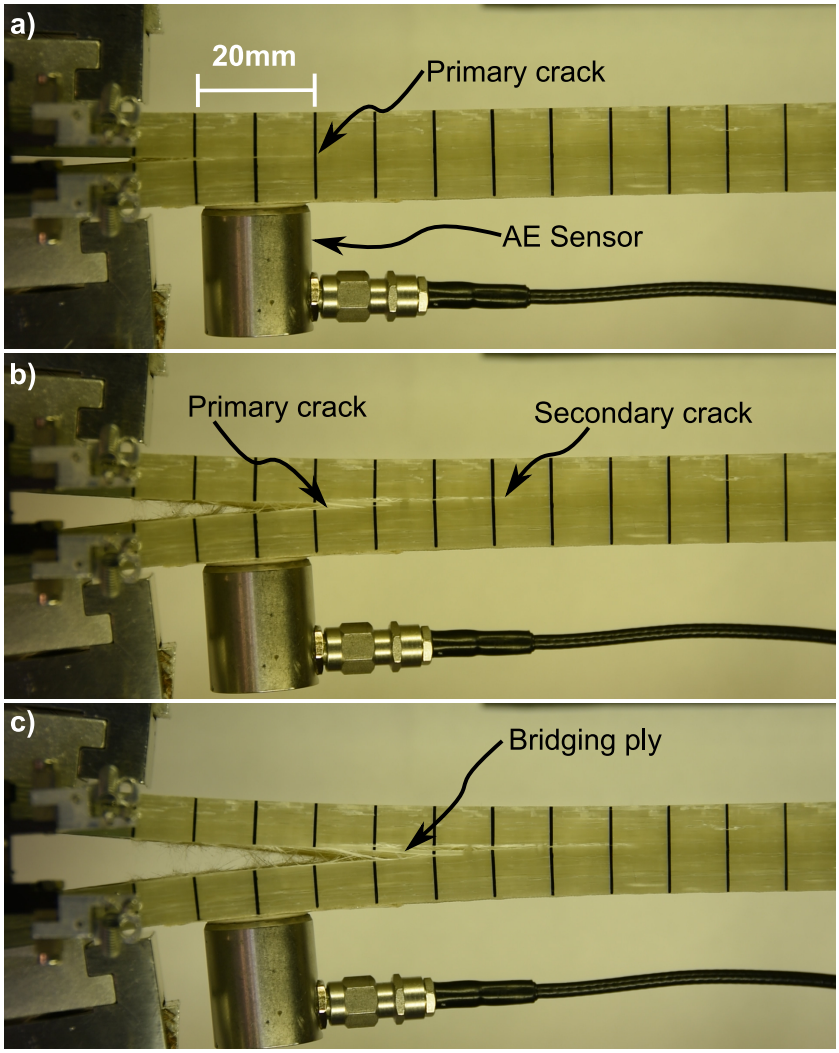

Figure 4.7: Crack propagation of sample HBB1-01 (high treatment). **a)** J=1307 J/m^2, **b)** 2544 J/m^2 **c)** J≈3000 J/m^2. J value in subfigure **c** is approximate due to large end-opening (>5 mm), i.e. large displacement in x_2 direction.

Specimens with the low treatment condition showed multiple delaminations (on the

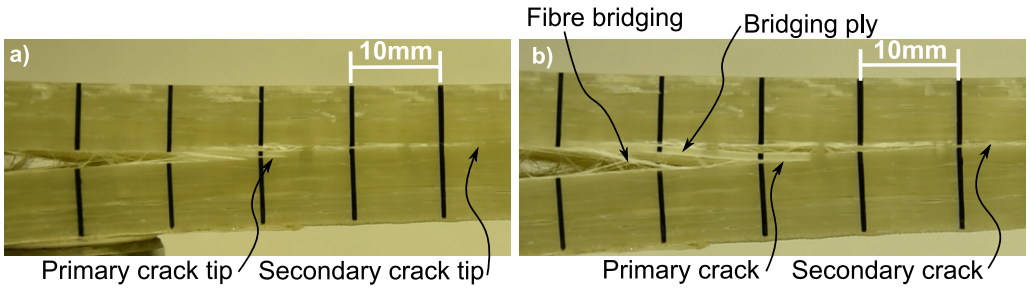

Figure 4.8: a) Zoomed in view of sub-image b in fig. 4.7, **b)** Zoomed in view of sub-image c in fig. 4.7.

plasma treated interface) in some cases, however the occurrence of multiple delaminations was not consistent. The untreated specimens showed a single delamination only, except for two specimens which developed a secondary delamination. In fig. 4.9, the calculated fracture resistance as a function of the measured end-opening is shown. In each plot, the results for plasma treatment are shown along with the results for the untreated reference material. A side-by-side comparison is shown of the low treatment specimens and high treatment specimens. Two untreated specimens (ID: HBB4-04 and HBB4-07) developed two delaminations and large scale fibre bridging, they are indicated in fig. 4.9a.

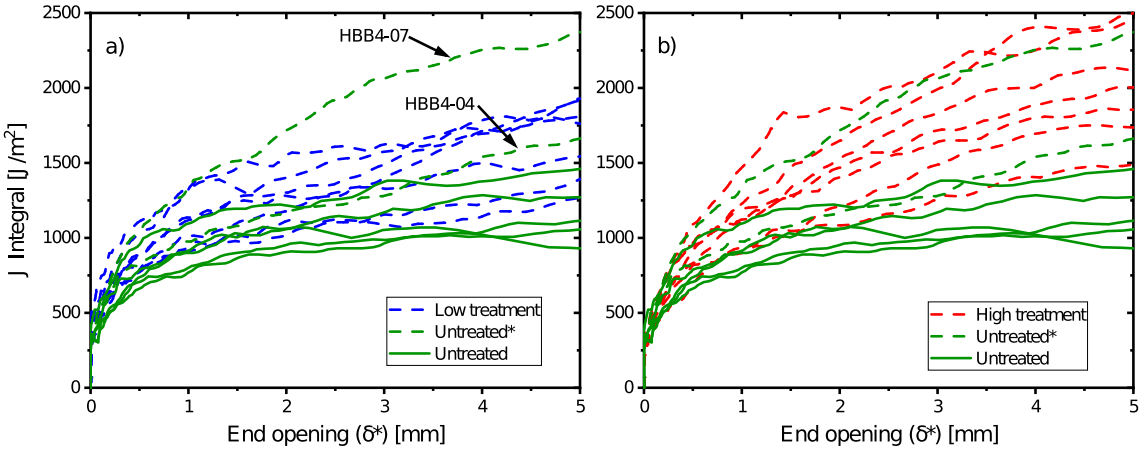

Figure 4.9: Fracture resistance of untreated laminates vs laminates with low treatment **a)** and high treatment **b)**. The dashed lines labelled with HBB4-04 and HBB4-07 are untreated DCB specimens that developed two cracks with large scale fibre bridging.

In fig. 4.9b the J vs end-opening of the high treatment series is presented. The J values for the high treatment condition is higher than for the untreated specimens. The untreated specimens can be observed to reach a steady state J value at approx. 2 mm end-opening, however the specimens with high treatment continue to increase and do not reach a steady state within 5 mm end-opening. The mean J values at 5 mm

end-opening are presented in table 4.2.

Table 4.2: DCB test round 1. Mean J values at 5 mm opening. The outliers for the untreated condition (HBB4-04 and HBB4-07) have been omitted from the calculation.

Treatment condition	Mean J at 5mm end opening [J/m^2]	SD	Percent increase wrt. untreated Round 1
Untreated	1160	190	0
Low treatment	1900	290	63
High treatment	2190	350	88

A zoomed in section of fig. 4.9b is presented in fig. 4.10. The onset of cracking is associated with a significant positive opening at a constant J value; thus the identification of J_0, the value of J at the initiation of crack growth, is fairly clear. As is visible from the graph, the initiation J values (J_0) for the high treatment specimens are similar to the J_0 values of the untreated specimens. Most specimens show zero or even negative end-opening prior to delamination onset.

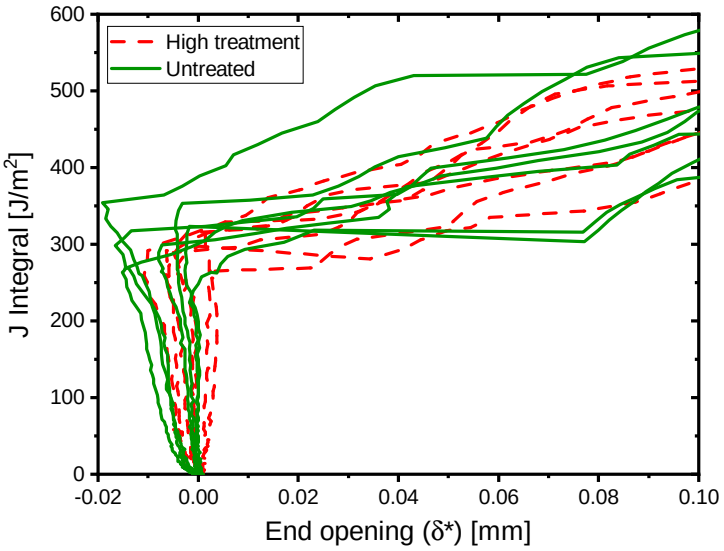

Figure 4.10: Detailed view of J-integral values during initial crack opening.

A detailed comparison is made between two representative specimens; one untreated (HBB4-03) and one with high treatment (HBB1-01). For reference, their J vs end-opening data are presented in fig. 4.11. The time increment between each marker in the graph is constant meaning that a jump between two markers indicates a sudden increase in the end-opening. The untreated specimen clearly achieves a steady state

J value, approx. 1000 J/m^2, whereas the J value for the high treatment specimen increases to approx 2450 J/m^2 before reaching a plateau.

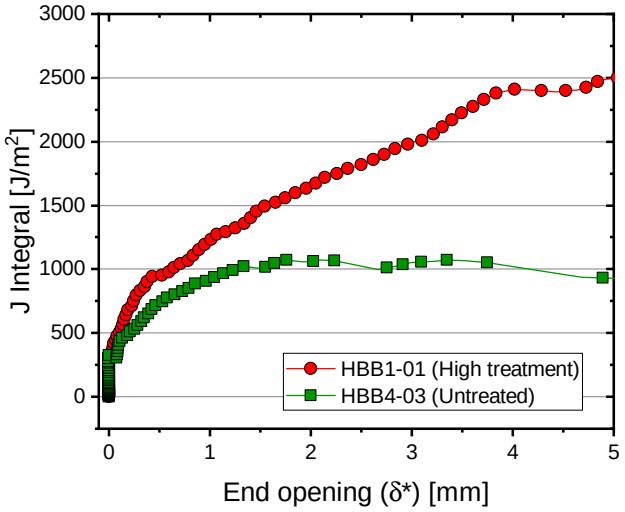

Figure 4.11: Comparison of J integral vs end-opening of the two specimens for in-depth analysis.

In figs. 4.12 and 4.13, the J integral and AE counts are shown as a function of *primary* crack length, a, for the high treatment and untreated specimen. In fig. 4.12, the primary crack is arrested (at approx. a =35 mm) while J increases. This inflection point coincides with the formation of the secondary crack. Simultaneously, the AE activity increases significantly. Figure 4.13 shows the equivalent data for the untreated specimen (plotted using the same axes scales as in fig. 4.12). The crack does not arrest and the J value reaches the steady state of around 1000 J/m^2 with a low amount of AE activity.

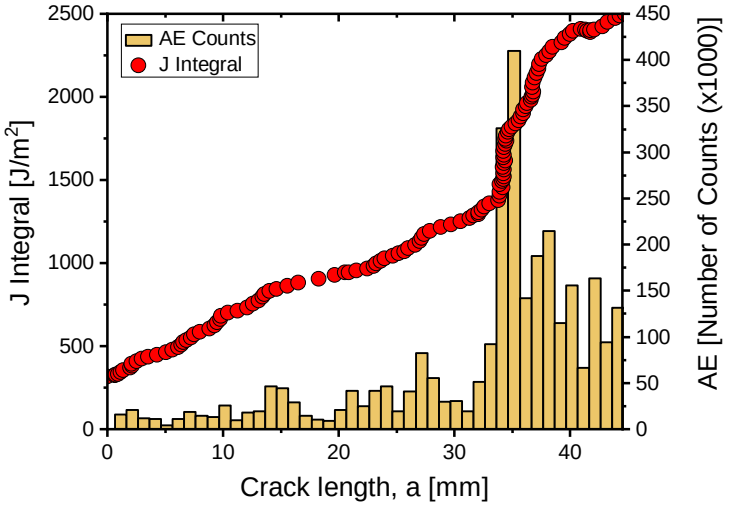

Figure 4.12: Fracture resistance and acoustic emission counts as a function of crack length. Specimen with controlled parallel cracks (high treatment, ID: HBB1-01).

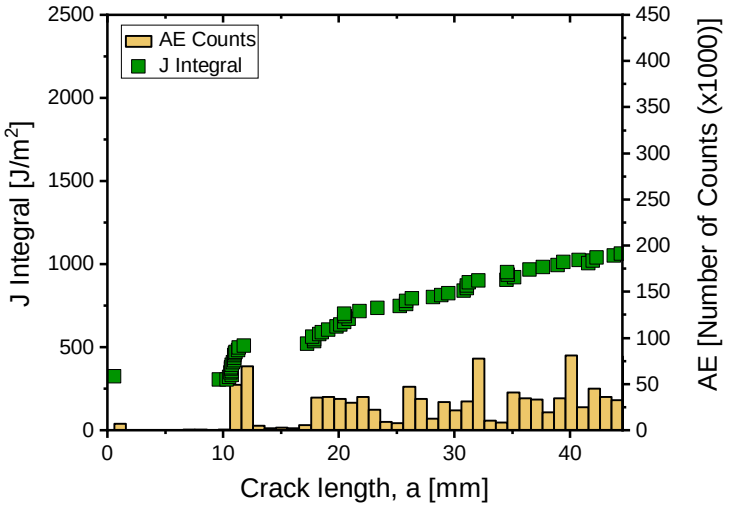

Figure 4.13: Fracture resistance and acoustic emission counts as a function of crack length. Untreated specimen (ID: HBB4-03) with single delamination crack.

ESEM images are shown in figs. 4.14 and 4.15 for specimen HBB1-01 with high treatment. Two cracks are visible following the interface around the bridging ply (ply #10 see fig. 4.3). Both cracks extended across the full width of the specimen, effectively causing a 'two-damage zone' situation. In some locations, large amounts of intralam-

inar cracks were observed within the bridging ply, as shown in fig. 4.15. Micrographs of an untreated specimen (ID: HBB4-01) are shown in figs. 4.16 and 4.17. In fig. 4.16, a single delamination crack is visible. This image is taken from the centre (in x_3 direction, see fig. 4.3) of the specimen. Figure 4.17 shows that near the edge of the same untreated specimen, multiple cracks and intralaminar cracks occur. This was a typical occurence for the untreated specimens.

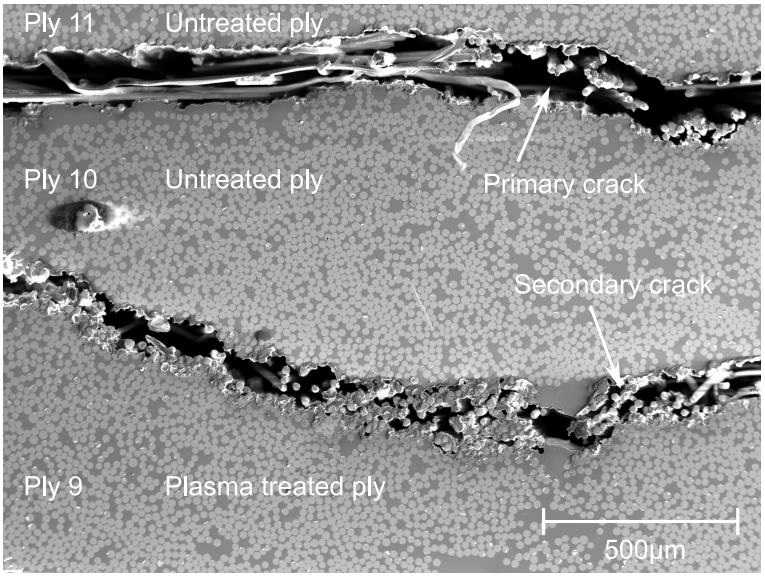

Figure 4.14: Micrograph of DCB cross section showing multiple cracks. (high treatment, ID: HBB1-01).

4.3.2 Second test series: re-loading of fully developed fibre bridging zones

The test specimens had been tested to complete steady state, to fully develop the fibre bridging zone and were then fully unloaded. The DCB specimens were re-tested, after moving the loading grip mounts further down the specimen and positioning the extensometer near the new crack tip.

In the case of the low treatment specimens, multiple delaminations were less common, often individual bundles would bridge rather than the full width ply. Similar behaviour was observed for the untreated specimens, with some showing multiple fracture process zones and some showing bridging bundles. The bridging bundles were typically located close to the edge of the specimen (as seen in fig. 4.17). In all high treatment specimens where secondary delaminations developed, both delamination cracks propagated into the untreated section of the DCB ($a > a_p$, see figs. 4.3

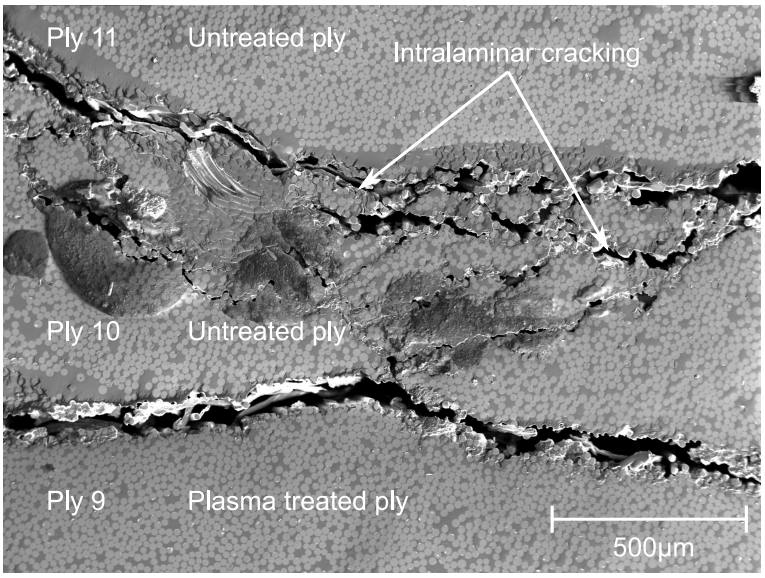

Figure 4.15: Micrograph of DCB cross section showing multiple cracks and intralaminar cracks. (high treatment, ID: HBB1-01).

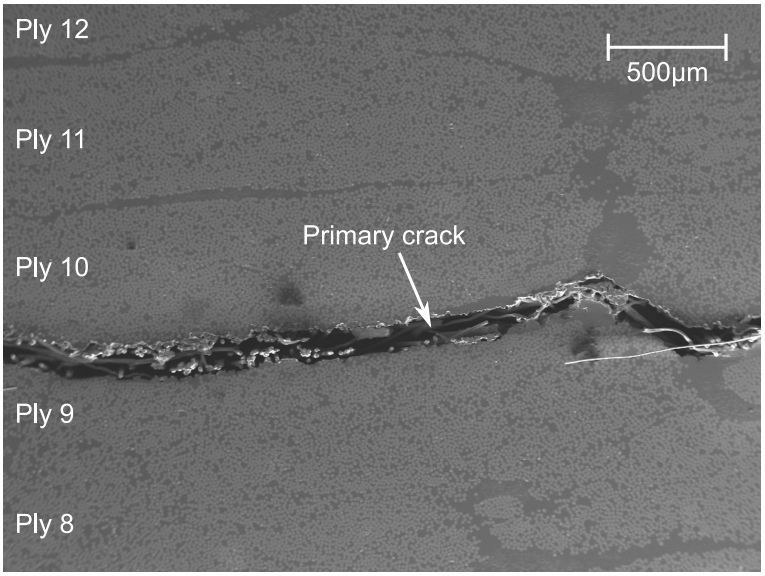

Figure 4.16: Micrograph of DCB cross section showing a single crack. (Untreated specimen, ID: HBB4-01).

and 4.5). In some cases it was observed that the two delaminations appeared to merge, creating a massive fibre bridging network.

In fig. 4.18 the J vs end-opening data is presented for the low treatment and untreated specimens. Both specimen series show an immediate steady state behaviour, i.e. there is no rising J as a function of end-opening. The J vs end opening curves

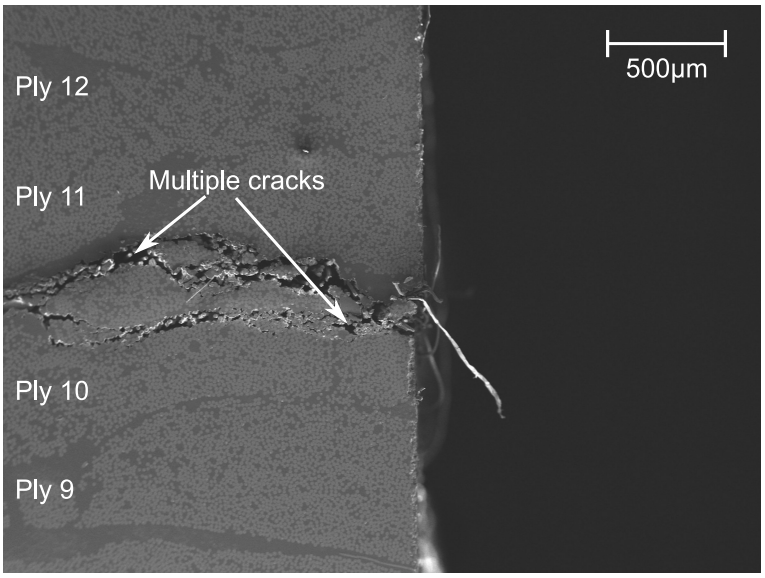

Figure 4.17: Micrograph of DCB cross section showing multiple cracks and intralaminar cracks near the specimen edge. (Untreated specimen, ID: HBB4-01).

for the high treatment and untreated series are shown in fig. 4.19. Again, immediate steady state behaviour is observed. The mean J value at 5 mm end-opening is presented in table 4.3.

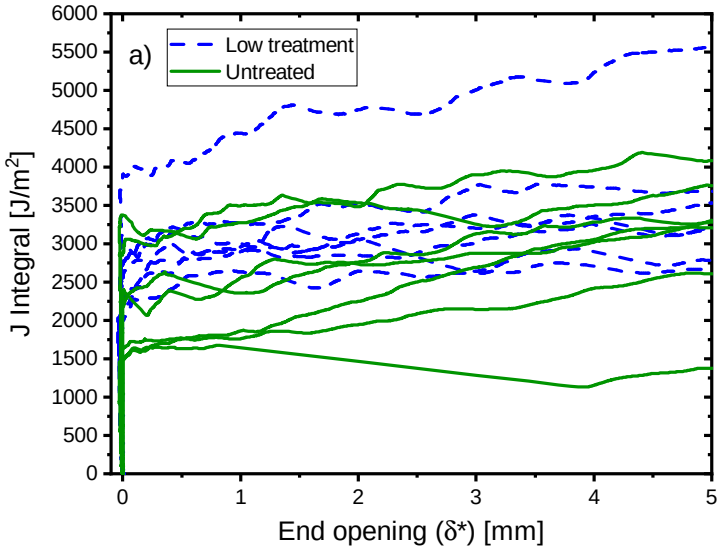

Figure 4.18: J vs end-opening curves for untreated and low treatment specimens during the re-loading experiments.

Three specimens are indicated with arrows in fig. 4.19: HBB1-03 (high treatment),

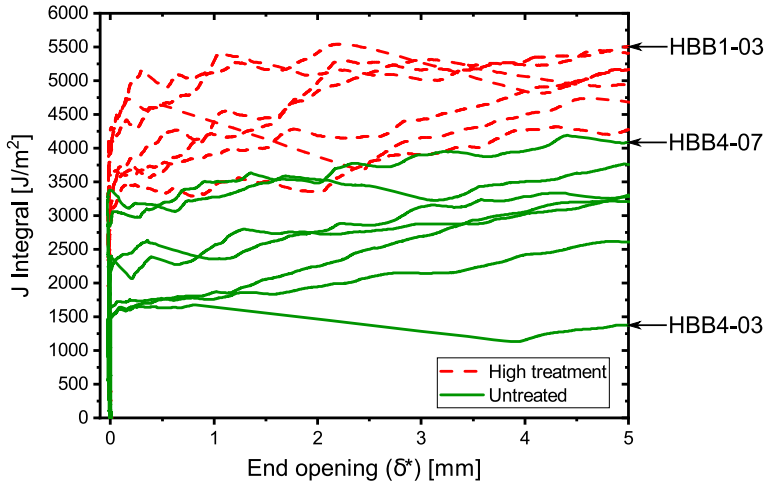

Figure 4.19: J vs end-opening curves for untreated and high treatment specimens during the re-loading experiments.

Table 4.3: DCB test round 2. Mean J values at 5mm opening. The percentage difference in J value is presented with respect to the untreated specimens in Round 2 and in Round 1.

Treatment condition	Mean J at 5mm end opening $[J/m^2]$	SD	Percent increase wrt. untreated Round 2	Percent increase wrt. untreated Round 1
Untreated	3090	890	0	166
Low treatment	3510	980	14	203
High treatment	5020	430	62	333

HBB4-07 (untreated) and HBB4-03 (untreated). Test images of these three specimens are presented in figs. 4.20 and 4.21. Specimen HBB4-07 (untreated) had a large amount of fibre bridging and some bridging bundles and showed the highest steady state J of around 4080 J/m^2. Specimen HBB4-03 (untreated), however only had a single bridging bundle near the specimen edge and the lowest measured J at 5 mm opening of 1375 J/m^2. Finally, specimen HBB1-03 (high treatment) showed massive fibre bridging and full width ply bridging with a J of 5500 J/m^2 at 5 mm end-opening. All of the untreated specimens developed at least one bridging bundle, therefore the data presented for untreated specimens in table 4.3 and figs. 4.18 and 4.19 no longer represent a 'clean' single delamination.

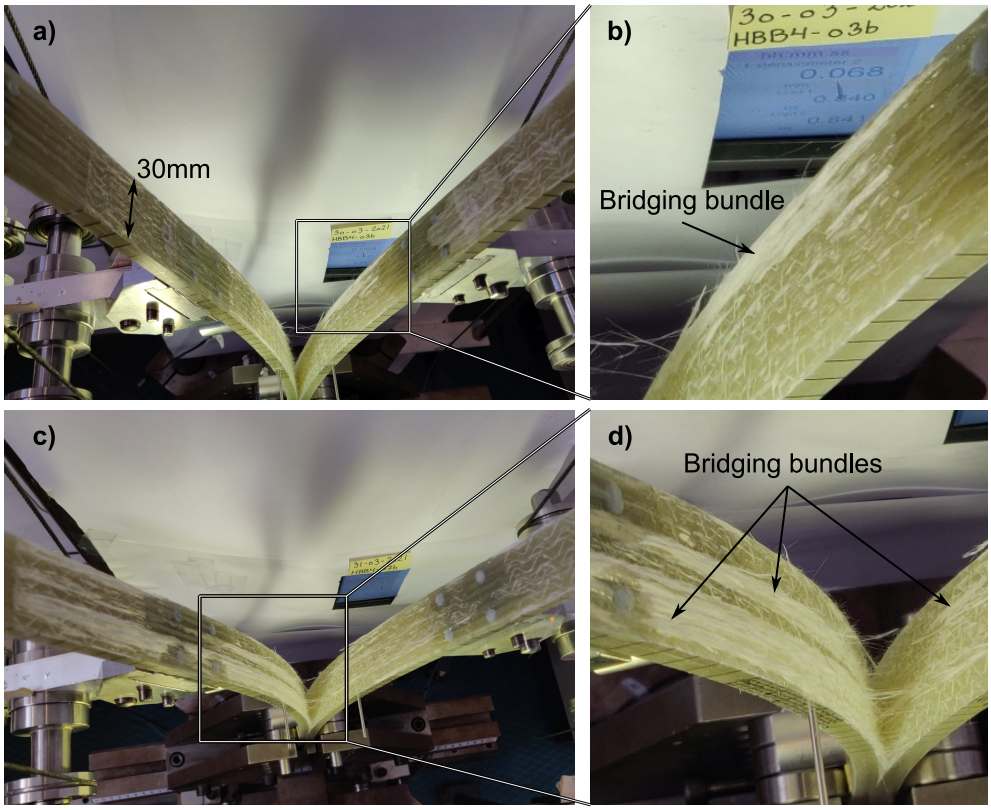

Figure 4.20: Top down view of two untreated DCB specimens (test round 2). **a)** Specimen HBB4-03 showing a single bundle bridging near the specimen edge. **b)** Detailed view of area shown in sub-figure (a). **c)** Specimen HBB4-07 showing multiple bundles bridging and fibre bridging. **d)** Detailed view of area shown in sub-figure (c). For scale reference, specimen width is 30 mm (indicated in sub-figure **a**), due to the skewed perspective of the image, scale is not constant.

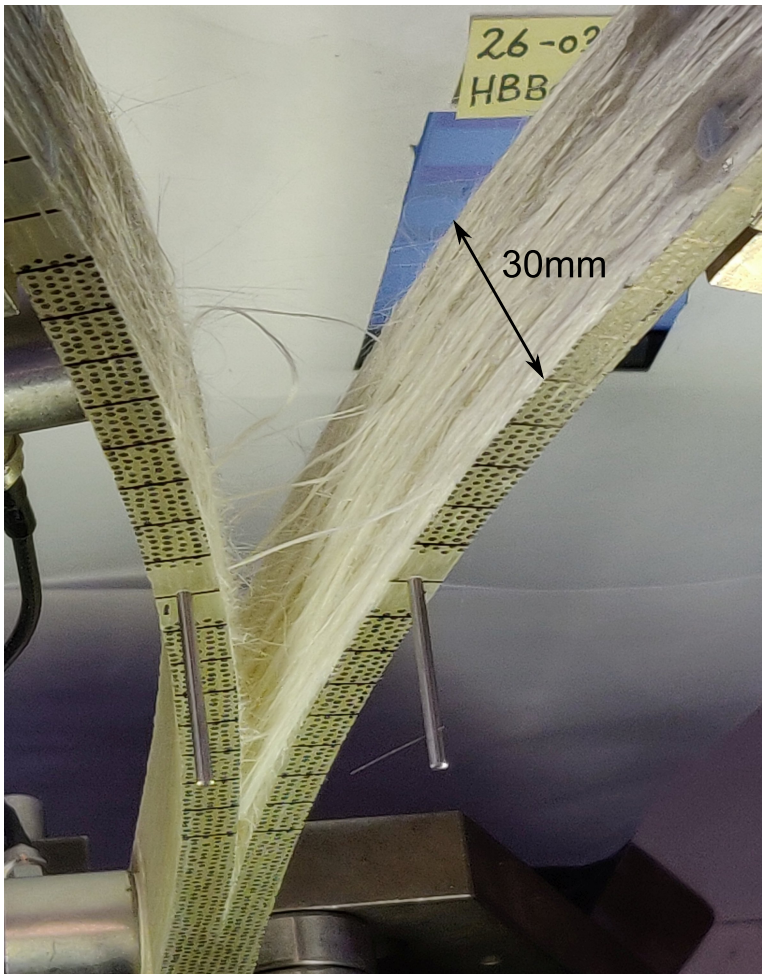

Figure 4.21: Top down view of two untreated DCB specimens (test round 2). Specimen HBB1-03 showing full width ply bridging (white area) and fibre bridging.

Chapter 5

Discussion

5.1 Plasma treatment

Atmospheric pressure plasma treatment was employed to introduce fluorine or fluorine containing polymers onto glass fibre fabrics. Both treatment methods (small and large DBD device) resulted in an increase in fluorine, detectable by XPS, and a decrease in wetting rate (see section 3.4). Fluorine based plasma treatments are often used for etching purposes [95], however SEM images of the fibre surfaces treated with the small DBD (in He/CF_4) did not show visible etching (figure 4 in paper **[P1]**). This may be due to a short exposure time. In the present work, etching was not a treatment objective since it may increase roughness and create a stronger fibre/matrix interphase [96]. Vinogradov et al. [67] have shown (using FTIR and, UV absorption spectroscopy and emission spectroscopy) that the ratio between in CF_2 and CF_3 in DBD plasmas (in CF_x containing gasses) plays an important role in determining whether etching or fluorination is pronounced. Future work could include optical plasma diagnostics to determine the ratio of CF_2 and CF_3 in the large and small plasma devices used in the present work.

In the work by Agopian et al. [97, 98], where sized carbon fibres were fluorinated in an N_2/F_2 environment (although not by plasma), it was noted that the sizing became fully etched if treated more than 30 minutes. Water contact angles increased from ca. 40° for untreated fibres to 105° after 20 minute treatment. However, after a 30 minute treatment, when the sizing of the fibres was fully etched, the water contact angle was reported to be 0° (i.e. full wetting). Therefore, the dynamic micro wetting technique may be used in future work, if etching occurs, to determine the point where a fibre becomes fully etched because wetting rates may increase again.

For treatment with the small DBD device in He/CF_4, the detection of fluorine on both the bundle interior and exterior (fig. 3.2) indicates that the treatment penetrated throughout the bundle and did not just affect the fibres on the surface of the bundle. The exposure time to the plasma was longer for treatment with the small DBD than treatment with the large DBD device, so there might be a difference in treatment effect on the fibres within the bundle for the two different plasma devices. This may then have an affect on the development of intralaminar damage in plasma fluorinated plies. If fluorine or fluorocarbon is introduced within the bundle interior, there may be a

weaker fibre/matrix interphase leading to a higher development of intralaminar cracks and fibre bridging in delamination experiments. This inverse relation between fibre/-matrix interphase strength and fibre bridging was demonstrated by Feih et al. [71].

The mean fluorine content detected on the fibre surface was highest for the treatment with He/OFB using the large DBD device (section 3.4.2). This treatment also had the lowest wetting rate of all the treatments. A higher detected fluorine content therefore indicates a slower wetting rate, however there is likely a treatment amount (exposure time) where, if no etching is present, the fibre surface is saturated with fluorocarbon. In the treatment with CF_4, little deposition or polymerization occurs, however the treatment with OFB could increase the layer thickness of the fluorocarbon coating. Once the glass surface is saturated further plasma fluorination would in either case not affect the observed wetting properties. However, in the interphase formation (dispersion of the sizing layer into the surrounding resin), a larger fluorocarbon content could affect the strength of interphase regions in the final fibre composite and thereby the inter and intralaminar properties.

An uneven distribution of fluorine was detected in the specimens treated with the large DBD device. This was observed both for the treatment of polyethylene terephthalate (PET) films in paper **[P2]** and in fabric samples in paper **[P3]**. Possible causes include uneven distribution of the He/OFB gas mixture in the PMMA plasma chamber and uneven spacing between the electrodes. Observation by infrared camera did show that the gas mixture was escaping along all borders of the chamber. Furthermore, ambient air may have leaked non-uniformly into the plasma chamber. It has been shown that the presence of oxygen can greatly reduce fluorocarbon deposition rates in atmospheric DBD treatment [68]. The packing density of the fibres in the bundle may also influence the treatment process for the interior fibres (see fig. 3.2) as there may be varying emission of volatile components from the sizing. In order to control the treatment process and to obtain a more uniform treatment, further investigation is required.

An issue regarding the plasma treatment process is the choice of weakening a lamina interface by fluorination. The idea of weakening a material locally may be difficult to 'sell' to for example an manufacturer of fibre composites. One could argue that instead of weakening the secondary delamination plane, perhaps it may be better to the strengthen the primary delamination plane. Preliminary work in this PhD project investigated gliding arc plasma [35, 62, 99] treatment as a method for increasing the wetting rate (i.e. decreasing static contact angle), however the change in wetting rate was not as significant as those by plasma fluorination. The focus of the present work was on creating a secondary delamination and that was deemed most likely to be successful by locally fluorinating the glass fibre fabrics. Initiating multiple delaminations by local strengthening is an interesting topic for future research, as having the capability to both weaken and strengthen gives better capabilities to tailor a structure's

delaminations, and by extension it's fracture resistance.

5.2 Control of interlaminar peak stress

The controlled reduction of peak stress was demonstrated by the short beam shear and curved beam tests section 3.4.2. Somewhat surprising, however, was the relatively small reduction in both normal ($\hat{\sigma}_n$) and shear ($\hat{\sigma}_t$) peak stress reduction, compared with the large reduction in wetting rate (section 3.4.2). In the literature there is a general agreement that the wettability of fibres may have an effect on the fibre/matrix adhesion and porosity content in a fibre matrix composite [73]. The present work indicates that for vacuum infused fabrics, the fibre wettability alone may not be the primary factor for controlling the interlaminar peak stress. Furthermore, the SEM images of both the curved beam specimens and the DCB specimens showed that a full fibre/matrix contact (i.e. no voids or gaps in the fibre/matrix interphase) was achieved, even for the highly treated specimens (section 4.3.1, and figures 6 and 7 in paper **[P3]**). This is further corroborated by the low porosity content (0.7-0.8%) observed in curved beams with and without a fluorinated ply, indicating that wetting alone is not a good indicator of void formation in the vacuum infusion process.

The low treatment condition showed an introduction of fluorocarbon and a decreased wetting rate, however the decrease in $\hat{\sigma}_n$ and $\hat{\sigma}_t$ was not found to be statistically significant (section 3.4.2). This may partially be due to the fact that the curved beam test is sensitive to defects and thus causes large scatter in the data [52]. Makeev et al. [52, 100], showed that this may be overcome by X-ray tomography assisted finite element modelling of specimens with defects, however this is neither a simple nor accessible method to achieve an accurate σ_n. Furthermore, the formation of multiple cracks in both the short beam shear and curved beam specimens means that a true $\hat{\sigma}$ is not measured if the cracks form simultaneously. High speed video recording in combination with digital image correlation (DIC) may assist in determining at what stress level the first crack is formed, or if cracks form simultaneously.

An interesting finding was the consistent failure location in the curved beam specimens for specimens with a plasma treated ply (section 3.4.2). Delamination cracks were always observed on the interface between the plasma treated ply and an untreated ply. On the other hand, the specimens containing only untreated plies showed failure on any interface throughout the specimen thickness. Even though the decrease in peak normal stress was modest for the curved beams, the delamination location was consistent and can therefore be considered controlled.

5.3 Enhanced fracture resistance by multiple delaminations

A novel method for controlling the formation of parallel delaminations to enhance fracture resistance has been presented. The consistent development of two parallel delaminations after treating a glass fibre fabric with plasma in a fluorocarbon containing gas mixture demonstrated the repeatability of the process.

In this chapter section, numerous comparisons are made with the work by Herráez, Pichler and Botsis (Sep 2020) [101], the following is a brief introduction and materials comparison. In their study, they investigated multiple parallel delaminations initiated by 1 or 3 PTFE slipfoils within an otherwise pristine laminate. The use of PTFE slipfoils means that essentially they have reduced the peak strength of the secondary interface to zero, and that a secondary delamination already exists a priori. Their focus was on the propagation of the parallel delamination. Numerical modelling and experimental investigation showed a number of similar results to the present work, most importantly a significant increase in fracture resistance in DCB specimens. Different configurations of the artificial defect(s) and different applied mode mixities were investigated. The material system used was a carbon/epoxy UD prepreg with ply thickness of 0.2 mm which was cured with an applied pressure of 3 bar in an autoclave. In comparison, the vinyl ester/UD glass fibre fabric in the present work had a ply thickness of 1 mm and was made by vacuum infusion followed by a postcure. The differences in resultant fibre composite materials include ply architecture (UD fabric vs UD prepreg), fibre volume fraction (autoclave at 3 bar will likely have a higher volume fraction than vacuum infusion at 850 mbar) (fibre volume fraction was not reported however in their article), resin system (epoxy vs vinyl ester) and fibre type (carbon vs glass).

In the present work an increase in apparent mode I fracture resistance of 88% was found for the high treated specimens with respect to the untreated specimens (DCB test round 1). In the second test round, when the fibre bridging zone was already fully developed, the difference between the untreated and high treatment specimens was slightly lower (62%), although it is critical to note that all untreated specimens developed bridging bundles and therefore the J value is no longer associated with the propagation of a single delamination.

The first DCB test round for the untreated specimens (see table 4.2), a J value of 1160 J/m^2 was reported at an end opening of 5 mm. In table 4.3 the J at 5 mm0 end opening was presented for specimens with full FBZ development (test round 2). Specimens with high treatment showed a J value of 5020 J/m^2 in round 2, or an increase of 333% with respect to the round 1 untreated specimens. The high treatment specimens in round 2 also showed massive fibre bridging networks due to the two parallel delaminations merging. The question, however, is if the comparison between the two cases

is fair? The untreated DCB specimens in round 1 may not have reached a steady state fracture process zone, as indicated by the eventual development of bridging bundles in the re-loading experiment in round 2. It would therefore be more accurate to call the J value of 1160 J/m^2, the J for a 'clean' single delamination and not a steady state J value for this material system. Furthermore, the J value of 5020 J/m^2 is not the J value for two 'clean' parallel delaminations, instead it is the J value for two delaminations which have merged to create a massive fibre bridging network.

In the work by Herráez et al. [101], an increase in fracture resistance of approximately 300% was reported for mode I specimens with two delaminations. Similar to the present work, the fracture resistance when the secondary delamination had just formed was approximately the double of the single delamination value. Maximum fracture resistance (+300%) was not reached until the primary crack had grown approx. 90 mm. This crack length is of comparable magnitude to the crack length (approx. 150 mm) required to reach full steady state in the present work. The differences in materials described earlier, especially the bridging ply thickness (i.e. bending stiffness), likely influence the delamination growth required to fully develop both fracture process zones. A higher bending stiffness requires larger crack growth to achieve the same normal opening of the fracture process zone. Goutianos and Sørensen [39], reported that a thinner bridging ligament (i.e. ply thickness), resulted in larger normal opening of the secondary delamination. If the ligament was too thick (and thus had a higher bending stiffness) the secondary delamination would not fully develop.

In the present work (chapter 4), plasma treatment was only applied to approximately half the fabric length (see figs. 4.3 and 4.4). After the formation of the secondary delamination during DCB testing, both delaminations continued propagating beyond the treated area. This raises the question: how small can the treated area be made while still enabling the initiation and continued propagation of both cracks into pristine material? The numerical analysis by Herráez et al. [101] showed that for thin plies (thickness, t<0.2 mm), a minimum defect length of 4 times the ply thickness was required for a secondary delamination to propagate. For thicker plies, this value was reported to increase (at a ply thickness t=0.4 mm, a defect length of 6t was required). This is comparable to the conclusion drawn by Goutianos and Sørensen [39] that a thinner ply allows for more bending and undergo larger normal opening, and can develop parallel delaminations at lower stresses.

The study on bondlines by Rask and Sørensen [36], where parallel delaminations occurred next to the bondline, inspired the present work. The occurrence of multiple delaminations was likely due to weaker interlaminar interfaces in the laminate next to the bondline with the primary crack. The formation of parallel cracks in bonded joints has been shown by Li et al. [102] to be dependent on the variability of interfacial properties. In fibre composite materials, just as in bondlines, the interfacial properties

are not constant but vary as a function of position. Li et al. showed that this variation contributed to both fibre bridging formation and ligament bridging in bonded joints. This can also be an explanation for the occurrence of multiple delaminations seen in the untreated specimens in the present work. If the primary delamination is allowed to propagate over a longer distance, its chances of encountering a weak area in a neighbouring ply is increased. The variation in number of parallel delaminations observed by Rask and Sørensen [36] is thus likely due to the interlaminar properties within the laminate next to the bondline. Indeed the layup of the specimens with 3 parallel cracks had more off axis plies next to the bondline than the specimens developing only 2 parallel cracks [36]. Lindgaard and Bak [103] reported more crack 'migration' (visually similar to parallel delaminations), for layups with off axis plies next to the primary crack.

5.4 J-integral and cohesive laws from specimens with multiple cracks

Unfortunately, the occurrence of multiple cracks in experiments is not always clearly reported in the literature. Therefore care must be taken when using experimental data found in the literature as input for cohesive zone models.

Cohesive zone modelling is normally done assuming a single delamination plane. However, if a laminate model is created with cohesive zones between each lamina, the fracture resistance of the whole laminate may be severely overpredicted if cohesive laws from experiments with multiple delaminations are used. The use of fracture resistance data (from experiments developing multiple delaminations) in simulation with one cohesive zone is only valid if the structure develops the same delaminations as the DCB used for model input. For example in the study by Holmes et al. [104], fatigue tests were performed and in some cases multiple cracks appeared. Cyclic bridging laws were calculated based on the experimental data, however these laws may not be valid when used to model a single delamination crack and care must be taken in applying these laws in structures (with other fibre architecture, layups, design) where secondary delaminations may not appear.

A large scale bridging law may be defined as the sum of two separate cohesive laws: one representing fracture at the crack tip and one for the fibre bridging zone (FBZ) behind the crack tip. In the fibre bridging portion of the cohesive law, however, there are actually two (or more) contributing factors which are smeared into one effective law. A bridging fibre contributes to the fibre bridging law by applying a closing traction to the crack face, additionally there is a contribution from the peeling process of the fibre. Often, this peeling process is not considered as a separate J contribution and

instead it is lumped together with the traction based contribution to J. Other contribution sources such as intraply cracking are also lumped into the same J contribution.

If we, as a thought experiment, look at one bridging fibre and scale it up so that the fibre now has the thickness of a ply. The problem becomes identical to having two parallel delaminations. Do we now consider the J contribution of the secondary delamination separately or can we still lump it together with the J_{FBZ} of the fibre bridging law? The crack tip that is furthest ahead could then be considered as the primary crack tip and everything that is behind that crack tip as the fibre bridging zone (including the bridging ply). The physical meaning of the J-integral can then be interpreted as the overall resistance to fracture. It can also still be used in modelling, as long as the user is aware that the properties of the cohesive law are smeared properties of multiple delaminations, relevant only for use in cases where that same scenario occurs.

Goutianos and Sørensen [39] discussed the negative contribution to the total J-integral of the portion of the secondary delamination that grows in the negative x_1 direction (i.e. opposite direction of the primary delamination). From a mathematical standpoint this has merit since the crack growth direction is opposite to the conventional crack growth direction, however from a physical perspective this idea must be reconsidered. When the left hand crack grows, it is forming new surface area and in the process breaking chemical bonds. Bonds are broken within the matrix, when fibres break and when fibres peel from the matrix (e.g. during fibre bridging). The breaking of chemical bonds necessitates energy, they do not break spontaneously. Therefore from a perspective of conservation of energy, the growth of any crack, in any direction, must contribute positively to the energy consumed. The J-integral is a method to determine the work per unit fracture area, therefore the following change to the formulation by Goutianos and Sørensen [39] is proposed:

$$J_{ss} = \sum |J_i|, \tag{5.1}$$

where J_{ss} is the total fracture resistance of a plate with multiple delaminations and J_i are the individual contributions for each delamination that grows.

In the present work, evidence was found of growth in the negative x_1 direction, however this was never associated with a decrease in J. More detailed analysis of this phenomenon is suggested in future work.

5.5 Limitations of the present study

In real life, structures are unlikely to be loaded in pure mode I conditions. Therefore a mixed mode testing campaign would be necessary to determine the initiation and propagation of parallel delaminations under more realistic loading conditions. The study by Herráez et al. [101] did show that propagation of multiple delaminations is possible under mixed mode conditions, however they did not consider initiation of the secondary delamination.

Turbine blades and bridge structures are not subject to just static loading. They are subject variable amplitude cyclic loads, such as wind gusts, passing vehicles, and in the case of turbines, the variable gravitational force caused by the rotation of the blades. Studies by Holmes et al. [104] (glass fabric/polyester) and Khudiakova et al. [105] (carbon fibre/polyphenylene sulfide) showed that under cyclic loading, secondary cracks appear in parallel to the primary crack, however the formation of secondary delaminations was not consistent (i.e. controlled) in either study.

Multiple cracks decrease the bending stiffness of a laminate, which decreases the buckling load in compression [106, 107]. This may have consequences for structural stability for buckling sensitive structures such as wind turbine blades and should be investigated further. The overall laminate thickness must also be considered since two delaminations in a thin laminate have a more significant effect on buckling load than two delaminations in a thick laminate [107].

5.6 Application of multiple delaminations

The demonstrated plasma treatment methods are localised in the sense that a small portion of a fabric can be treated, exactly where a secondary delamination is required. This could allow the tailoring of structures such that delaminations occur in expected locations and in tough interfaces, allowing delamination growth to be slowed or even halted. An interface close to a bondline or plydrop could be considered, such that the formation of multiple delamination and corresponding increase in fracture resistance is controlled. It is of course necessary that the location of the primary delamination is known a priori, this is why sensitive areas in a composite structure such as a plydrop or bondline are excellent candidates for such a treatment.

Another application may be the testing and tuning of non destructive test (NDT) methods [108, 109]. Established techniques such as ultrasonic scanning, thermography, shearography, x-ray tomography etc. may not be able to detect a local weak area (also referred to as a partial bond) created by plasma fluorination. More severe treat-

ments may even be able to consistently create a so called 'kissing bond', which is a bond with full interfacial contact (i.e. no detectable gap between faces) but with zero or near zero strength [109]. This does also raise the question: if the treatment is made for the purpose of developing multiple delaminations, how do you perform quality control of the treatment without destructive inspection?

5.7 Summary of suggested topics for future research

- Expand testing of DCB specimens to include different mode II and mixed mode conditions.
- Perform fatigue delamination studies, documenting crack growth of individual crack tips (initiation and propagation could be treated separately).
- Investigate the affect of ply bridging and multiple delaminations with large scale fibre bridging on in-plane laminate properties and structural stability (buckling).
- Investigate methods for strengthening interfaces as a method to control delamination initiation in neighboring interfaces.

Chapter 6

Conclusions

In the present thesis, the topic of multiple parallel delaminations has been investigated experimentally. Based on the results presented in the thesis and attached papers, the following conclusions may be drawn:

- Treatment with atmospheric pressure plasma in fluorine containing gas introduces fluorine or fluorocarbons onto sized glass fibre surfaces.
- Peak interlaminar stresses are reduced for fibre composites containing a plasma fluorinated ply.
- The development of two parallel delaminations is consistent with reducing the peak interlaminar stress of a secondary crack plane.
- The fracture resistance of two propagating parallel delaminations is significantly higher than the fracture resistance of a single delamination.

Bibliography

[1] IEA, "World Energy Outlook 2021," tech. rep., Paris, 2021.

[2] H. Rosling, A. R. Rönnlund, and O. Rosling, *Factfulness: Ten Reasons We're Wrong About the World - and Why Things Are Better Than You Think*. Flatiron Books, 2018.

[3] Masson-Delmotte_et_al., *IPCC, 2021: Contribution of Working Group I to the Sixth Assessment Report of the Intergovernmental Panel on Climate Change*. Cambridge University Press, 2021.

[4] A. K. Magnan, H. O. Pörtner, V. K. Duvat, M. Garschagen, V. A. Guinder, Z. Zommers, O. Hoegh-Guldberg, and J. P. Gattuso, "Estimating the global risk of anthropogenic climate change," *Nature Climate Change*, vol. 11, no. 10, pp. 879–885, 2021.

[5] IEA, "World Energy Outlook 2019," tech. rep., 2019.

[6] "Press Release Feb 10 2021.," *Vestas Wind Systems A/S URL: www.vestas.com/en/media/company-news?l=22&n=3886820#!NewsView*.

[7] B. F. Sørensen and L. P. Mikkelsen, "New advanced materials will enable the bigger wind turbines of the future," in *DTU International Energy Report 2021: Perspectives on Wind Energy* (B. Holst Jørgensen, P. Hauge Madsen, G. Giebel, I. Martí, and K. Thomsen, eds.), pp. 125–133, Risø, Roskilde, Denmark: DTU Wind Energy, 2021.

[8] Y. Swolfs, B. Fazlali, A. Melnikov, F. Mesquita, V. Feyen, C. Breite, L. Gorbatikh, and S. V. Lomov, "State-of-the-art models for mechanical performance of carbon-glass hybrid composites in wind turbine blades," *IOP Conference Series: Materials Science and Engineering*, vol. 942, no. 1, 2020.

[9] A. Kandelbauer, G. Tondi, O. C. Zaske, and S. H. Goodman, "Unsaturated Polyesters and Vinyl Esters," in *Handbook of Thermoset Plastics* (H. Dodiuk and S. H. Goodman, eds.), ch. 6, pp. 111–172, Elsevier Inc., third ed., 2014.

[10] M. Ghazimoradi, E. A. Trejo, V. Carvelli, C. Butcher, and J. Montesano, "Deformation characteristics and formability of a tricot-stitched carbon fiber unidirectional non-crimp fabric," *Composites Part A: Applied Science and Manufacturing*, vol. 145, no. March, p. 106366, 2021.

[11] U. A. Mortensen, *Process parameters and fatigue properties of high modulus composites*. PhD thesis, Technical University of Denmark, 2019.

[12] C. H. Park and W. Lee, "Modeling void formation and unsaturated flow in liquid composite molding processes: A survey and review," *Journal of Reinforced Plastics and Composites*, vol. 30, no. 11, pp. 957–977, 2011.

[13] J. L. Thomason, "Glass fibre sizing: A review," *Composites Part A: Applied Science and Manufacturing*, vol. 127, p. 105619, 12 2019.

[14] D. A. Jesson and J. F. Watts, "The interface and interphase in polymer matrix composites: Effect on mechanical properties and methods for identification," *Polymer Reviews*, vol. 52, no. 3-4, pp. 321–354, 2012.

[15] M. Dey, J. M. Deitzel, J. W. Gillespie, and S. Schweiger, "Influence of sizing formulations on glass/epoxy interphase properties," *Composites Part A: Applied Science and Manufacturing*, vol. 63, pp. 59–67, 2014.

[16] J. L. Thomason and D. W. Dwight, "Use of XPS for characterization of glass fibre coatings," *Composites Part A: Applied Science and Manufacturing*, vol. 30, no. 12, pp. 1401–1413, 1999.

[17] F. R. Jones, "A review of interphase formation and design in fibre-reinforced composites," *Journal of Adhesion Science and Technology*, vol. 24, no. 1, pp. 171–202, 2010.

[18] J. K. Kim, M. L. Sham, and J. Wu, "Nanoscale characterisation of interphase in silane treated glass fibre composites," *Composites Part A: Applied Science and Manufacturing*, vol. 32, no. 5, pp. 607–618, 2001.

[19] L. H. Sharpe, "The Interphase in Adhesion," *The Journal of Adhesion*, vol. 4, no. 1, pp. 51–64, 1972.

[20] FAA, "Advisory Circular 25 571-1D Damage Tolerance and Fatigue Evaluation of Structure," *Advisory Circular 25_571-1D*, vol. 1, pp. 1–2, 2012.

[21] G. Sinnema, "Safety of spaceflight structures - The application of fracture and damage control," *Acta Astronautica*, vol. 162, pp. 469–480, 2019.

[22] R. Alderliesten, "Damage tolerance of bonded aircraft structures," *International Journal of Fatigue*, vol. 31, no. 6, pp. 1024–1030, 2009.

[23] H. G. Lee, M. G. Kang, and J. Park, "Fatigue failure of a composite wind turbine blade at its root end," *Composite Structures*, vol. 133, pp. 878–885, 12 2015.

[24] L. C. T. Overgaard, E. Lund, and O. T. Thomsen, "Structural collapse of a wind turbine blade. Part A: Static test and equivalent single layered models," *Composites Part A: Applied Science and Manufacturing*, vol. 41, pp. 257–270, 2 2010.

[25] Z. Suo, G. Bao, and B. Fan, "Delamination R-Curve Phenomena Due to Damage," *Journal of Mechanics, Physics and Solids*, vol. 40, no. 1, pp. 1–16, 1992.

[26] A. G. Evans, "Perspective on the Development of High-Toughness Ceramics," *Journal of the American Ceramic Society*, vol. 73, no. 2, pp. 187–206, 1990.

[27] E. Wilson, M. S. Mohammadi, and J. A. Nairn, "Crack Propagation Fracture Toughness of Several Wood Species," *Advances in Civil Engineering Materials*, vol. 2, no. 1, pp. 316–327, 2013.

[28] N. Matsumoto and J. A. Nairn, "The fracture toughness of medium density fiberboard (MDF) including the effects of fiber bridging and crack-plane interference," *Engineering Fracture Mechanics*, vol. 76, no. 18, pp. 2748–2757, 2009.

[29] A. Watt, A. A. Goodwin, and A. P. Mouritz, "Thermal degradation of the mode I interlaminar fracture properties of stitched glass fibre/vinyl ester composites," *Journal of Materials Science*, vol. 33, no. 10, pp. 2629–2638, 1998.

[30] A. Mouritz, "Review of z-pinned composite laminates," *Composites Part A: Applied Science and Manufacturing*, vol. 38, pp. 2383–2397, 12 2007.

[31] J. A. Pascoe, S. Pimenta, and S. T. Pinho, "Interlocking thin-ply reinforcement concept for improved fracture toughness and damage tolerance," *Composites Science and Technology*, vol. 181, no. June, p. 107681, 2019.

[32] M. Hojo, S. Matsuda, M. Tanaka, S. Ochiai, and A. Murakami, "Mode I delamination fatigue properties of interlayer-toughened CF/epoxy laminates," *Composites Science and Technology*, vol. 66, no. 5, pp. 665–675, 2006.

[33] G. Bao and Z. Suo, "Remarks on crack bridging concepts," *Applied Mechanics Reviews*, vol. 45, no. 8, pp. 355–366, 1992.

[34] J. R. Rice, "A Path Independent Integral and the Approximate Analysis of Strain Concentration by Notches and Cracks," *Journal of Applied Mechanics*, vol. 35, no. 2, pp. 379–386, 1968.

[35] Y. Kusano, B. F. Sørensen, T. L. Andersen, and F. Leipold, "Adhesion improvement of glass-fibre-reinforced polyester composites by gliding arc discharge treatment," *Journal of Adhesion*, vol. 89, no. 6, pp. 433–459, 2013.

[36] M. Rask and B. F. Sørensen, "Determination of the J integral for laminated double cantilever beam specimens: The curvature approach," *Engineering Fracture Mechanics*, vol. 96, pp. 37–48, 12 2012.

[37] B. F. Sørensen, K. Jørgensen, T. K. Jacobsen, and R. C. Østergaard, "DCB-specimen loaded with uneven bending moments," *International Journal of Fracture*, vol. 141, no. 1-2, pp. 163–176, 2006.

[38] D. J. H. Cederløf, Y. Kusano, and B. F. Sørensen, "Control of interlaminar strength by atmospheric pressure plasma treatment," *Submitted to Journal of Composite Interfaces*, 2022.

[39] S. Goutianos and B. F. Sørensen, "Fracture resistance enhancement of layered structures by multiple cracks," *Engineering Fracture Mechanics*, vol. 151, pp. 92–108, 2016.

[40] J. Beauson and P. Brøndsted, *Chapter 23: Wind Turbine Blades: An End of Life Perspective*. Springer Nature, 2016.

[41] M. Kuhtz, A. Hornig, M. Gude, and H. Jäger, "A method to control delaminations in composites for adjusted energy dissipation characteristics," *Materials and Design*, 2017.

[42] M. Kuhtz, A. Hornig, J. Richter, and M. Gude, "Increasing the structural energy dissipation of laminated fibre composite materials by delamination control," *Materials & Design*, vol. 156, pp. 93–102, 10 2018.

[43] Y. Kusano, "Atmospheric pressure plasma processing for polymer adhesion: A review," *Journal of Adhesion*, vol. 90, no. 9, pp. 755–777, 2014.

[44] P. Dimitrakellis and E. Gogolides, "Hydrophobic and superhydrophobic surfaces fabricated using atmospheric pressure cold plasma technology: A review," *Advances in Colloid and Interface Science*, vol. 254, pp. 1–21, 4 2018.

[45] A. Patnaik, R. S. Rengasamy, V. K. Kothari, and A. Ghosh, "Wetting and wicking in fibrous materials," *Textile Progress*, vol. 38, no. 1, pp. 1–105, 2006.

[46] E. Mäder, "Study of fibre surface treatments for control of interphase properties in composites," *Composites Science and Technology*, vol. 57, pp. 1077–1088, 1 1997.

[47] E. Mäder, K. Grundke, H.-J. Jacobasch, and G. Wachinger, "Surface, interphase and composite property relations in fibre-reinforced polymers," *Composites*, vol. 25, pp. 739–744, 1 1994.

[48] P. S. Shin, Y. M. Baek, J. H. Kim, H. S. Park, D. J. Kwon, J. H. Lee, M. Y. Kim, K. L. DeVries, and J. M. Park, "Interfacial and wetting properties between glass fiber and epoxy resins with different pot lifes," *Colloids and Surfaces A: Physicochemical and Engineering Aspects*, vol. 544, pp. 68–77, 5 2018.

[49] S. J. Park, J. S. Jin, and J. R. Lee, "Influence of silane coupling agents on the surface energetics of glass fibers and mechanical interfacial properties of glass fiber-reinforced composites," *Journal of Adhesion Science and Technology*, vol. 14, no. 13, pp. 1677–1689, 2000.

[50] N. De Geyter, R. Morent, L. Gengembre, C. Leys, E. Payen, S. Van Vlierberghe, and E. Schacht, "Increasing the hydrophobicity of a PP film using a helium/CF4 DBD treatment at atmospheric pressure," *Plasma Chemistry and Plasma Processing*, vol. 28, no. 2, pp. 289–298, 2008.

[51] A. M. Miranda Maduro, *Influence of Curing Cycle on the Build-up of Residual Stresses and the Effect on the Mechanical Performance of Fibre Composites*. PhD thesis, DTU Wind Energy, 2021.

[52] A. Makeev, G. Seon, Y. Nikishkov, and E. Lee, "Methods for assessment of interlaminar tensile strength of composite materials," *Journal of Composite Materials*, vol. 49, no. 7, pp. 783–794, 2015.

[53] ASTM International, "Standard test method for measuring the curved beam strength of a fiber-reinforced polymer-matrix composite," tech. rep., 2013.

[54] ASTM International, "Standard test method for short-beam strength of polymer matrix composite materials," Tech. Rep. Reapproved 2006, 2011.

[55] M. A. Lieberman and A. J. Lichtenberg, *Principles of Plasma Discharges and Materials*. Hoboken, New Jersey: John Wiley & Sons, Inc., 1994.

[56] T. Yokoyama, M. Kogoma, T. Moriwaki, and S. Okazaki, "The mechanism of the stabilisation of glow plasma at atmospheric pressure," *Journal of Physics D: Applied Physics*, vol. 23, no. 8, pp. 1125–1128, 1990.

[57] U. Kogelschatz, "Dielectric-barrier Discharges: Their History, Discharge Physics, and Industrial Applications," *Plasma Chemistry and Plasma Processing*, vol. 23, no. 1-46, pp. 131–141, 2003.

[58] Y. Kusano, S. V. Singh, A. Bardenshtein, N. Krebs, and N. Rozlosnik, "Plasma surface modification of glass-fibre-reinforced polyester enhanced by ultrasonic irradiation," *Journal of Adhesion Science and Technology*, vol. 24, no. 11-12, pp. 1831–1839, 2010.

[59] Y. Kusano, S. V. Singh, K. Norrman, F. Leipold, J. Drews, P. Morgen, A. Bardenshtein, and N. Krebs, "Ultrasound enhanced plasma treatment of glass-fibre-reinforced polyester in atmospheric pressure air for adhesion improvement," *Journal of Adhesion*, vol. 87, no. 7-8, pp. 720–731, 2011.

[60] A. Chirokov, A. Gutsol, and A. Fridman, "Atmospheric pressure plasma of dielectric barrier discharges," *Pure and Applied Chemistry*, vol. 77, no. 2, pp. 487–495, 2005.

[61] W. Siemens, "Ueber die elektrostatische Induction und die Verzögerung des Stroms in Flaschendrähten," *Annalen Der Physik Und Chemie*, vol. 178, no. 9, pp. 66–122, 1857.

[62] Y. Kusano, "Doctor of Technices thesis: Atmospheric pressure plasmas for polymer surface modification: Alternating current gliding arcs and ultrasound enhanced plasmas," 2019.

[63] C. Fang, Y. Kusano, and A. Bardenshtein, "High-speed plasma treatment of polyethylene terephthalate films using ultrasound assisted dielectric barrier discharge," *Packaging technology and science*, no. April, pp. 1–7, 2021.

[64] Y. Kusano, M. Yoshikawa, K. Naito, S. Okazaki, and M. Kogoma, "Atmospheric pressure plasma polymerization of fluorinated monomers," in *Proceedings of the 7th Symposium on Plasma Science for Materials SPSM 7*, pp. 77–81, 1994.

[65] C. H. Wen, M. J. Chuang, and G. H. Hsiue, "Asymmetric surface modification of poly(ethylene terephthalate) film by CF 4 plasma immersion," *Applied Surface Science*, vol. 252, no. 10, pp. 3799–3805, 2006.

[66] J. H. Choi, E. S. Lee, H. K. Baik, S. J. Lee, K. M. Song, and Y. S. Lim, "Analysis of polymer surface treated by dielectric barrier discharge," *Plasma Sources Science and Technology*, vol. 14, no. 2, pp. 363–367, 2005.

[67] I. P. Vinogradov, A. Dinkelmann, and A. Lunk, "Deposition of fluorocarbon polymer films in a dielectric barrier discharge (DBD)," *Surface and Coatings Technology*, vol. 174-175, no. 1, pp. 509–514, 2003.

[68] I. P. Vinogradov and A. Lunk, "Dependence of surface tension and deposition rate of fluorocarbon polymer films on plasma parameters in a dielectric barrier discharge (DBD)," *Surface and Coatings Technology*, vol. 200, no. 1-4 SPEC. ISS., pp. 695–699, 2005.

[69] P. Sťahel, V. Buršíková, M. Síra, Z. Navrátil, M. L. Delgado, and J. Janča, "Deposition of teflon like coatings in surface barrier discharge," *Czechoslovak Journal of Physics*, vol. 54, no. SUPPL. 3, pp. 866–871, 2004.

[70] S. Noh, A. Y. Moon, and S. Y. Moon, "Superhydrophobic treatment using atmospheric-pressure He /C4F8 plasma for buoyancy improvement," *Japanese Journal of Applied Physics*, vol. 54, no. 4, 2015.

[71] S. Feih, J. Wei, P. Kingshott, and B. F. Sørensen, "The influence of fibre sizing on the strength and fracture toughness of glass fibre composites," *Composites Part A: Applied Science and Manufacturing*, vol. 36, pp. 245–255, 2 2005.

[72] J. L. Thomason, "The interface region in glass fibre-reinforced epoxy resin composites: 3. Characterization of fibre surface coatings and the interphase," *Composites*, vol. 26, no. 7, pp. 487–498, 1995.

[73] J. L. Thomason, "A review of the analysis and characterisation of polymeric glass fibre sizings," *Polymer Testing*, vol. 85, p. 106421, 5 2020.

[74] M. Tanoglu, S. Ziaee, S. H. Mcknight, G. R. Palmese, and J. W. Gillespie, "Investigation of properties of fiber/matrix interphase formed due to the glass fiber sizings," *Journal of Materials Science*, vol. 36, no. 12, pp. 3041–3053, 2001.

[75] A. Kelly and W. R. Tyson, "Tensile properties of fibre-reinforced metals: Copper/tungsten and copper/molybdenum," *Journal of the Mechanics and Physics of Solids*, vol. 13, no. 6, 1965.

[76] B. F. Sørensen, "Micromechanical model of the single fiber fragmentation test," *Mechanics of Materials*, vol. 104, pp. 38–48, 1 2017.

[77] E. Graciani, J. Varna, V. Mantič, A. Blázquez, and F. París, "Evaluation of interfacial fracture toughness and friction coefficient in the single fiber fragmentation test," *Procedia Engineering*, vol. 10, pp. 2478–2483, 2011.

[78] B. Miller, P. Muri, and L. Rebenfeld, "A microbond method for determination of the shear strength of a fiber/resin interface," *Composites Science and Technology*, vol. 28, no. 1, pp. 17–32, 1987.

[79] L. Yang and J. L. Thomason, "Development and application of micromechanical techniques for characterising interfacial shear strength in fibre-thermoplastic composites," *Polymer Testing*, vol. 31, no. 7, pp. 895–903, 2012.

[80] M. A. Alimuddin and M. R. Piggott, "Fracture toughness of fiber-polymer interfaces estimated from single fiber peel tests," *Polymer Composites*, vol. 20, no. 5, pp. 655–663, 1999.

[81] P. G. Jenkins, D. Bryce, G. Xypolias, and J. L. Thomason, "Micro-mechanical investigation of glass fibre/resin interface failure in mode i and mode II," *IOP Conference Series: Materials Science and Engineering*, vol. 942, no. 1, 2020.

[82] D. J. Hottentot Cederløf and B. F. Sørensen, "Characterisation of fibre/matrix interfacial fracture energy using the single fibre peel experiment," *IOP Conference Series: Materials Science and Engineering*, vol. 942, no. 1, 2020.

[83] A. Kelly, "Interface effects and the work of fracture of a vibrous composite," *Proc Roy Soc Ser A Math Phys Sci*, vol. 319, no. 1536, pp. 95–116, 1970.

[84] D. B. Marshall and W. C. Oliver, "Measurement of Interfacial Mechanical Properties in Fiber-Reinforced Ceramic Composites," *Journal of the American Ceramic Society*, vol. 70, no. 8, pp. 542–548, 1987.

[85] J.-H. Kim, D.-J. Kwon, P.-S. Shin, Y.-M. Beak, H.-S. Park, K. L. DeVries, and J.-M. Park, "Interfacial properties and permeability of three patterned glass fiber/epoxy composites by VARTM," *Composites Part B: Engineering*, vol. 148, pp. 61–67, 9 2018.

[86] D. J. H. Cederløf, Y. Kusano, and S. Fæster, "Fluorination of sized glass fibres for decreased wetting by atmospheric pressure plasma treatment in He / CF 4," *The Journal of Adhesion*, vol. 96, no. 1-4, pp. 2–12, 2019.

[87] 3B-The-fibreglass-company, "SE 3030 data sheet SE 3030," tech. rep., Battice.

[88] "Dassault Systèmes, Abaqus 6.18 documentation," 2018.

[89] ASTM International, "Standard test method for ignition loss of cured reinforced resin," tech. rep., 2011.

[90] ASTM International, "Standard test methods for constituent content of composite materials," Tech. Rep. December, 2010.

[91] T. J. Lu, Z. C. Xia, and J. W. Hutchinson, "Delamination of beams under transverse shear and bending," 1994.

[92] S. Lekhnitskiy, *Anisotropic Plates*. Moscow: Gosudarstvennoye Izdatel'stvo, 2 ed., 1957.

[93] N. Krumenacker, *Experimental study of variability and defects in vacuum-bag-only corner laminates*. PhD thesis, McGill University, 2018.

[94] B. F. Sørensen and P. Kirkegaard, "Determination of mixed mode cohesive laws," *Engineering Fracture Mechanics*, vol. 73, no. 17, pp. 2642–2661, 2006.

[95] C. Cardinaud, "Fluorine-based plasmas: Main features and application in micro-and nanotechnology and in surface treatment," *Comptes Rendus Chimie*, vol. 21, no. 8, pp. 723–739, 2018.

[96] A. Wasy Zia, Y. Q. Wang, and S. Lee, "Effect of physical and chemical plasma etching on surface wettability of carbon fiber-reinforced polymer composites for bone plate applications," *Advances in Polymer Technology*, vol. 34, no. 1, pp. 1–4, 2015.

[97] O. Teraube, J. C. Agopian, E. Petit, F. Metz, N. Batisse, K. Charlet, and M. Dubois, "Surface

modification of sized vegetal fibers through direct fluorination for eco-composites," *Journal of Fluorine Chemistry*, vol. 238, no. August, p. 109618, 2020.

[98] J. C. Agopian, O. Téraube, K. Charlet, and M. Dubois, "A review about the fluorination and oxyfluorination of carbon fibres," *Journal of Fluorine Chemistry*, vol. 251, no. September, 2021.

[99] Y. Kusano, S. Teodoru, F. Leipold, T. Andersen, B. Sørensen, N. Rozlosnik, and P. Michelsen, "Gliding arc discharge — Application for adhesion improvement of fibre reinforced polyester composites," *Surface and Coatings Technology*, vol. 202, pp. 5579–5582, 8 2008.

[100] A. Makeev, P. Carpentier, and B. Shonkwiler, "Methods to measure interlaminar tensile modulus of composites," *Composites Part A: Applied Science and Manufacturing*, vol. 56, pp. 256–261, 1 2014.

[101] M. Herráez, N. Pichler, and J. Botsis, "Improving delamination resistance through tailored defects," *Composite Structures*, vol. 247, no. February, p. 112422, 2020.

[102] X. Li, R. Tao, M. Alfano, and G. Lubineau, "How variability in interfacial properties results in tougher bonded composite joints by triggering bridging," *International Journal of Solids and Structures*, vol. 191-192, pp. 87–98, 2020.

[103] E. Lindgaard and B. L. V. Bak, "Experimental characterization of delamination in off-axis GFRP laminates during mode I loading," *Composite Structures*, vol. 220, no. April, pp. 953–960, 2019.

[104] J. W. Holmes, L. Liu, B. F. Sørensen, and S. Wahlgren, "Experimental approach for mixed-mode fatigue delamination crack growth with large-scale bridging in polymer composites," *Journal of Composite Materials*, vol. 48, no. 25, pp. 3111–3128, 2014.

[105] A. Khudiakova, A. J. Brunner, M. Wolfahrt, T. Wettemann, D. Godec, and G. Pinter, "On the investigation of quasi-static crack resistance of thermoplastic tape layered composites with multiple delaminations: Approaches for quantification," *Composites Part A: Applied Science and Manufacturing*, vol. 149, no. January, p. 106484, 2021.

[106] Z. Aslan and F. Daricik, "Effects of multiple delaminations on the compressive, tensile, flexural, and buckling behaviour of E-glass/epoxy composites," *Composites Part B: Engineering*, vol. 100, pp. 186–196, 2016.

[107] F. Jin, P. Xu, F. Xia, H. Liang, S. Yao, and J. Xue, "Buckling of composite laminates with multiple delaminations: Part I Theoretical and numerical analysis," *Composite Structures*, vol. 250, no. March, p. 112491, 2020.

[108] B. Ehrhart, B. Valeske, and C. Bockenheimer, "Non-destructive evaluation (NDE) of aerospace composites: Methods for testing adhesively bonded composites," in *Methods for testing adhesively bonded composites* (V. M. Karbhari, ed.), Woodhead Publishing Series in Composites Science and Engineering, pp. 220–237, Woodhead Publishing, 2013.

[109] K. B. Katnam, L. F. M. da Silva, and T. M. Young, "Bonded repair of composite aircraft structures: A review of scientific challenges and opportunities," *Progress in Aerospace Sciences*, vol. 61, pp. 26–42, 2013.

Appendix A

Appended papers

Included to the thesis are the following papers.

[P1] **Hottentot Cederløf, D. J.**, Kusano, Y., and Fæster, S. (2019). Fluorination of sized glass fibres for decreased wetting by atmospheric pressure plasma treatment in He/CF4. *Journal of Adhesion*, 96(1-4), pp. 2–12.

[P2] Fang, C., **Hottentot Cederløf, D. J.**, Bardenshtein, A., and Kusano, Y. (2020). Air-to-air atmospheric pressure plasma treatment – perspective for composite manufacturing *IOP Conf. Series: Materials Science and Engineering*, 942, 012030.

[P3] **Hottentot Cederløf, D. J.**, Kusano, Y., and Sørensen, B.F. (2021). Control of interlaminar strength by atmospheric pressure plasma treatment. *Submitted to Journal of Composite Interfaces*.

[P1]

Hottentot Cederløf, D. J., Kusano, Y., and Fæster, S.

FLUORINATION OF SIZED GLASS FIBRES FOR DECREASED WETTING BY ATMOSPHERIC PRESSURE PLASMA TREATMENT IN HE/CF_4.

Journal of Adhesion, 96(1-4), 2-12 (2019).

Fluorination of sized glass fibres for decreased wetting by atmospheric pressure plasma treatment in He/CF_4

Daan J. Hottentot Cederløf[a,*], Yukihiro Kusano[a], Søren Fæster[a]

[a] *Wind Energy Department, Technical University of Denmark, 4000 Roskilde, Denmark*

Abstract

Sized glass fibre bundles were treated using atmospheric pressure plasma in a helium/ tetrafluoromethane gas mixture. X-ray photoelectron spectroscopy showed that fluorine was introduced onto the sizing surface. A new analysis method (dynamic micro-wetting) to determine the wetting rate of the plasma treated fibre bundles is presented. The dynamic micro-wetting test using glycerol as a test liquid showed a reduced wetting rate after plasma treatment. It is demonstrated that dynamic micro-wetting is a useful tool for characterization of fibre bundle wetting.

Keywords: surface treatment, plasma, fibres, wetting

1. Introduction

Glass fibre composites are widely used in applications where high stiffness, low weight and low cost are required, for example in ship hulls and wind turbine blades. A common damage mechanism in composites is delamination, where adjacent plies are separated, due to out-of-plane loading, impact

*Corresponding author.
Email address: dace@dtu.dk (Daan J. Hottentot Cederløf)

VoR published in Journal of Adhesion (05/11/2019) doi/10.1080/00218464.2019.1686364

events, bolted joints or other stress concentrations. As delamination fronts (delamination cracks) grow, either statically or cyclically, structural failure may occur due to a loss of stiffness.[1,2] Various methods exist for reducing delaminations such as z-pinning[3] and inclusion of toughening particles.[4] Alternatively, a conservative design approach may be adopted, however this leads to an unnecessarily heavy structure.

Rask and Sørensen,[5] showed experimentally that when multiple delamination cracks (concept illustrated in fig. 1) occurred in double cantilever beam (DCB) specimens, the resistance to crack growth scaled proportionally to the additional number of delamination cracks. However, the occurrence of multiple delamination cracks was not controlled. Further numerical studies of DCB specimens by Goutianos and Sørensen[6] -with a second cohesive interface parallel to the primary crack interface- showed that in order to control the formation of a second crack, the interlaminar tensile strength (denoted σ_{22}^2 in fig. 1) of the second interface must be lower than the σ_{22}^1 of the primary crack interface. In other words, a weak plane must be introduced near the primary crack plane to form a second crack.

Introducing a weak plane may be achieved by inclusion of a polytetrafluoroethelene (PTFE) slip foil, a common technique for initiation of cracks in delamination experiments. To reduce the severity of a complete disbond, the PTFE foil may be perforated, so as to maintain a certain amount of interlaminar strength; as demonstrated by Kuhtz et al.[7] However, any physical barrier (with or without perforations) will hinder the formation of fibre bridg-

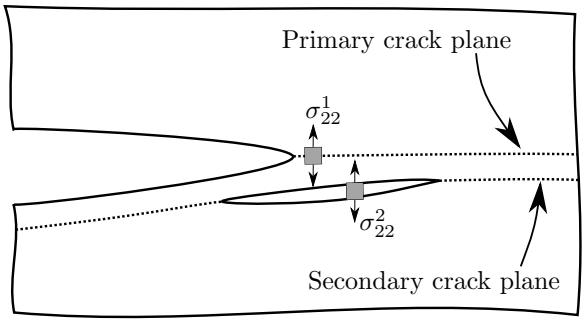

Figure 1: Illustration of the formation of multiple delamination cracks in a composite DCB specimen. The superscripts 1 and 2 refer to the primary and secondary crack planes, respectively.

ing. It is shown that fibre bridging is a toughening mechanism which is useful for reducing crack growth.[8] Fluorination of fibres, by plasma treatment prior to infusion, may be used to locally introduce a weak interface without the use of a physical barrier.

Atmospheric plasma treatment is an attractive surface modification because of its low environmental impact, selectivity in treatment and compatibility with a wide range of materials. Furthermore, it can be limited to treating material surfaces without influencing bulk properties; the treatment depth is in the order of 10 nm.[9] Polymerization, deposition, ablation and substitution can occur depending on the gas introduced in the plasma.[10] For example using a helium/ammonia (He/NH_3) mixture may introduce nitrogen onto a polymer surface.[11] Tetrafluoromethane (CF_4) is commonly used in plasma treatment of surfaces and may be used to fluorinate a polymer surface creating a de-wetting surface similar to PTFE.[12] To the authors

best knowledge, atmospheric pressure plasma treatment to locally fluorinate sized glass fibres, has not been reported before.

In all commercial glass fibre production a thin organic surface coating called sizing is applied to glass fibres to promote compatibility with the matrix. Sizing provides critical properties to the fibres and finished composite part, including: good wetting, resistance to environmental factors and a fibre-matrix interphase capable of stress transfer.[13] It is also demonstrated by Xu et al.[14] that sizing acts as a filler, reducing the fibre surface roughness and reducing the occurrence of microvoids in the fibre/matrix interface. Sizing thickness is typically in the range of 0.1 μm-10 μm, which is 1-3 orders of magnitude larger than the plasma treatment depth of 10 nm. After plasma treatment, the bulk glass fibre material and the protective role of the sizing therefore remain unchanged.

The current paper investigates the influence of dielectric barrier discharge (DBD) plasma in a He/CF_4 mixture on the surface of commercial sized glass fibre with the aim of introducing fluorine on the sizing surface. A technique of dynamic micro-wetting is presented for measuring the wetting of bundles of fibres. This technique is used to determine the change in wetting behaviour of glycerol on glass fibre bundles. X-ray photoelectron spectroscopy (XPS) and field emission scanning electron microscopy (FE-SEM) are used to characterize the elemental and morphological change of the sizing surface after plasma treatment.

2. Method

Specimens containing several bundles of sized glass fibres were cut from a non-crimp UD-0 fabric without backing reinforcement. The specimens were treated with an atmospheric pressure DBD plasma generated in a mixture of helium (He) and tetrafluoromethane (CF_4) (see fig. 2). The DBD was supplied with 3.0 SLM (standard liter per minute) of He, mixed with 0.23 SLM of CF_4. The DBD was generated between 2 water cooled electrodes; the bottom electrode (a 50 mm × 50 mm metal plate) covered by a 100 mm × 100 mm × 3 mm Alumina dielectric barrier; the top electrode is a 50 mm × 50 mm metal mesh electrode.[15] Power was supplied by an alternating-current (AC) generator at approx. 40 kHz (Generator 6030. SOFTAL Electronic GmbH, Hamburg, Germany). A high-voltage probe (PPE 20kV, LeCroy, Chestnut Ridge, NY, USA) and a 50 Ω shunt resistor were used to measure voltage and current, to determine average power input. Treatment time was 60 s, plasma power was 50 W or 100 W.

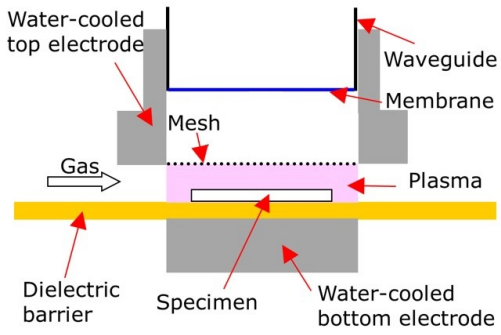

Figure 2: DBD treatment test setup

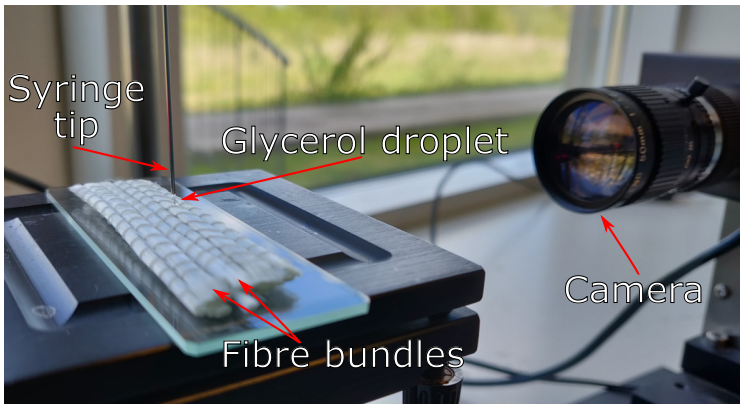

Figure 3: Contact angle measurement setup. (Full colour image available online.)

Dynamic micro-wetting tests were performed by applying a droplet (ca. 1 μL) of glycerol onto a single bundle of glass fibres using a threaded plunger syringe (setup shown in fig. 3). Glycerol was used as a test liquid because, like typical uncured resin, it has both polar and non-polar structures. Furthermore, its viscosity is representative of resin used for vacuum infusion of glass fibre composites.[16] As it wets more slowly than water it is easier to record the wetting process. A similar method, albeit with a different data processing method, is described by Shin et al.[17] Stitching fibres were not removed from the bundles in order to maintain the bundle structure. A video of the droplet was video recorded (CAM100. Crelab Instruments AB, Billdal, Sweden) as it reduced in height and spread into the bundle. Contact angles (θ) were measured at fixed time intervals and fitted with an exponential function (eq. (1)) using the curve fitting toolbox (cftool) in Matlab. In eq. (1) the constant, A, is related to the initial contact angle (i.e. eq. (1) evaluated at t=0). The α term is a measure of the wetting rate of the droplet. Measurements were performed on at least 2 points per bundle with a minimum

of 3 bundles measured per treatment type.

$$cos(\theta) = 1 - A \cdot e^{-\alpha \cdot t} \tag{1}$$

The surface structure of the glass fibres was observed by FE-SEM (Zeiss Ultra 55, Oberkochen, Germany). Specimens were sputter coated with gold (ca. 7 nm) prior to microscopy.

Elemental composition of the fibre surface was analysed by XPS. Fibre bundles were analysed using a micro focused monochromatic Al Kα X-ray source (K-alpha, ThermoFischer Scientific, Paisley, UK). An X-ray energy of 1486.6 eV was used, resulting in a lateral resolution of 30 μm. A high resolution analysis of the carbon 1s (C1s) was performed with spectra acquired over 30 scans. De-convolution was performed by curve fitting with purely Gaussian components with linear background subtraction. A full-width at half-maximum of 1.5 eV was used for C1s peaks. The peaks at roughly 285 eV, 286.5 eV and 289.5 eV can be assigned to C-H/C-C, C-O-C/C-OH and C-F, respectively.[18] Fibre samples were taken from both the bundle exterior and interior to determine treatment uniformity through the bundle cross-section. At least 3 points were analyzed per specimen.

3. Results

The results of the dynamic micro-wetting test are shown in table 1, where constant (A) and constant (α) are introduced in eq. (1) in the methodology.

A larger wetting rate, α, indicates faster wetting. A significant decrease in wetting rate was observed during the dynamic micro-wetting tests of the plasma treated specimens. Untreated specimens showed full wetting within 60 s whereas specimens treated at 100 W took >600 s.

Table 1: Dynamic micro-wetting test results: constant A and wetting rate α of contact angles.

Power [W]	Constant, A		Wetting rate, (α)		No. measurements
	Avg	±	Avg	±	
untreated	0.918	0.225	0.091	0.071	36
50	1.000	0.223	0.012	0.015	56
100	0.931	0.197	0.004	0.005	12

FE-SEM images of untreated fibre surface (figs. 4a and 4c) are compared to 100 W treated fibres (figs. 4b and 4d). Circular 'island' formations with a diameter in the order of 200 nm are recognized in both figs. 4b and 4c, these types of features were observed on all glass fibres with sizing, before and after plasma treatment (also at 50 W). The FE-SEM images generally show a smooth surface, however cracks with length of 100 nm-200 nm were observed on both treated and untreated specimens at higher magnification (figs. 4c and 4d).

XPS spectra of the plasma treated and untreated fibres are shown in fig. 5. The elemental surface compositions are summarised in table 2. A peak at

688 eV is observed for fibres treated with plasma indicating that the surface contained fluorine. Fluorine is detected after plasma treatment, on fibres from the interior and exterior of the bundle. The more powerful treatment of 100 W shows a higher fluorine content, shown by the increased F:C ratio in table 2 and larger fluorine peak in fig. 5a compared to fig. 5b. An increase in the O:C ratio is observed on interior and exterior fibres for both 50 W and

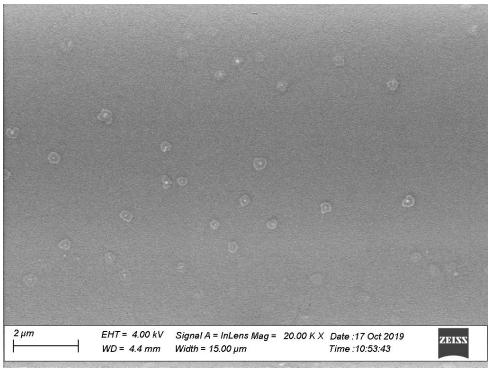

(a) Untreated fibre.

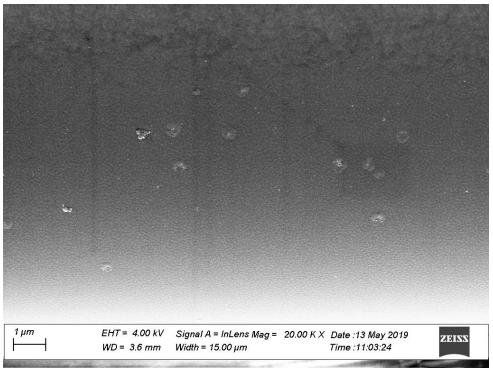

(b) Treatment: DBD 100W.

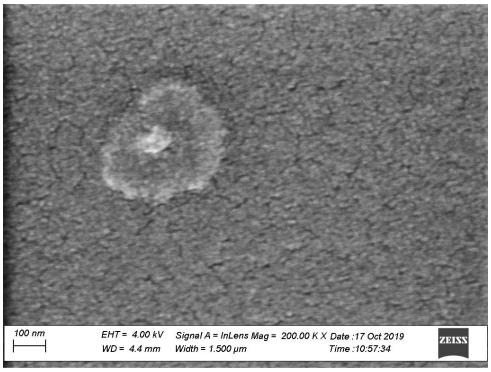

(c) Untreated fibre.

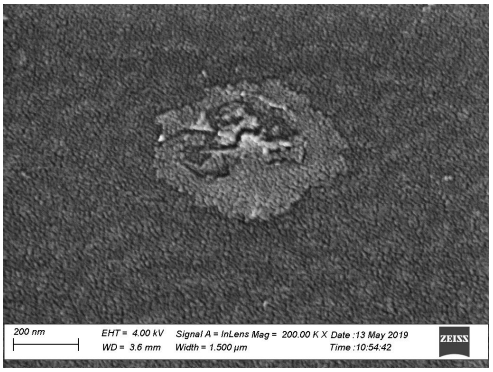

(d) Treatment: DBD 100W.

Figure 4: FE-SEM images of fibres before and after plasma treatment. (Fibre diameter = 17 μm)

100 W treatments. Figure 6 shows typical C1s spectra of the treated and untreated fibres. The peaks labelled Scan A, Scan B and Scan C correspond to C-H/C-C, C-O-C/C-OH and C-F, respectively. After treatment at both 50 W and 100 W, C-F bonds are observed. Furthermore, an increase in the treatment power results in a larger C-F peak.

Table 2: Elemental composition of glass fibre surface before and after treatment.

Power [W]	Bundle location	Elemental composition [at.%]						O:C	F:C
		C	O	F	N	Si	Ca		
-	Interior	76.0	22.9	0.0	0.0	1.1	0.0	0.29	0
	Exterior	76.8	21.9	0.0	0.0	1.3	0.0	0.29	0
50	Interior	74.7	23.3	1.4	0.0	0.6	0.0	0.31	0.040
	Exterior	75.1	23.4	1.5	0.0	0.0	0.0	0.36	0.043
100	Interior	72.9	23.5	3.6	0.0	0.0	0.0	0.33	0.055
	Exterior	71.1	23.1	5.3	0.4	0.0	0.1	0.32	0.056

4. Discussion

Atmospheric pressure plasma treatment with He/CF_4 at different plasma powers resulted in a decrease in wettability, as observed by the decrease in wetting rate, α, in table 1. The mean wetting rate is reduced by a factor of 22.8 after plasma treatment at 100 W and a factor of 7.6 after plasma treatment at 50 W. This can be attributed to the introduction of fluorine onto the fibre sizing, as observed in the XPS results in table 2 and fig. 6, creating a PTFE type de-wetting behaviour. Treatment at 50 W introduced

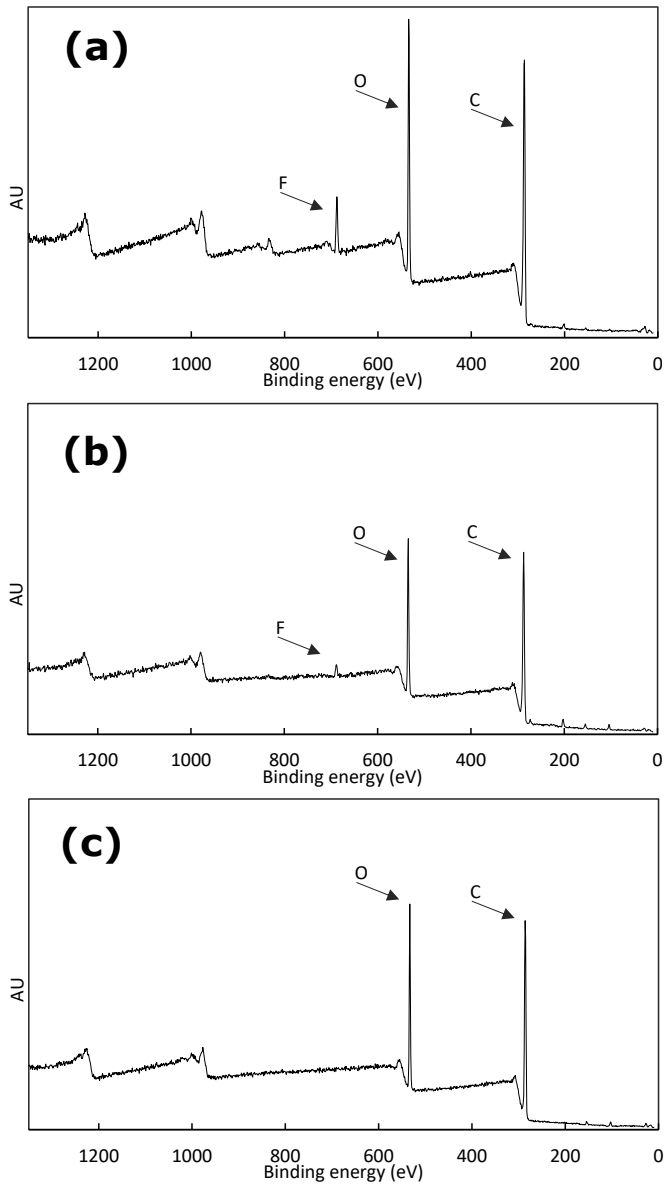

Figure 5: XPS spectra of treated and untreated fibres. (**a**) 100W DBD treatment, (**b**) 50W DBD treatment, (**c**) untreated

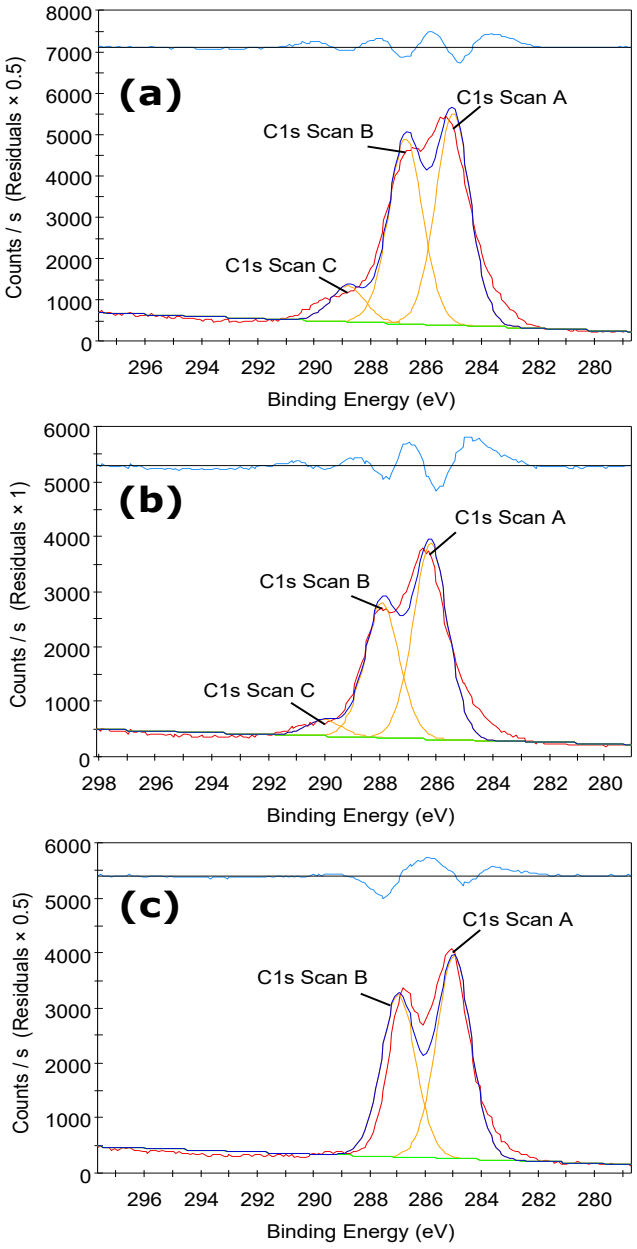

Figure 6: Typical C1s spectra of treated and untreated fibres. (**a**) 100W DBD treatment, (**b**) 50W DBD treatment, (**c**) untreated

$1.4 - 1.5 at.\%$ fluorine; at 100W the fluorine content was $3.6 - 5.3 at.\%$. Fluorine content was increased on fibres from the bundle interior as well as on fibres from the exterior, indicating that the plasma treatment was effective throughout the bundle cross-section. A comparable treatment method (DBD plasma in O_2/CF_4 on cellulose films) has been reported elsewhere[19] with an introduction of 20.3 at.% fluorine resulting in a water contact angle increase from 42.1° to 92°, i.e. a significant de-wetting behaviour. This may be used in a composite structure to introduce a weak plane between plies, similar to a foil of PTFE.

Increased surface roughness on the micro and nano scales are able to increase the hydrophobicity of an already hydrophobic surface.[12] Since a factor 1.8 difference in fluorine content was observed for the 50 W and 100 W treatments, leading to a factor 3 decrease in wetting rate, it is possible that the plasma treatment at a higher power also influenced the resulting topography. FE-SEM images showed signs of surface cracking in untreated and plasma treated specimens, however no clear difference in roughness could be observed between the treated and untreated fibres. Morphological change[16] was not observed on the sizing surface. Further analysis by atomic force microscopy (AFM) is suggested for nano scale topographical characterization of the surface since this is not detectable by FE-SEM.

A minor increase of the O:C ratio after DBD treatment was observed for the plasma treated samples, indicating that the treatment had an oxidizing effect. This is attributed to O_2 and moisture contamination from the ambi-

ent air.[15,20]

The curve fit constant, A (table 1), does not show a significant difference for treated or untreated surfaces with the mean of constant, A, showing at most a 12% difference. The value of A is related to the contact angle at time=0 (evaluating eq. (1) at t=0). Therefore, a static contact angle measurement on a bundle of fibres is not sensitive enough to indicate the effect of surface modification. Repeatable results of the dynamic micro-wetting test however shows that α, a temporal measurement, can give a better indication of surface modification than the constant A.

5. Conclusion

A DBD plasma in He/CF_4 can introduce fluorine onto sized glass fibre surfaces. Fluorine contents measured on fibres from the bundle interior and exterior indicate that the treatment was effective on fibres throughout the bundle. By introducing fluorine (1.4-5.3 at.%), wetting rates with glycerol are significantly reduced (factor 7.6-22.8) for fibres treated with plasma in He/CF_4. The dynamic micro-wetting test can successfully show the change in wetting rates after treatment at different plasma power levels and is therefore a useful tool to characterize wetting of fibre bundles.

Acknowledgements

The DACOMAT project has received funding from the European Union's Horizon 2020 research and innovation programme 5 under GA No. 761072. Special thanks to Gitte Christiansen for preparation of the microscopy specimens.

The Version of Record of this manuscript has been published and is available in the Journal of Adhesion (November 5, 2019).
https://www.tandfonline.com/doi/10.1080/00218464.2019.1686364

References

[1] Overgaard, L. C. T.; Lund, E. Structural collapse of a wind turbine blade. Part B: Progressive interlaminar failure models. *Compos. Part A Appl. Sci. Manuf.* **2010**, *41*, 271–283.

[2] Lee, H. G.; Kang, M. G.; Park, J. Fatigue failure of a composite wind turbine blade at its root end. *Compos. Struct.* **2015**, *133*, 878–885.

[3] Mouritz, A. Review of z-pinned composite laminates. *Compos. Part A Appl. Sci. Manuf.* **2007**, *38*, 2383–2397.

[4] Dadfar, M.; Ghadami, F. Effect of rubber modification on fracture toughness properties of glass reinforced hot cured epoxy composites. *Mater. Des.* **2013**, *47*, 16–20.

[5] Rask, M.; Sørensen, B. F. Determination of the J integral for laminated

double cantilever beam specimens: The curvature approach. *Eng. Fract. Mech.* **2012**, *96*, 37–48.

[6] Goutianos, S.; Sørensen, B. F. Fracture resistance enhancement of layered structures by multiple cracks. *Eng. Fract. Mech.* **2016**, *151*, 92–108.

[7] Kuhtz, M.; Hornig, A.; Richter, J.; Gude, M. Increasing the structural energy dissipation of laminated fibre composite materials by delamination control. *Mater. Des.* **2018**, *156*, 93–102.

[8] Yao, L.; Alderliesten, R. C.; Benedictus, R. The effect of fibre bridging on the Paris relation for mode I fatigue delamination growth in composites. *Compos. Struct.* **2016**, *140*, 125–135.

[9] Kusano, Y. Atmospheric pressure plasma processing for polymer adhesion: A review. *J. Adhes.* **2014**, *90*, 755–777.

[10] Li, R.; Ye, L.; Mai, Y.-W. Application of plasma technologies in fibre-reinforced polymer composites: a review of recent developments. *Compos. Part A Appl. Sci. Manuf.* **1997**, *28*, 73–86.

[11] Kusano, Y.; Mortensen, H.; Stenum, B.; Goutianos, S.; Mitra, S.; Ghanbari-Siahkali, A.; Kingshott, P.; Sørensen, B.; Bindslev, H. Atmospheric pressure plasma treatment of glassy carbon for adhesion improvement. *Int. J. Adhes. Adhes.* **2007**, *27*, 402–408.

[12] Dimitrakellis, P.; Gogolides, E. Hydrophobic and superhydrophobic surfaces fabricated using atmospheric pressure cold plasma technology: A review. *Adv. Colloid Interface Sci.* **2018**, *254*, 1–21.

[13] Thomason, J. *Glass fibre sizings: A review of the scientific literature*; James L. Thomason, 2012.

[14] Xu, P.; Yu, Y.; Guo, Z.; Zhang, X.; Li, G.; Yang, X. Evaluation of composite interfacial properties based on carbon fiber surface chemistry and topography: Nanometer-scale wetting analysis using molecular dynamics simulation. *Compos. Sci. Technol.* **2019**, *171*, 252–260.

[15] Teodoru, S.; Kusano, Y.; Rozlosnik, N.; Michelsen, P. K. Continuous plasma treatment of ultra-high-molecular-weight polyethylene (UHMWPE) fibres for adhesion improvement. *Plasma Process. Polym.* **2009**, *6*, 375–381.

[16] Kusano, Y.; Madsen, B.; Berglund, L.; Oksman, K. Modification of cellulose nanofibre surfaces by He/NH3 plasma at atmospheric pressure. *Cellulose* **2019**, *26*, 7185–7194.

[17] Shin, P.-S.; Baek, Y.-M.; Kim, J.-H.; Park, H.-S.; Kwon, D.-J.; Lee, J.-H.; Kim, M.-Y.; DeVries, K. L.; Park, J.-M. Interfacial and wetting properties between glass fiber and epoxy resins with different pot lifes. *Colloids Surfaces A Physicochem. Eng. Asp.* **2018**, *544*, 68–77.

[18] Beamson, G.; Briggs, D. *High resolution XPS of organic polymers, the Scienta ESCA300 database*; Wiley: Chichester, 1992.

[19] Siró, I.; Kusano, Y.; Norrman, K.; Goutianos, S.; Plackett, D. Surface modification of nanofibrillated cellulose films by atmospheric pressure dielectric barrier discharge. *J. Adhes. Sci. Technol.* **2013**, *27*, 294–308.

[20] Kusano, Y.; Teodoru, S.; Hansen, C. M. The physical and chemical properties of plasma treated ultra-high-molecular-weight polyethylene fibers. *Surf. Coatings Technol.* **2011**, *205*, 2793–2798.

[P2]

Fang, C., Hottentot Cederløf, D. J., and Kusano, Y.

AIR-TO-AIR ATMOSPHERIC PRESSURE PLASMA TREATMENT – PERSPECTIVE FOR COMPOSITE MANUFACTURING

IOP Conf. Series: Materials Science and Engineering, 942(1), 012030, (2020),.

IOP Conf. Series: Materials Science and Engineering **942** (2020) 012030 doi:10.1088/1757-899X/942/1/012030

Air-to-air atmospheric pressure plasma treatment – perspective for composite manufacturing

Cheng Fang[1,2], Daan Jonas Hottentot Cederløf[1], Alexander Bardenshtein[3] and Yukihiro Kusano[1,3*]

[1] Department of Wind Energy, Technical University of Denmark, Denmark
[2] Harbin Institute of Technology, People's Republic of China
[3] Danish Technological Institute, Denmark

*: corresponding author
e-mail: yuk@teknologisk.dk

Abstract. Fibre-reinforced polymer composites are gaining increasing attention in various applications for constructing mechanical structures such as wind turbine blades. The interface between fibres and a polymer matrix should be optimally designed to promote the mechanical performance of the composites. Plasma treatment shows obvious advantages over conventional approaches, since it has the characteristic of environmental friendliness, low-cost, and easy operation. A plasma can be favourably generated at atmospheric pressure. One of the most commonly used atmospheric pressure plasmas is a dielectric barrier discharge (DBD). In the present work, an air-to-air DBD is introduced. The DBD was generated in a gas mixture of helium and fluorocarbon between a rod-shaped water-cooled powered electrode covered with alumina and a one-dimensionally movable ground aluminium plate. Polyethylene terephthalate films were used as model specimens, and attached on the aluminium plate for the surface modification. The results indicate that specimen surfaces can be oxidized or fluorinated, depending on the conditions, and that the gap between the electrodes and gas flowrates significantly affect the treatment effect.

1. Introduction

Glass fibre reinforced polymer (GFRP) composites are widely used due to high strength-to-weight ratios, mechanical and corrosion resistance properties [1]. Examples of applications include sporting equipment, vehicles, architectures, and wind turbine blades.

It is indicated experimentally [2] and theoretically [3] that fracture toughness of GFRPs can be improved not by strong interactions at the interfaces between fibres and polymer matrices, but by optimally designed interfaces. More specifically, creation of multiple cracks in GFRPs due to locally distributed domains with low adhesion can improve overall fracture toughness of GFRPs. Therefore, at the initial stage of polymer composite manufacturing, surface treatment of fibres is important for controlling the interfacial properties of GFRPs. Motivated by this idea, fluorination of sized glass fibres is studied aiming at reducing initial interaction of glass fibre surfaces with polymer matrices [4,5]. Specifically, it is expected that fluorination of sized glass fibre surfaces can pronounce de-wetting of uncured matrix polymers, delay interaction between the sizing and the matrix, and that subsequent interfacial interaction can be lowered. Among the reported surface treatment techniques, atmospheric pressure plasma treatment is attractive due to its high treatment efficiency, environmental friendliness

and easy operation with simple setups [6,7]. Commonly used atmospheric pressure plasmas include corona discharge, dielectric barrier discharge (DBD) [8], cold plasma torch [9,10], and gliding arc [11-17]. DBD is generated by applying an alternating-current (AC) voltage between electrodes separated by one or more dielectrics. Simple and robust configuration of the DBD allows for design flexibility including air-to-air type continuous plasma treatment systems [18,19].

Adhesion improvement of material surfaces using plasma treatment [6,7] is commonly demonstrated by oxidation for acid-based interactions [20] and/or surface roughening for mechanical interlocking effects for the purpose of improving interactions at interfaces. By contrast, recent publications [4,5] propose designed lower interactions between glass fibre fabrics with a polymer matrix by creating a polytetrafluoroethylene (PTFE) like surface by substitution reactions between hydrogen and fluorine using a DBD in a helium/tetrafluoromethane (He/CF_4) gas mixture. However, it is reported that use of fluorocarbons such as hexafluoropropylene (HFP. C_3F_6) and octafluorocyclobutane (OFB. c-C_4F_8) in a DBD exhibits better hydrophobic effects by plasma polymerization to synthesize a PTFE like coating than use of CF_4 [21]. It is noted here that if plasma polymerization on a material surface is appropriately carried out, the surface property of the coating is generally independent of the material to be coated.

In the present work, an air-to-air DBD is introduced for investigating hydrophobic plasma surface modification in a He/OFB gas mixture. Polyethylene terephthalate (PET) films were used as model specimens to study the modification effects, since PET is easily available, and its properties are well-known. Contact angle measurements were carried out using deionized water and glycerol as test liquids for studying wetting characteristics. X-ray photoelectron spectroscopy (XPS) was used to characterize the elemental analysis of the modified PET film surfaces.

2. Experimental methods

A photo image and a diagram of the DBD setup are shown in Fig. 1. The powered electrode is water-cooled cylindrical metallic tube covered with an alumina tube. Inner and outer diameters of the alumina tube are 12 and 16 mm, respectively. The lower ground electrode is an aluminium plate (280 mm x 400 mm). The gap between the alumina tube and the aluminium plate was adjusted to 0.6 mm or 2.0 mm. He and OFB were used as a dilute gas and a reactive gas, respectively. A flowrate of He was adjusted between 14.5 and 29 standard litre per minute (SLM). OFB flowrate was adjusted between 0.066 and 0.262 SLM. A gas mixing ratio (MR) is defined in equation (1).

$$MR = F_{OFB} / (F_{He} + F_{OFB}) \times 100 \text{ (vol. \%)}, \quad (1)$$

where F_{OFB} and F_{He} are the flowrates of OFB and He, respectively.

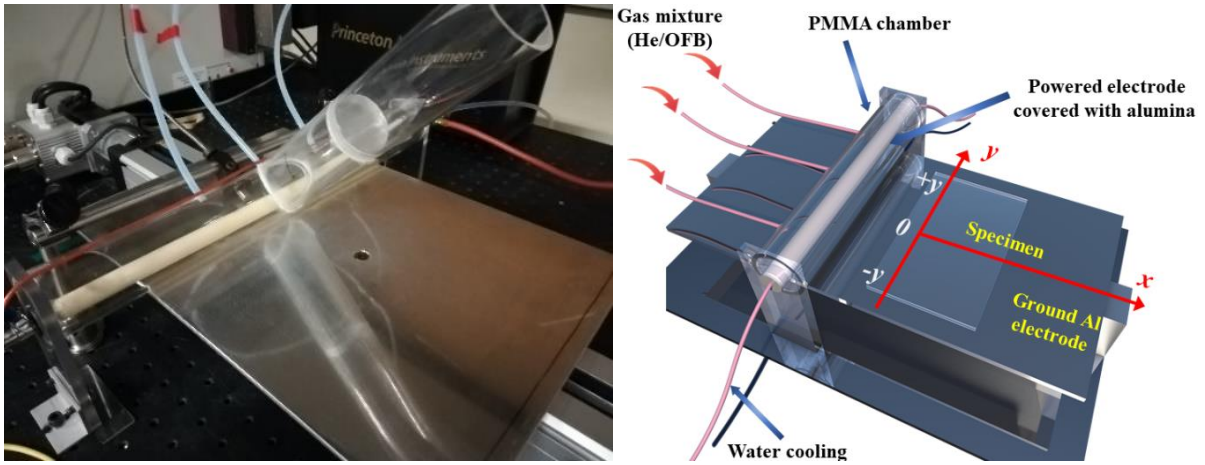

Fig. 1 A photo image and a diagram of the air-to-air atmospheric pressure DBD setup.

He gas was pre-mixed with OFB, and then introduced into a poly-methyl-methacrylate (PMMA) chamber, separating the gas mixture from the surrounding atmosphere. The bottom part of the PMMA chamber facing the aluminium plate is open to air so that the DBD was generated between the alumina tube and the aluminium plate. The DBD was driven by an AC power supply (Generator 6030, SOFTAL Electronic GmbH, Germany) at a frequency of approximately 40 kHz. Untreated general-purpose PET films with thickness of 65 μm were used as specimens. They were attached on the aluminium plate at positions in a y-axis direction of "-y" (approximately 5 cm from the edge of the aluminium plate), "0" (centre) and "+y" (approximately 5 cm from the edge of the aluminium plate). The aluminium plate was moved forward and backward in an x-axis direction at a speed ranging from 1 to 100 mm/s. The specimens were exposed to the DBD once or four times. The average power input was obtained by measuring voltage and current with a high-voltage probe and a 10 **Ω** current viewing resistor, respectively. The power of each treatment was adjusted to 100 W.

Static contact angles of deionized water and glycerol on the PET films before and after the treatment were measured in air at room temperature using a contact angle measurement system (CAM100; Crelab Instruments AB, Sweden). Here, deionized water is characterized by its significantly polar nature, and is the most commonly used test liquid for the contact angle measurement. Glycerol is also often used as a test liquid, exhibiting both polar and non-polar nature with high viscosity. Glycerol is considered to be an appropriate test liquid for screening adhesion properties of polymer surfaces due to similarities of physical properties to general adhesives and uncured resins [22].

XPS data were collected using a monochromatic Al K_α X-ray source with a lateral resolution of 30 mm (K-alpha; ThermoFischer Scientific, UK) to study the changes of the elemental composition at the PET film surfaces. Atomic concentrations of each element were calculated by determining the relevant integral peak intensities subtracting a linear background.

3. Results

A photo image of the DBD in the He/OFB gas mixture is exemplified in Fig. 2. The discharge looks a mixture of filamentary and glow-like discharges. It was confined between the electrodes, and spread along the powered electrode in the y-axis direction. The photoemission on the right side in Fig. 2, corresponding to +y direction, was more intense than at the centre and at the left-hand side. The difference of the photoemission is related to the uniformity of the plasma and treatment, which will be discussed below.

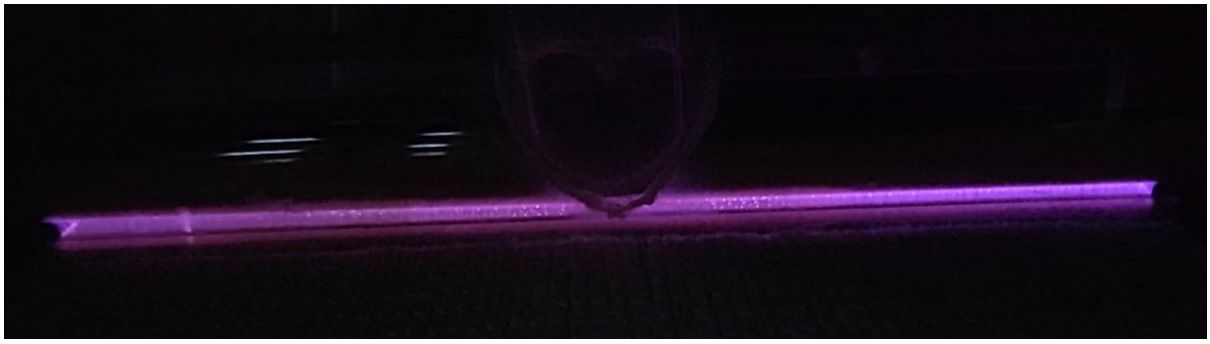

Fig. 2. A photo of the DBD in He/OFB gas mixture (gap: 2.0 mm, MR value: 0.45 %). The purple colour indicates photo-emission from the DBD between the cylindrical powered electrode and the ground electrode.

The voltage and current waveforms of the DBD in the He/OFB gas mixture are shown in Fig. 3. The voltage waveform was sinusoidal. The phase shift was approximately π/4, indicating that the DBD is

primarily a capacitively coupled plasma. Generation of the DBD in each half period deformed the current waveform from the sinusoidal feature.

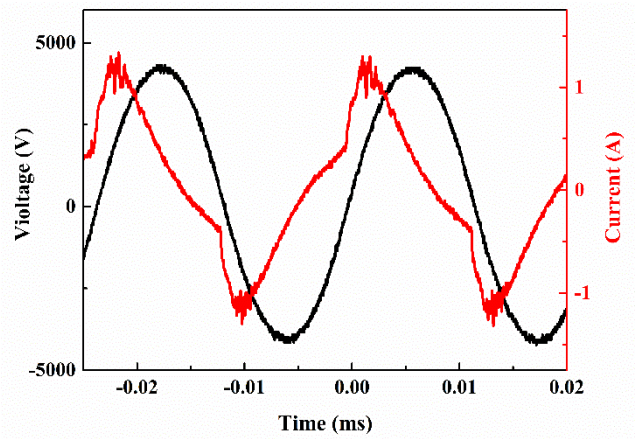

Fig. 3. An example of voltage (black) and current (red) waveforms of the DBD in He/OFB gas mixture (gap: 2.0 mm, MR value: 0.45 %).

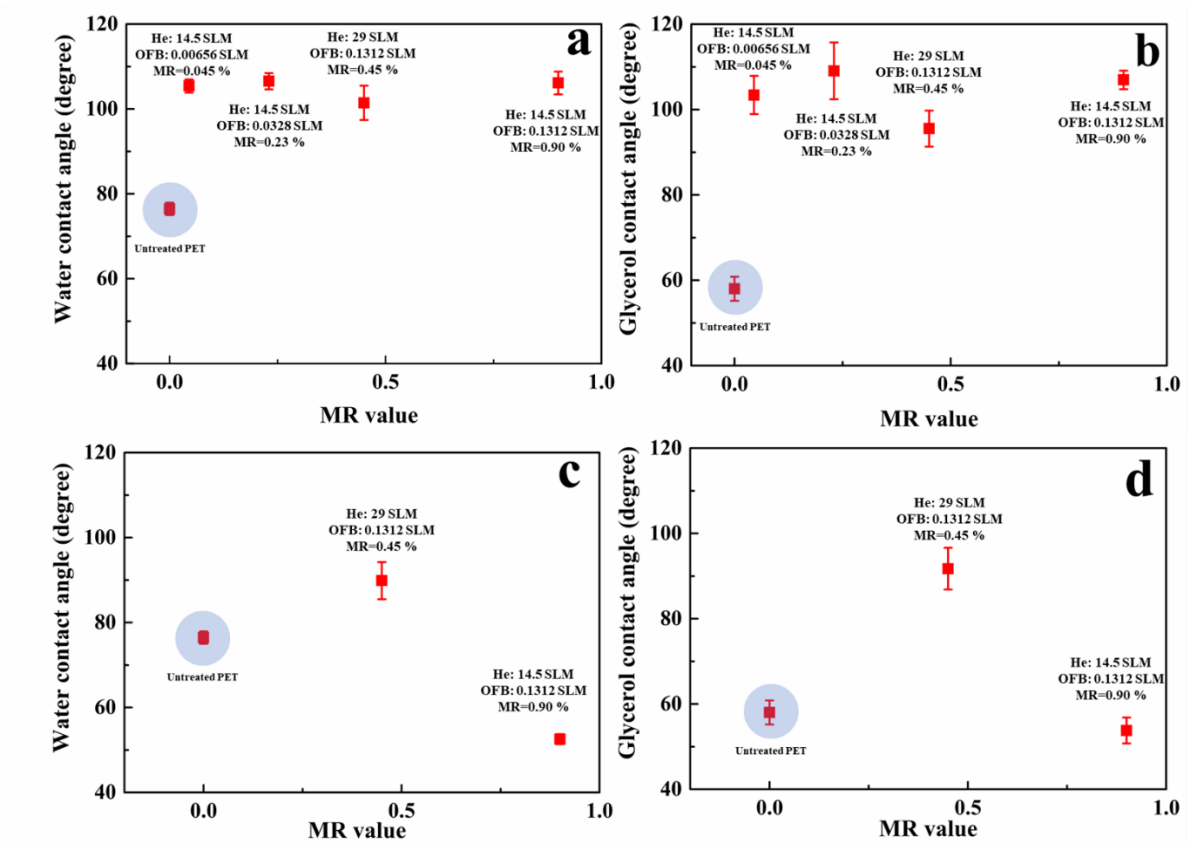

Fig. 4. Contact angles of deionized water and glycerol with the gaps of 0.6 mm (a, b) and 2.0 mm (c,d). (exposure: 4 times, MR value: 0.045 %, 0.23 %, 0.45 %, and 0.90 %). The contact angles for the untreated PET are also plotted in each figure.

In order to investigate the influence of different plasma process parameters on the wettability of the PET surfaces, static contact angles of deionized water and glycerol were measured after treatment. PET films without treatment were also tested for comparison and the values for deionized water and glycerol were 76.4 ± 1.5 and 58.0 ± 2.8 degrees, respectively. The gas content in a plasma is an important parameter for atmospheric pressure plasma processing. It depends on flowrates of the gases, the MR value, introduction of air from the surrounding, and consumption of the reactive gas by polymerization and/or decomposition in the plasma. The gap between the two electrodes, which affects the introduction of atmospheric air into the DBD, was first set to the minimum value of 0.6 mm. The MR value was set to 0.045 %, 0.23 %, 0.45 %, or 0.90 %. PET films were placed at the "0" position on the aluminium plate (see Fig. 1) and exposed to the DBD four times. Results of the contact angle measurement of the PET films treated under different conditions are summarized in the Fig. 4 (a,b). The contact angle increased greatly after each treatment.

Next, the gap was set to 2.0 mm and similar experiments were carried out. Fig. 4 (c,d) illustrates the results of the contact angle measurement, showing a different trend from the smaller gap in Fig. 4 (a,b). When the MR value was set from 0.045 to 0.45 %, the contact angles of deionized water and glycerol increased, but were lower than the values achieved at the gap of 0.6 mm. When the MR value was 0.9 % by decreasing the He flowrate from 29 SLM to 14.5 SLM, the contact angles were even lower than those of the original PET films.

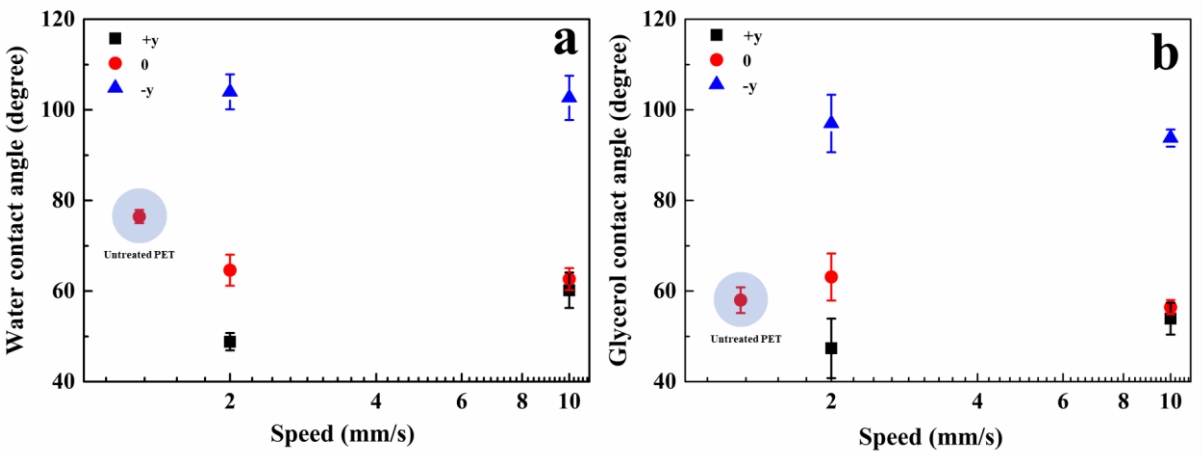

Fig. 5. Contact angles at position of –y, 0, and +y. (a) deionized water, (b) glycerol (exposure: once, gap: 2.0 mm, MR value: 0.45 %, He flowrate: 29 SLM). The contact angles for the untreated PET are also plotted in each figure.

Since the DBD can treat an up to A4 size specimen (210 mm x 300 mm), it is worth investigating the treatment uniformity. In addition, time for treatment is an important parameter for practical applicability of the processing. It can be changed by the number of the exposures and the moving speed of the aluminium plate. In the following experiments, the number of exposures is fixed to one time. In addition, the PET films were fixed at the positions of "-y", "0" and "+y", the moving speed was varied between 1 and 100 mm/s, and the gap and the He flowrate were fixed at 2.0 mm and 29 SLM, respectively.

The MR value was fixed at 0.45 %, and contact angles of deionized water and glycerol were measured after the treatments as shown in Fig. 5. The result indicates that the treatment was significantly uneven. The "-y" position became highly hydrophobic. On the other hand, at the "0" and "+y" positions, the water contact angle was slightly lowered from the original value of 76.4 degrees, and the glycerol contact angle did not change significantly from the original value of 58.0 degrees.

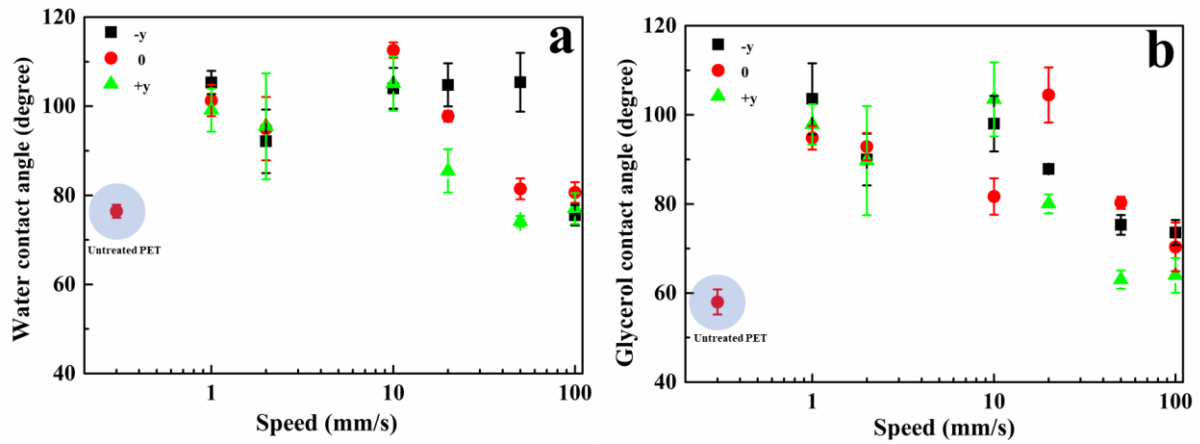

Fig. 6. Distributions of contact angles at positions –y, 0, and +y. (a) deionized water, (b) glycerol (gap: 2.0 mm, exposure: once, MR value: 0.90 %, He flowrate: 29 SLM). The contact angles for the untreated PET are also plotted in each figure.

The flowrate of OFB was increased from 0.131 SLM to 0.262 SLM with a fixed He flowrate of 29 SLM, and the similar experiment was carried out (MR value: 0.90 %). The results of the measured contact angles are summarized in Fig. 6. The uniformity of the treatment was generally improved, compared with the results in Fig. 5. At higher speeds, the contact angle approaches the values of the untreated PET films.

Table 1. XPS elemental analysis of the PET films (gap: 2.0 mm, exposure: once, MR value: 0.90 %).

Speed (mm/s)	*Position*	*Atomic content (at.%)*			*Contact angle (°)*	
		C	F	O	Water	Glycerol
-	-	75.8	0.0	24.2	76.4 ±1.5	58.0± 2.8
1	-y	45.5	52.4	2.1	105.3 ±2.6	103.6± 8.0
	0	48.5	25.6	26.0	101.3 ±3.5	94.9± 2.7
	+y	36.6	36.6	26.8	99.1 ±4.8	97.8± 4.5
10	-y	45.5	39.9	14.6	104.8 ±4.6	98.0± 6.2
	0	55.2	13.2	31.6	112.6 ±1.8	81.7± 4.1
	+y	52.9	17.5	29.6	105.1 ±6.1	103.5± 8.3

XPS measurements were carried out to analyze the elemental composition of the PET film surfaces before and after the plasma treatments. Table 1 summarizes the results XPS together with contact angles. The plasma conditions were the same as those in Fig. 6, and the moving speed was 1 or 10 mm/s. The

untreated PET film surface was dominated by carbon (C) and oxygen (O) atoms without fluorine (F) atoms. After each treatment, F atoms bonded with C were introduced at the surfaces. The F content on the film surfaces tended to be higher at the slower speed. Compared with the "0" and "+y" positions, the F content at the "-y" position was significantly higher at each speed. Specifically, the F content of the film was 52 at.% when the speed was 1 mm/s. At the "0" and "+y" positions, the O content was higher than the untreated one. In other words, both fluorination and oxidation simultaneously occurred at these positions.

4. Discussion

The discharge mode of the DBD is discussed by comparing the visual observation of the plasma in Fig. 2 with the voltage current waveforms in Fig. 3. The overall deformation in the current waveform from the sinusoidal feature suggests an increase in the electrical impedance by the generation of a bulk plasma, while the complex spiky current waveform indicates formation of filamentary micro-discharges, which agrees with the observation of the DBD in Fig. 2.

Measurement of wetting characteristics gives direct indication of surface treatment effects. Fig. 4 (a,b) indicates that the DBD treatment could effectively increase the hydrophobicity of the PET surfaces when the gap was 0.6 mm. On the other hand, when the gap was 2.0 mm, the surfaces did not show hydrophobicity when the He flowrate was lowered as shown in Fig. 4 (c,d). The results demonstrate that the electrode gap has a great impact on the treatment effect. Furthermore, it is suggested that oxidation and/or etching on the PET film surfaces would take place with the gap of 2.0 mm. When the gap becomes larger, the gas flowrates should be increased to account for extra leakage.

The measured result in the unevenness of the wettability shown in Fig. 5 can be related to the uniformity of the gas mixture in the DBD. The photo in Fig. 2 was captured in the same condition. The intense photoemission at "+y" position indicates the lower OFB content in that region. It can be due to insufficient gas mixing process of He and OFB, or uneven local consumption of OFB. It is therefore worth increasing the flowrate of OFB or the MR value as demonstrated in Fig. 6. The result confirms that the treatment can be more uniform by the higher MR value at the high He flowrate.

It is interesting to compare the XPS result with the result of the contact angle measurement in Table 1. It seems that the measured contact angles would be rather insensitive against the significant difference of the F and O contents at different positions. One possible explanation of the discrepancy is that each position would be sufficiently fluorinated to be hydrophobic, and that the differences of the F and O contents may not necessarily affect the contact angles. However, additional investigation will be necessary for further improving the uniformity of the plasma treatment.

5. Conclusion

An air-to-air DBD plasma in a He/OFB gas mixture can introduce fluorine and promote hydrophobicity of the PET films. The flowrates of the gases and the gap of the electrode played important roles for the treatment effects, attributed to the gas content in the plasma. The measured wetting characteristics of hydrophobicity was rather insensitive to the difference in elemental composition of the PET surfaces. The technique presented can be used for continuous air-to-air surface modification of sheet-like specimens including glass fibre fabrics, indicating industrial feasibility of the technology for fibre composite manufacturing.

Acknowledgements

The DACOMAT project has received funding from the European Union's Horizon 2020 research and innovation programme 5 under GA No. 761072. Cheng Fang's work was supported by the Harbin Institute of Technology Scholarship Fund. Research technician Jonas Kreutzfeldt Heininge is acknowledged for design and construction of the air-to-air DBD.

References

[1] Information on https://www.sintef.no/projectweb/dacomat/ "DACOMAT - Damage Controlled Composite Materials". The European Union's Horizon 2020 research and innovation programme under GA No. 761072. Coordinator: SINTEF, Norway. The website inspected on 24th August 2020.
[2] Rask M, Sørensen B F 2012 Eng. Fract. Mech. **96** 37–48
[3] Goutianos S, Sørensen B F 2016 Eng. Fract. Mech. **151** 92–108
[4] Cederløf D J H, Fæster S, Kusano Y 2020 J. Adhesion **96** 2-12
[5] Kusano Y, Cederløf D J H, Fæster S 2020 Key Eng. Mater. **843** 159-164
[6] Kogoma M, Kusano M, Kusano Y 2011 Nova Science Publishers
[7] Kusano Y 2014 J. Adhesion **90** 755-777
[8] Kogelschatz K U 2003 Plasm. Chem. Plasm. Proc. **23** 1-46
[9] Mortensen H, Kusano Y, Leipold F, Rozlosnik N, Kingshott P, Sørensen B F, Stenum B, H Bindslev 2006 J. Appl. Phys. **45** 8506-8511
[10] Lee B J, Kusano Y, Kato N, Horiuchi T, Koinuma H 1997 Jpn. J. Appl. Phys. Pt **36** 2888-2891
[11] Fridman A, Nester S, Kennedy L A, Saveliev A, Mutaf-Yardimci O 1999 Prog. Energy Combustion Sci **25** 211–231
[12] Zhu J J, Ehn A, Gao J L, Kong C D, Aldén M, Larsson A, Salewski M, Leipold F, Kusano Y, Li Z S 2017 Optics Express **25** 20243-20257
[13] Kusano Y, Berglund L, Aitomäki Y, Oksman K, Madsen B 2016 Mater. Sci. Eng. **139** 012027
[14] Kusano Y, Salewski M, Leipold F, Zhu J J, Ehn A, Li Z S, Aldén M 2014 Eur. Phys. J. D **68** 319
[15] Kusano Y 2009 Surf. Eng. **25(6)** 415-416
[16] Zhu J J, Gao J L, Ehn A, Aldén M, Li Z S, Larsson A, Kusano Y 2017 Phys. Plasmas **24** 013515
[17] Kusano Y, Zhu J J, Ehn A, Li Z S, Aldén M, Salewski M, Leipold F, Bardenshtein A, Krebs N 2015 Surf. Eng. **31(4)** 282-288
[18] Teodoru S, Kusano Y, Rozlosnik N, Michelsen P K 2009 Plasm. Proc. Polym. **6** S375-S381
[19] Kusano Y, Andersen T L, Michelsen P K 2008 J. Phys. Conf. Ser. **100** 012002
[20] Mittal K L 1977 Polym. Eng. Sci. **17** 467-473
[21] Kusano Y, Yoshikawa M, Naito K, Okazaki S, Kogoma M 1994 SPSM **7** 77-81
[22] Kusano Y, Madsen B, Berglund L, Oksman K 2019 Celulose 26 7185-7194

[P3]

Hottentot Cederløf, D. J., Kusano, Y., and Sørensen, B. F.

CONTROL OF INTERLAMINAR STRENGTH BY ATMOSPHERIC PRESSURE PLASMA TREATMENT

Journal of Composite Interfaces, [submitted].

Control of interlaminar strength by atmospheric pressure plasma treatment

Daan J. Hottentot Cederløf[a,*], Yukihiro Kusano[b], Bent F. Sørensen[a]

[a] *Wind Energy Department, Technical University of Denmark, 4000 Roskilde, Denmark*
[b] *Danish Technological Institute, Taastrup, Denmark*

Abstract

Properties of fibre reinforced composites are significantly controlled by the fibre/matrix interface. A method for controlling delamination cracks by introducing fluorine onto the surface of sized glass fibres is presented. The treatment consists of passing glass fibre fabrics through an atmospheric pressure plasma generated in a fluorocarbon containing gas. Wetting of polar liquid on the fabric is decreased significantly, as demonstrated by the dynamic micro-wetting test. The high treatment condition showed a decrease in interlaminar tensile strength and interlaminar shear strength in addition to control of the location of damage initiation. Microscopy and fibre volume fraction analysis do not show an increase in porosity in the fluorinated samples.

Keywords: Curved beam, ILSS, composite materials, fluorination, interface

1. Introduction

Delamination is a key driver of failure in composite structures such as wind turbine blades. It is therefore of great interest to develop toughening mechanisms to enhance the resistance to crack growth. The formation of multiple parallel delaminations with large scale bridging zones have been shown to increase the resistance to damage growth [1; 2]. However, in both studies the formation of multiple delaminations was not controlled i.e. not

*Corresponding author.
Email address: dace@dtu.dk (Daan J. Hottentot Cederløf)

created on purpose. The mode II specimens and two out of six mode I specimens showed multiple cracks in the study by Kusano et al. [2]. In the study by Rask and Sørensen [1], none of the mode I specimens showed multiple cracks whereas mixed mode specimens with a particular layup showed two crack tips, mixed mode specimens with another layup developed three crack tips. For the specimens with three crack tips the steady-state fracture resistance was 3 times the fracture resistance of the specimens with one crack tip.

It is shown numerically and analytically by Goutianos and Sørensen [3; 4] that in order to control the formation of a second delamination crack once a primary delamination has formed, the interlaminar tensile strength (denoted $\hat{\sigma}_{22}^2$ in fig. 1) of the secondary plane must be lower than the interlaminar tensile strength of the primary plane ($\hat{\sigma}_{22}^1$). Inclusion of a polytetrafluoroethylene (PTFE) film may achieve this goal by decreasing the $\hat{\sigma}_{22}^2$ to zero. The aim of the present work, however, is to achieve a controlled decrease in $\hat{\sigma}_{22}^2$, without introducing a full disbond between the fibre composite plies. This effect is similar to a so called 'partial bond' [5].

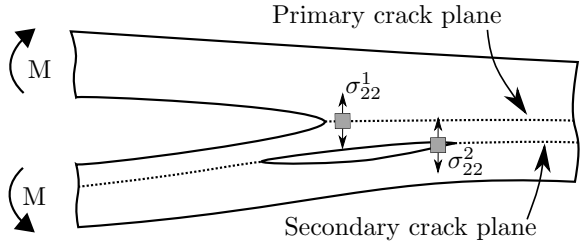

Figure 1: Illustration of the formation of multiple delamination cracks in a composite specimen with applied bending moments. The superscripts 1 and 2 refer to the primary and secondary crack interfaces/planes, respectively.

In previous studies [6; 7; 8], it was shown that the introduction of fluorine onto the fibre sizing surface, significantly reduced the wetting properties of the fibres. It is also reported that lower wettability of sized glass fibres is correlated to lower fibre/matrix interfacial strength [9; 10; 11; 12]. In the present study it is hypothesized that the introduction of fluorine onto the surface of unimpregnated sized glass fibres by means of atmospheric pressure plasma treatment is able to locally reduce the wetting properties of the fibres and thereby reduce the interlaminar tensile strength in a composite

laminate. The controlled reduction in interlaminar tensile strength is a step to achieving controlled multiple delamination cracks in a laminate.

Plasma treatment is often used because it can be used to treat a local area of the material. The bulk material properties remain unchanged since the treatment only affects the surface properties of the material. Furthermore, the use of an atmospheric pressure plasma allows for treatment without the use of a vacuum chamber, which often limits treatments to small batches or volumes. Previous work showed that a plasma generated in a mixture of tetrafluoromethane (CF_4) and helium (He) in a small plasma chamber could effectively introduce fluorine onto sized glass fibre surfaces [6]. A mixture of helium and octofluorocyclobutane (OFB) (C_4F_8), a fluorine containing gas, has been shown to be effective at polymerizing fluorine onto polymer surfaces [13; 14].

To determine whether the proposed plasma treatment will reduce the interlaminar strength of the composite, two mechanical tests are performed. These tests are specifically designed for characterisation of interlaminar properties. The curved beam test (ASTM D6415) [15] is used for interlaminar tensile strength (ILTS) and the short beam shear test is used to determine the interlaminar shear strength (ILSS). The short beam shear test has been used in numerous studies on fibre/matrix interphase properties [10; 12; 16]. The curved beam test however, is not commonly employed.

The curved beam test subjects an L shaped specimen to four point bending, introducing pure bending moments in the straight sections of the specimen. In the curved gauge region of the specimen the two opposing moments result in a concentrated tensile radial stress (i.e. in the thickness direction), this is illustrated in fig. 2. In other tests, such as the ASTM D7291 [17], to determine out of plane strength, a large area is normally subjected to a constant stress [18]. The curved beam test, however, subjects a small gauge area to a highly concentrated stress. Lu et al. [19] performed analytical and numerical studies of curved beams with an initial crack. They showed that the mode mixity, ψ (defined as the ratio of mode I and mode II stress concentration factors) increases almost linearly with the angular position of the crack. This means that when the crack initiates it is a mode I crack, as the crack extends towards the straight section it transitions to a mode II crack [19]. Therefore the test can only give results for mode I crack initia-

tion, any crack propagation results can only be used if the mode mixity is known as a function of the crack position. Extensive studies by Makeev et al. [18; 20] have shown that the curved beam test is not suitable for determining interfacial properties for use in design since it underpredicts the true material strength. However as a comparative method, in this case comparing fibre surface treatments, it is deemed suitable. A recently developed short beam method by Makeev et al. [18; 21] has shown promising results, however requires a thick laminate (>20mm).

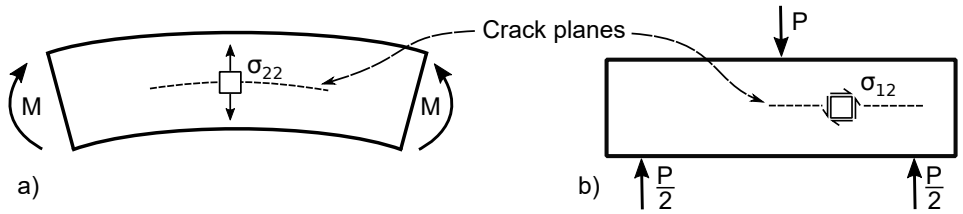

Figure 2: Illustration of the loading and stress state in the curved beam test (a) and short beam shear test (b). Dashed line indicates plane of maximum stress.

The interlaminar tensile strength of the curved beam was obtained from a simplified version of an analytical formulation by Lekhnitskii for anisotropic curved beams [22; 15],

$$\hat{\sigma}_{22} = \frac{3M}{2wt_C\sqrt{r_i r_o}} \tag{1}$$

where, M is the applied moment; t_C and w are the thickness and width; and r_i and r_o are the inner and outer radius of the curved section, respectively.

The most common test method for determination of the interlaminar shear strength is the short beam shear test [23]. The short beam shear test is a three point bending test used to determine interlaminar properties. A schematic of a loaded specimen is shown in fig. 2, in which the plane of maximum shear stress where shear cracks initiate is shown. While the curved beam test has a small area of the specimen is subject to a concentrated stress, the short beam shear test specimen has a relative large area with near uniform shear stress. For the short beam shear specimen, the maximum shear stress is obtained as [23],

$$\hat{\sigma}_{12} = \frac{3}{4}\frac{P_m}{bh} \tag{2}$$

where (P_m), (b) and (h) are the peak observed load, specimen width and specimen thickness, respectively.

In this paper, glass fibre fabrics are treated with a plasma generated in a fluorine containing gas mixture (OFB/He). These fabrics are used to prepare fibre reinforced composite laminates. Two mechanical tests are carried out to experimentally determine the interlaminar tensile strength (ILTS) and interlaminar shear strength (ILSS) for laminates made with untreated fabrics and laminates that include one ply which has been plasma fluorinated. The curved beam test (ASTM D6415 [15]) is used to determine the ILTS. ILSS is determined by means of the short beam shear test (ASTM D2344 [23]).

2. Materials and experimental methods

2.1. Materials

Uni-directional (UD) non-crimp glass fibre fabrics (W3030 2400tex, Hexcel, Duxford, UK) were used. The resin system used in this study is a commercial vinylester (DION VE1260, Polynt A/S, Sandefjord, Norway).

2.2. Plasma treatment

The fabrics were treated using a dielectric barrier discharge (DBD) device generating an atmospheric pressure plasma in a mixture of helium (He) and octo-fluorobutane (OFB). The gas mixture was continuously fed into the plasma chamber with a flow rate of 29 standard liters per minute (SLM) He and 0.262 SLM OFB. The DBD was generated between a grounded aluminium movable plate electrode (280mm x 400mm) and a powered water-cooled rod-shaped electrode insulated by an alumina dielectric barrier as shown in fig. 3. The speed of the lower movable plate electrode (in the x direction) was controlled using a linear actuator. An alternating current (AC) at approx. 40kHz was applied to the water cooled powered electrode by an AC power generator (Generator 6030. SOFTAL Electronic GmbH, Hamburg, Germany). A high voltage probe (PPE 20kV, LeCroy, Chestnut Ridge, NY, USA) and shunt resistor were used to measure voltage and current, respectively, from which power consumption was calculated. Power was

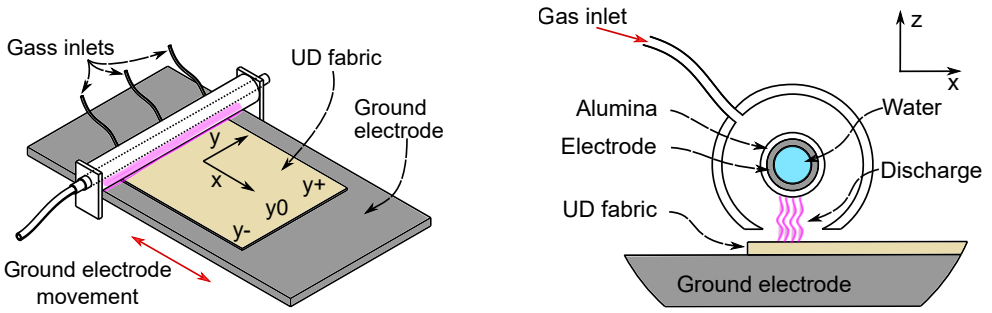

(a) (b)

Figure 3: Illustration of DBD device with fabric sample. **(a)** 3D visualization of DBD device, indicating the direction of motion of the ground electrode and coordinate system used for treatment measurements. **(b)** Cross sectional view of the DBD device, showing both electrodes and fabric sample.

controlled to be 100W for both treatments. The DBD device is described in greater detail by Fang et al. [13].

The fabric samples were 210mm in width and 240mm in length and thus did not span the entire width of the electrode (280mm). Two treatment speeds were used: 1mm/s and 10mm/s.

A poly(methyl methacrylate) (PMMA) chamber encapsulates the powered electrode, separating the plasma gas from ambient air and contains three ports for introduction of the gas mixture. An opening in the lower side of the PMMA chamber faces the movable ground electrode, with the DBD generated between the alumina tube and the ground electrode. In fig. 3b, the opening through which the plasma discharge is generated, is illustrated.

Both optical (3840x2160 pixel sensor) and infrared (640x480 pixel sensor) (Optris PI 640, Berlin, Germany) cameras were used to record images of the treatment process.

2.3. Fibre surface characterization

Fibre bundles were analysed after plasma treatment (before resin infusion) by X-ray Photoelectron Spectroscopy (XPS). A micro focused monochromatic Al K α X-ray source (K-alpha, ThermoFischer Scientific, Paisley, UK)

with X-ray energy of 1486.6 eV was used. Two scans were used for survey analysis and 30 scans were used for high resolution C1s analysis.

Wetting tests were performed using the dynamic micro wetting technique [6]. In these tests, a droplet of glycerol (as resin substitute) is placed on a fabric bundle and its shape is recorded using a camera equipped with a macro lens (CAM100. Crelab Instruments AB, Billdal, Sweden). The contact angle, θ, defined in fig. 4, was recorded as a function of time for up to 15 minutes. The contact angle was calculated by eq. (4), where A and α are fitting parameters and t is time. The fitting parameter α is a measure of wetting rate, a larger α indicates faster wetting behaviour. The fitting parameter, A, has been shown to be related to the initial condition of the droplet (i.e. at t=0)[6] and is not of significance in this study.

$$\theta = 2\angle BAC \tag{3}$$

$$cos(\theta) = 1 - A \cdot e^{-\alpha \cdot t} \tag{4}$$

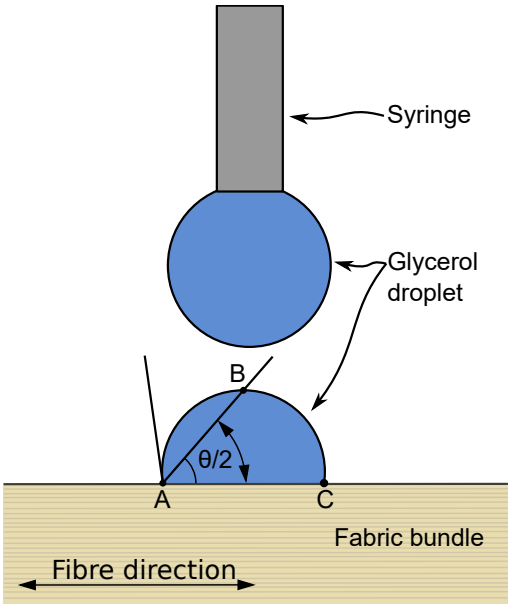

Figure 4: Sketch of dynamic micro wetting test.

2.4. Manufacturing of test specimens

Curved beam laminates were produced using four plies of UD fabric placed on the outside an inverted V-shaped steel mould. The steel mould corner radius was machined to 6.4mm to conform to the dimensions specified in the D6415 ASTM standard [15]. Mould release (ZYVAX-slipcoat WATER SHIELD, Granudan ApS, Stenløse, Denmark) was applied two times to the steel mould prior to layup. The plies were cut to 210mm x 240mm (transverse fibre direction and fibre direction, respectively). The plies were oriented on the mould so that the fibres run continuously along the legs and around the bend of the curved beam. Only one out of four plies was treated with plasma (ply number 3 in fig. 5).

A perforated peel-ply and flow mesh were placed between ply 1 and the vacuum bag. The fabrics were impregnated with a commercial vinylester resin resin (DION VE1260, Polynt A/S, Sandefjord, Norway) by vacuum infusion. The resin was thoroughly mixed with an accelerator (Norox PBC21, United Initiators GmbH, Pullach, Germany) (2.5% by weight) and degassed for 5 minutes prior to infusion. The vacuum pressure during infusion was kept at 800 mbar. Once infusion was complete the vacuum pressure was decreased to 600 mbar before fully sealing the mould. The laminate was first cured for 24 hours at room temperature followed by a 16 hour cure at 60°C.

Short beam shear specimens were cut from the straight portion of the curved beam samples. The specimen length was six times the thickness and the specimen width was two times the thickness, in accordance with the ASTM standard D2344 [23].

Manufacturing quality was analysed by means of fibre volume fraction analysis and environmental scanning electron microscopy (ESEM). Fibre volume fraction (FVF) and porosity fraction were determined by the burn-off method following ASTM standards D2584 [24] and D3171 [25]. Samples for ESEM inspection were cast in epoxy resin, polished to $1\mu m$ finish and sputter coated with carbon (layer thickness of approx. 15nm). Environmental scanning electron microscopy (ESEM) was performed using an EVO 60 (Zeiss, Oberkochen, Germany) to analyse the composite specimen cross sections, and interfaces after testing.

2.5. Mechanical test procedure

Curved beam

Curved beam specimens were subject to four point bending, inducing a pure moment in the 'legs' of the specimen. The straight portion of the curved beam samples were reinforced by stainless steel dog-bone shaped sleeves to avoid excessive rotations. This reinforcement technique was previously used by Krumenacker [26]. A universal testing machine with a 25kN load cell was used. The test was performed under displacement control with a constant cross head displacement rate of 0.5mm/s. The tests were video recorded using a DSLR camera (16.2MP sensor).

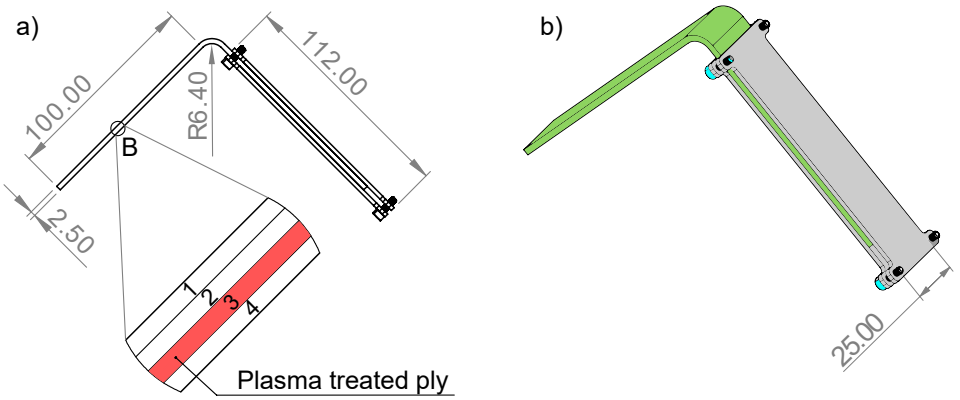

Figure 5: Illustration of curved beam sample and dog-bone shaped stiffener sleeves. a) side view with dimensions and zoomed view of the layup. b) perspective view.

Short beam shear

The short beam shear samples are subjected to 3-point bending in a universal testing machine with a crosshead displacement of 1 mm/s. A 10kN load cell was used. The roller support spacing is set so that the span to thickness ratio is 4.0. Acceptable failure modes are interlaminar shearing, initiating either at the centre of the specimen or near the edges.

2.6. Data Analysis

Statistical analysis was performed on the short beam shear and curved beam results to determine if the treatment significantly reduces the interlaminar shear strength and interlaminar tensile strength, respectively. Since

sample populations are small and of different population size, a two-sample t-test assuming unequal variances is used. A one-tailed t-test with significance level of 5% is used because we are interested only in the strength reduction of the treatment. If the null hypothesis is rejected (P-value lower than 0.05) we can conclude that the treatment condition has a significant effect on the interlaminar strength (tensile or shear)[27].

3. Results

3.1. Treatment of fibres

In table 1, the elemental composition of the treated glass fibre surface obtained by XPS is presented. A clear increase in mean F:C ratio is observed with a decrease in treatment speed. Table 1 shows that the increase in mean fluorine content and mean F:C ratio was one order of magnitude higher for the 1mm/s treatment than for the 10mm/s treatment. In table 1, the positions *Y+, Y0* and *Y-* refer to the position along the water cooled electrode, as shown in fig. 3a. There is a significant variation in the F:C ratio across the width of the treated fabric. The dynamic micro-wetting test results are presented in table 2, with decreasing treatment speed (i.e. increasing treatment severity) the mean wetting rate decreases. It was observed that in the wetting characterisation of the most severely treated fabric (1mm/s), the glycerol test liquid would in some cases not wet the fabric at all with contact angles (θ) of 115-120° observed for more than 10 minutes. This is higher than the 105° advancing contact angle of glycerol on polytetrafluoroethylene (PTFE) reported by Lee et al. [28]. By comparison, the untreated fabric would always be wetted in less than 1 minute.

No significant variation in wetting rates was observed for different (Y-axis) positions across the electrode.

3.2. Microstructure

The microstructure of the straight 'leg' section is shown in fig. 6. The images shown are of the plasma treated ply with treatment speed of 1mm/s. Uniform contact between fibre and matrix is observed without gaps in the fibre/matrix interface, in addition to little visible porosity in the matrix. Fibre volume fraction (FVF) and porosity analysis results are presented in table 3.

Table 1: Elemental composition of glass fibre surface before and after treatment.

Treatment	Position	Elemental composition [at.%]					
		C1s	O1s	F1s	Si2p	F:C ratio	O:C ratio
Untreated		74.5	25.5	0.0	0.0	0.00	0.34
10mm/s (low treatment)	Y+	72.6	20.8	4.4	2.2	0.06	0.29
	Y0	77.7	20.6	0.5	1.1	0.01	0.27
	Y-	75.9	22.0	0.0	1.6	0.00	0.29
	mean	75.4	21.1	1.7	1.7	0.02	0.28
1mm/s (high treatment)	Y+	63.4	18.0	17.3	1.2	0.27	0.28
	Y0	68.6	21.4	9.3	0.7	0.14	0.31
	Y-	72.6	23.0	4.4	0.0	0.06	0.32
	mean	68.2	20.8	10.3	0.6	0.15	0.31

Table 2: Dynamic micro-wetting results for plasma treated fabrics.

Treatment	Mean wetting rate (α) [s^{-1}]	SD	Factor decrease wetting rate
Untreated	1.4E-01	8.0E-02	1
10mm/s (low)	1.9E-02	2.0E-02	7
1mm/s (high)	8.7E-04	2.0E-03	157

The fibre content decreases with increasing treatment severity, however the porosity content is unaffected.

Table 3: Fibre volume fraction analysis of treated and untreated composite beams.

Treatment	Fibre content		Matrix content		Porosity content	
	Mean	SD	Mean	SD	Mean	SD
Untreated	53.7	0.8	45.6	0.8	0.7	0.1
10mm/s (low)	52.5	0.6	46.7	0.7	0.8	0.1
1mm/s (high)	50.3	0.7	48.9	0.7	0.8	0.1

3.3. Interlaminar tensile strength

The test results for the curved beam experiment are shown in table 4. The t-test result shows that we fail to reject the null hypothesis for the 10mm/s treatment, whereas we can reject the null hypothesis in the case of the 1mm/s treatment. This means that the strength reduction was statistically significant for the high treatment (1mm/s) but not statistically significant for the

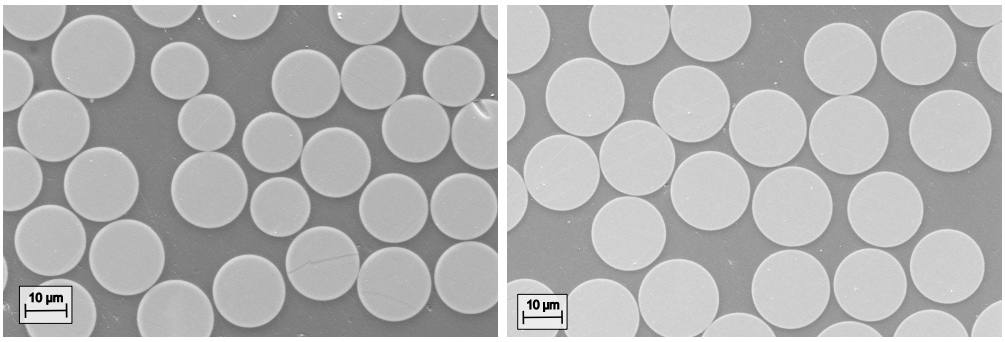

(a) (b)

Figure 6: Micrograph of plasma treated ply in curved beam specimen. Specimen treatment velocity was 1mm/s (high treatment). **a)** Microstructure of untreated ply in curved beam specimen, straight section. **b)** Microstructure of plasma treated ply (1mm/s treatment) in curved beam specimen, straight section.

Table 4: Interlaminar tensile strength (ILTS) results for treated and untreated beams. Sample standard deviation (SD) shown for the data set.

Treatment	Number of specimens	ILTS ($\hat{\sigma}_{22}$) Mean [MPa]	SD	Decrease mean ILTS [%]	T-test P-value
Untreated	13	23.4	3.7	-	
10mm/s (low)	5	22.3	4.6	4.7	0.335
1mm/s (high)	6	20.4	2.6	12.8	0.028

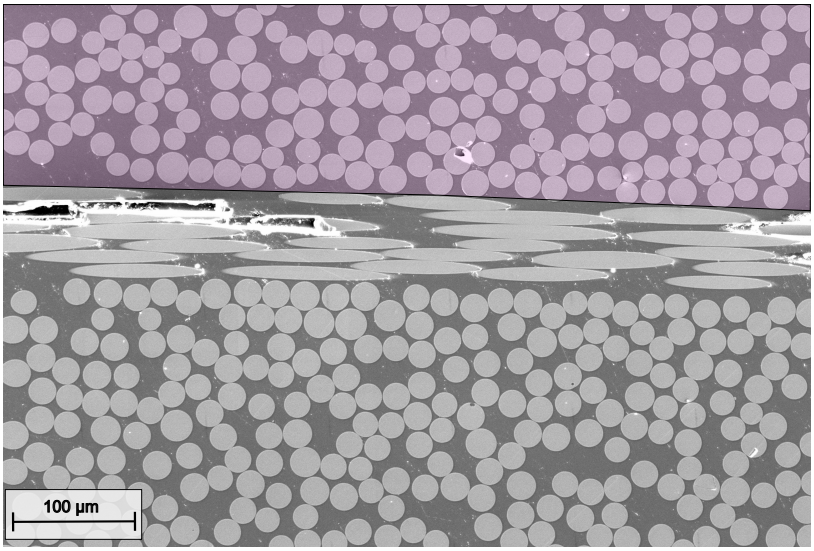

Figure 7: Micrograph of infused laminate. The top ply (highlighted) in the image has been treated at a rate of 1mm/s.

low treatment (10mm/s). Post-test microscope observations showed that all specimens with the 1mm/s treatment showed cracks on the interface of the treated ply i.e. on the interface between plies 2/3 and plies 3/4 (illustrated in fig. 8). The treated specimens never showed cracking on the interface of plies 1/2. Out of 13 samples without treatment, 7 showed cracks on the interface between ply 1 and ply 2.

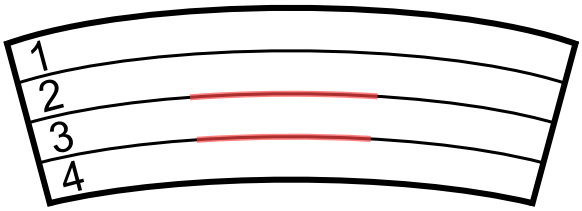

Figure 8: Illustration of crack location in the test section of a curved beam specimen.

3.4. Interlaminar shear strength

The test results for the interlaminar shear strength test are presented in table 5. In the case of the 10mm/s treatment we fail to reject the null hy-

Table 5: Interlaminar shear strength (ILSS) results for treated and untreated beams. Sample standard deviation (SD) included for the data set.

Treatment	Number of specimens	ILSS ($\hat{\sigma}_{12}$) Mean [MPa]	SD	Decrease mean ILSS ($\hat{\sigma}_{12}$) [%]	T-test P-value
Untreated	12	64.3	3.9	-	-
10mm/s (low)	12	62.6	3.7	2.6	0.143
1mm/s (high)	12	61.6	1.9	4.2	0.027

pothesis. The t-test result shows that we can reject the null hypothesis in the case of the 1mm/s treatment. Thus, the failure mode of all the specimens was shear cracking, consistent with the acceptable failure modes described in the ASTM D2344 standard [23]. Typically, multiple parallel shear cracks were formed, both within the plies and on the interfaces between plies. There was no observed consistent difference in failure mode between the treated or untreated samples.

4. Discussion

4.1. Discussion on treatment results

The results (sec. 3.1) show that, in both treatment conditions fluorine containing polymer was successfully polymerized onto the fibre surface. However, the mean fluorine content increase was more pronounced for the slower 1mm/s treatment. Dynamic wetting tests showed that a significant reduction in wetting was achieved for both treatments. The presence of fluorine on the fibre sizing surface and the observed de-wetting effect is expected to delay the interaction between the sizing surface and resin during infusion, creating a weaker interface.

The fluorine content observation at different (Y positions) showed that the treatment was not uniform across the electrode, with a significantly larger fluorine content on the Y+ side than on the Y- side. The variation of the treatment across the electrode width may be attributed to a combination of; uneven spacing between the ground electrode and the powered electrode, gas mix uniformity, air leakage from surroundings and consumption of the precursor. Contamination with ambient air is expected to be more pronounced for the faster treatment condition (10mm/s) which reduces the efficacy of the

treatment. Previous work by Fang et al. [13] using the same treatment setup to treat PET films, showed a similar variation across the electrode. In that study, the PET film was uniform in thickness which indicates that any thickness variation in the glass fabric was not the leading cause for variation in fluorine on the fabric surface. In the present study gas flow was observed to be relatively uniform across the electrode by IR camera. Therefore it seems more likely that the variation in fluorine content is due to a variation in the gap between the two electrodes. A small decrease in the electrode spacing results in a lower impedance and higher current density of the plasma, which in turn results in a larger consumption of precursor giving uneven treatment results.

In a previous study [6], fluorination by plasma treatment in a helium/ tetrafluoromethane (He/CF_4) gas mixture was conducted on the same fabric type as in the current study. The F:C ratio observed for the 1mm/s treatment in the current study is an order of magnitude larger than the high treatment case in the previous study. Furthermore, the wetting rate is one order of magnitude lower than what was found in the previous study. This difference is attributed to the fact that octofluorocyclobutane (OFB) may polymerize on the fibre sizing surface, whereas CF_4 is introduced by means of a substitution reaction [14]. As an alternative to fluorine containing gasses, it possible to achieve hydrophobic surfaces by deposition of organosilicone films by atmospheric pressure plasma treatment [29].

4.2. Discussion on mechanical test results

Dynamic micro wetting results indicate a very strong effect of the treatment on the wetting properties. For the 1mm/s treatment the wetting was 157 times slower than the untreated condition. However, in comparison with the reduction in wetting properties, there is a relatively small decrease in interlaminar tensile strength (12.8%) and interlaminar shear strength (4.2%). The results of the t-test indicate that the reduction in both interlaminar tensile strength and interlaminar shear strength observed for the 1mm/s treatment is statistically significant. The reduction in strength is attributed to the polymerized fluorocarbons on the fibre sizing surface, which act as bond inhibitors at the fibre/matrix interface and delay the initial interaction between fibre sizing surface and the resin.

The 10mm/s (low) treatment however does not show a statistically significant reduction in either interlaminar tensile or interlaminar shear strength tests. It is perhaps surprising that wetting rate that is 7 times lower than the untreated specimen does not translate to a significant reduction in either interlaminar tensile or shear strength. Fibre wetting is often stated to be important to achieving a good laminate quality (i.e. full fibre/matrix contact and interphase adhesion) and a key driver of sizing development [30; 31]. A previous study by Larson and Drzal [16] on glass fibre/vinyl ester composite systems included wetting analysis and the short beam shear test. One fibre system was coated in release agent, resulting in poor wetting, however the ILSS showed a minor reduction. They attribute this to the sizing layer diffusing into the resin during infusion, thereby spreading out the thin film of release agent into the fibre/matrix interphase region.

An interesting observation is that the porosity content of the laminate did not increase with either of the treatment conditions (table 3). Furthermore, SEM observations did not reveal defects or poor contact between fibre and resin. This may be due to the manufacturing method (vacuum infusion) resulting in fully displacing the trapped air in the fabrics with resin. Other manufacturing methods such as wet layup with ambient pressure curing may show more defects in a fluorinated ply. A potential application of this treatment could be in the field of non-destructive testing, this could be used to create consistent partial bonds, without the use of grease, release agent or a slipfoil [32; 33; 5].

The delamination crack location was observed to be more controlled for the treated curved beam specimens, in the sense that cracks always formed on the interface of the treated ply, or within the treated ply (as indicated in fig. 8). This strongly indicates that the plasma treatment led to damage initiation, i.e. control of damage initiation. This suggests that in experiments where a high interlaminar tensile stress is present, such as a mode I double cantilever beam test (fig. 1), this treatment could generate multiple cracks. In the interlaminar shear strength tests however, such a control of crack location was not observed.

The curved beam test specimen has large tensile stresses in a very small area, therefore it is very sensitive to manufacturing defects. A small pore in the curved region may act as an initiator for damage propagation, skewing

the results towards lower interfacial strengths. Careful manufacturing is required with high quality inspection to detect any defect in the gauge area. Makeev et al. [18; 20] used X-CT to analyse the test region before mechanical testing and identified defects in 3D in each specimen. By modelling the defects in FEM, a very accurate peak stress could be determined. This is closer to a real material value than the values obtained by means of the ASTM D6415 method, which tests manufacturing quality. However, the procedure of X-CT followed by FE modelling is prohibitively expensive and involved, as acknowledged by Makeev et al. [18; 20]. The curved beam test alone is thus not a sufficient method for determining the interlaminar tensile strength.

5. Conclusion

Treatment of sized glass fibre fabrics with atmospheric pressure plasma in a fluorine containing gas has resulted in the polymerization of fluorocarbons onto the fibre sizing surface. As a result of the polymerization with fluorocarbons a strong decrease in wettability of the fabrics with a polar test liquid was observed.

An interlaminar strength reduction can be achieved for fabrics plasma treated in fluorine containing gas. Interlaminar tensile strength was reduced 3 times more than interlaminar shear strength. There is a dependency on the speed of the treatment (i.e. exposure time to the plasma) and the strength reduction. A slower treatment speed resulted in a introduction of more fluorine on the fibre sizing surface and a larger decrease in interlaminar strength (tensile and shear).

Acknowledgements

This research is conducted as part of the DACOMAT project. The DACOMAT project has received funding from the European Union's Horizon 2020 research and innovation programme 5 under GA No. 761072. Special thanks to Jonas Kreutzfeldt Heininge, Kenneth Algart and Jan Sjølin for assistance with specimen manufacturing and testing.

References

[1] M. Rask, B. F. Sørensen, Determination of the J integral for laminated double cantilever beam specimens: The curvature approach, Engineering Fracture Mechanics 96 (2012) 37–48. doi:10.1016/J.ENGFRACMECH.2012.06.017.

[2] Y. Kusano, B. F. Sørensen, T. L. Andersen, F. Leipold, Adhesion improvement of glass-fibre-reinforced polyester composites by gliding arc discharge treatment, Journal of Adhesion 89 (6) (2013) 433–459. doi:10.1080/00218464.2013.759063.

[3] S. Goutianos, B. F. Sørensen, Fracture resistance enhancement of layered structures by multiple cracks, Engineering Fracture Mechanics 151 (2016) 92–108. doi:10.1016/j.engfracmech.2015.10.036.

[4] S. Goutianos, B. F. Sørensen, Enhancement of fracture resistance by multiple cracks in layered structures under mode I and mix mode loading, ICCM International Conferences on Composite Materials 2017-Augus (2017).

[5] P. B. Nagy, Ultrasonic classification of imperfect interfaces, Journal of Nondestructive Evaluation 11 (3-4) (1992) 127–139. doi:10.1007/BF00566404.

[6] D. J. H. Cederløf, Y. Kusano, S. Fæster, Fluorination of sized glass fibres for decreased wetting by atmospheric pressure plasma treatment in He / CF 4, The Journal of Adhesion 00 (00) (2019) 1–11. doi:10.1080/00218464.2019.1686364.

[7] O. Teraube, J. C. Agopian, E. Petit, F. Metz, N. Batisse, K. Charlet, M. Dubois, Surface modification of sized vegetal fibers through direct fluorination for eco-composites, Journal of Fluorine Chemistry 238 (August) (2020) 109618. doi:10.1016/j.jfluchem.2020.109618.

[8] J. C. Agopian, O. Teraube, M. Dubois, K. Charlet, Fluorination of carbon fibre sizing without mechanical or chemical loss of the fibre, Applied Surface Science 534 (May) (2020) 147647. doi:10.1016/j.apsusc.2020.147647.

[9] M. Dey, J. M. Deitzel, J. W. Gillespie, S. Schweiger, Influence of sizing formulations on glass/epoxy interphase properties, Composites Part A: Applied Science and Manufacturing 63 (2014) 59–67. doi:10.1016/j.compositesa.2014.04.006.

[10] E. Mäder, Study of fibre surface treatments for control of interphase properties in composites, Composites Science and Technology 57 (8) (1997) 1077–1088. doi:10.1016/S0266-3538(97)00002-X.

[11] P.-S. Shin, Y.-M. Baek, J.-H. Kim, H.-S. Park, D.-J. Kwon, J.-H. Lee, M.-Y. Kim, K. L. DeVries, J.-M. Park, Interfacial and wetting properties between glass fiber and epoxy resins with different pot lifes, Colloids and Surfaces A: Physicochemical and Engineering Aspects 544 (2018) 68–77. doi:10.1016/J.COLSURFA.2018.02.017.

[12] S. J. Park, J. S. Jin, J. R. Lee, Influence of silane coupling agents on the surface energetics of glass fibers and mechanical interfacial properties of glass fiber-reinforced composites, Journal of Adhesion Science and Technology 14 (13) (2000) 1677–1689. doi:10.1163/156856100742483.

[13] C. Fang, D. J. Hottentot Cederløf, A. Bardenshtein, Y. Kusano, Air-to-air atmospheric pressure plasma treatment - Perspective for composite manufacturing, IOP Conference Series: Materials Science and Engineering 942 (1) (2020). doi:10.1088/1757-899X/942/1/012030.

[14] Y. Kusano, M. Yoshikawa, K. Naito, S. Okazaki, M. Kogoma, Atmospheric pressure plasma polymerization of fluorinated monomers, in: Proceedings of the 7th Symposium on Plasma Science for Materials SPSM 7, 1994, pp. 77–81.

[15] ASTM International, Standard test method for measuring the curved beam strength of a fiber-reinforced polymer-matrix composite, Tech. rep. (2013). doi:10.1520/D6415.

[16] B. K. Larson, L. T. Drzal, Glass fibre sizing/matrix interphase formation in liquid composite moulding: effects on fibre/matrix adhesion and mechanical properties, Composites 25 (7) (1994) 711–721. doi:10.1016/0010-4361(94)90206-2.

[17] ASTM International, Standard Test Method for Through-Thickness " Flatwise " Tensile Strength and Elastic Modulus of a Fiber-Reinforced Polymer Matrix Composite, Tech. rep. (2015). doi:10.1520/D7291.

[18] A. Makeev, G. Seon, Y. Nikishkov, E. Lee, Methods for assessment of interlaminar tensile strength of composite materials, Journal of Composite Materials 49 (7) (2015) 783–794. doi:10.1177/0021998314525979.

[19] T. J. Lu, Z. C. Xia, J. W. Hutchinson, Delamination of beams under transverse shear and bending, Materials Science and Engineering A 188 (1-2) (1994) 103–112. doi:10.1016/0921-5093(94)90361-1.

[20] A. Makeev, P. Carpentier, B. Shonkwiler, Methods to measure interlaminar tensile modulus of composites, Composites Part A: Applied Science and Manufacturing 56 (2014) 256–261. doi:10.1016/J.COMPOSITESA.2013.10.018.

[21] A. Makeev, Y. He, P. Carpentier, B. Shonkwiler, A method for measurement of multiple constitutive properties for composite materials, Composites Part A: Applied Science and Manufacturing 43 (12) (2012) 2199–2210. doi:10.1016/j.compositesa.2012.07.021.

[22] S. Lekhnitskiy, Anisotropic Plates, 2nd Edition, Gosudarstvennoye Izdatel'stvo, Moscow, 1957.

[23] ASTM International, Standard test method for short-beam strength of polymer matrix composite materials, Tech. Rep. Reapproved 2006 (2011). doi:10.1520/D2344.

[24] ASTM International, Standard test method for ignition loss of cured reinforced resin, Tech. rep. (2011). doi:10.1520/D2584-18.2.

[25] ASTM International, Standard test methods for constituent content of composite materials, Tech. Rep. December (2010). doi:10.1520/D3171-15.2.

[26] N. Krumenacker, Experimental study of variability and defects in vacuum-bag-only corner laminates, Ph.D. thesis (2018).

[27] R. A. Fisher, Statistical Methods for Research Workers, 5th Edition, Oliver and Boyd Ltd., Edinburgh, 1934.

[28] S. Lee, J. S. Park, T. R. Lee, The wettability of fluoropolymer surfaces: Influence of surface dipoles, Langmuir 24 (9) (2008) 4817–4826. doi:10.1021/la700902h.

[29] P. Dimitrakellis, E. Gogolides, Hydrophobic and superhydrophobic surfaces fabricated using atmospheric pressure cold plasma technology: A review, Advances in Colloid and Interface Science 254 (2018) 1–21. doi:10.1016/J.CIS.2018.03.009.

[30] J. Thomason, Glass fibre sizing: A review, Composites Part A: Applied Science and Manufacturing 127 (2019) 105619. doi:10.1016/J.COMPOSITESA.2019.105619.

[31] A. Patnaik, R. S. Rengasamy, V. K. Kothari, A. Ghosh, Wetting and wicking in fibrous materials, Textile Progress 38 (1) (2006) 1–105. doi:10.1533/jotp.2006.38.1.1.

[32] K. Katnam, L. da Silva, T. Young, Bonded repair of composite aircraft structures: A review of scientific challenges and opportunities, Progress in Aerospace Sciences 61 (2013) 26–42. doi:http://doi.org/10.1016/j.paerosci.2013.03.003.

[33] B. Ehrhart, B. Valeske, C. Bockenheimer, Non-destructive evaluation (NDE) of aerospace composites: Methods for testing adhesively bonded composites, in: V. M. Karbhari (Ed.), Methods for testing adhesively bonded composites, Woodhead Publishing Series in Composites Science and Engineering, Woodhead Publishing, 2013, pp. 220–237. doi:10.1533/9780857093554.2.220.